Chem Soc Rev

REVIEW ARTICLE

View Article Online
View Journal | View Issue

Cite this: *Chem. Soc. Rev.*, 2019, **48**, 4424

Interface design for high energy density polymer nanocomposites

Hang Luo,†[a] Xuefan Zhou,†[a] Christopher Ellingford,[b] Yan Zhang,[ac] Sheng Chen,[d] Kechao Zhou,[a] Dou Zhang,*[a] Chris R. Bowen*[c] and Chaoying Wan*[b]

Received 30th March 2019

DOI: 10.1039/c9cs00043g

rsc.li/chem-soc-rev

This review provides a detailed overview on the latest developments in the design and control of the interface in polymer based composite dielectrics for energy storage applications. The methods employed for interface design in composite systems are described for a variety of filler types and morphologies, along with novel approaches employed to build hierarchical interfaces for multi-scale control of properties. Efforts to achieve a close control of interfacial properties and geometry are then described, which includes the creation of either flexible or rigid polymer interfaces, the use of liquid crystals and developing ceramic and carbon-based interfaces with tailored electrical properties. The impact of the variety of interface structures on composite polarization and energy storage capability are described, along with an overview of existing models to understand the polarization mechanisms and quantitatively assess the potential benefits of different structures for energy storage. The applications and properties of such interface-controlled materials are then explored, along with an overview of existing challenges and practical limitations. Finally, a summary and future perspectives are provided to highlight future directions of research in this growing and important area.

[a] State Key Laboratory of Powder Metallurgy, Central South University, Changsha, Hunan 410083, China. E-mail: dzhang@csu.edu.cn
[b] International Institute for Nanocomposites Manufacturing (IINM), WMG, University of Warwick, CV4 7AL, UK. E-mail: chaoying.wan@warwick.ac.uk
[c] Department of Mechanical Engineering, University of Bath, Bath, BA2 2ET, UK. E-mail: c.r.bowen@bath.ac.uk
[d] Key Laboratory of Polymeric Materials and Application Technology of Hunan Province, College of Chemistry, Xiangtan University, Xiangtan 411105, Hunan Province, China
† These authors contributed equally to this work.

1. Introduction

Polymers are a key element in energy harvesting and storage devices due to their unique properties in comparison with traditional ceramic and metallic materials, such as high breakdown strength, mechanical flexibility, low density, ease of processing and low cost.[1–6] Today, functional polymer composites are attracting interest in an increasing number of applications, including polymer based dielectric capacitors which are widely employed in the areas of power transmission, hybrid

Hang Luo

Hang Luo obtained his PhD degree in Material Science and Engineering from Central South University in 2016, and he continued post-doctoral studies in Chemistry at Central South University. He has worked as an Associate Professor at the State Key Laboratory of Powder Metallurgy, Central South University since 2017. His work has concentrated on interface design, polymer based dielectrics for energy storage and ferro-/piezo-electric ceramics.

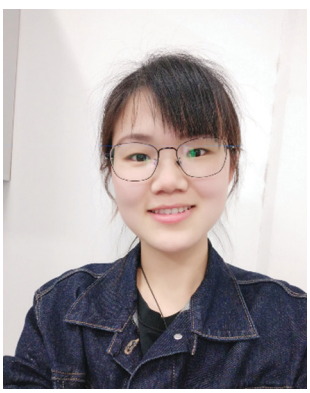

Xuefan Zhou

Xuefan Zhou obtained her BSc degree in Material Engineering from Central South University in 2017. She is currently a PhD student at the Powder Metallurgy Research Institute of Central South University. Her PhD work focuses on sodium bismuth titanate based lead-free piezoelectric ceramics for enhancing their piezoelectric properties and strain response. In addition, she also studies dielectric capacitors for energy storage applications.

electric vehicles, high power weapons, radar, wind power generation, and microelectronic systems; these sectors are summarized in Fig. 1. As an example, a converter valve is used for the conversion of an alternating current (AC) into a direct current (DC) in high voltage direct current (HVDC) transmission engineering, and in such a system the dielectric capacitors occupy over 50% of the volume. Polymers are preferred due to their advantages in terms of excellent electrical properties and ease of forming in continuous and large area dielectric films with a tailored thickness in the micrometer range. Table 1 provides a summary for a variety of current dielectrics in polymeric and ceramic form.[3,7–14] The dielectric material often employed in commercially available capacitors is biaxially oriented polypropylenes (BOPP). However, the mismatch between ambient temperature (~140 °C) and the maximum operating temperature (~105 °C) of BOPP can become a limitation to its application.[15] In this case, high-temperature dielectric materials, such as polyethylene naphthalate (PEN), polyphenylene sulfide (PPS), poly(ethylene terephthalate) (PET) and polyimide (PI) have been developed.[7] Another important commercially available capacitor system is the multi-layer ceramic capacitor (MLCC), where the mainstream dielectric is the $BaTiO_3$ or doped-$BaTiO_3$ ceramics.[16] Compared with the capacitors formed from bulk ceramics, MLCC possesses high capacitance (*e.g.* 1–100 μF), small volume (*e.g.* 0.6 by 0.3 mm^2), high reliability, and excellent high-frequency characteristics.[17] In addition, MLCCs can endure a relatively high electric field due to the small thickness of the individual layers, of the order of several microns, compared with bulk ceramic capacitors whose dimensions are several hundred microns.[18] Recently, electroactive polymers with high relative permittivity, such as ferroelectric poly(vinylidenefluoride) (PVDF) and its co/ter-polymers, and ceramic/polymer composites have been intensively studied due to their high permittivity and high breakdown strength. A comparison to show the ranges for different energy storage devices are summarized in Table 2, where the advantages of polymer based dielectric capacitors include high power density, high efficiency, stability and low cost compared

Sheng Chen

Sheng Chen received his PhD degree in Polymer Chemistry and Physics from Xiangtan University in 2013. After graduation, he worked in the College of Chemistry in Xiangtan University as an Associate Professor. His research interests include the design, synthesis and phase structure of liquid crystalline polymers, and energy storage of polymer-based nanocomposites.

Dou Zhang

Dou Zhang obtained his PhD degree in Metallurgy & Materials from University of Birmingham in 2006. He is currently a Professor in Powder Metallurgy Research Institute of Central South University. His research is focused on ferroelectric ceramics for energy and microwave applications; piezoelectric ceramics and composites as sensors and actuators; porous ceramics; bioceramics; ceramic microsystem techniques, including colloidal micromoulding and 3D printing. Particular attentions are paid to the controllability of fine scale structures and their impact on device performance.

Chris R. Bowen

Christopher Rhys Bowen has a BSc degree in Materials Science from the University of Bath (1986–1990) and a DPhil from the University of Oxford (1990– 1993). Post-doctoral work was at Tecnische Universität Harburg-Hamburg and University of Leeds (1994–1996). He was Senior Scientist at the Defence Evaluation and Research Agency from 1996–1998. He joined Bath as a Lecturer in 1998 and is now Professor of Materials, where research includes energy harvesting, ferroelectrics and functional ceramics.

Chaoying Wan

Dr Chaoying Wan is Associate Professor in multifunctional nanocomposites at the University of Warwick, UK. She obtained a PhD degree in Materials Science in 2004 at Shanghai Jiao Tong University. She was awarded a Marie Curie Fellowship and worked at Trinity College Dublin between 2009 and 2011. She specialises in polymer synthesis and characterisation of multiphase/multicomponent nanocomposites, smart dielectric elastomers and sustainable rubbers for energy applications.

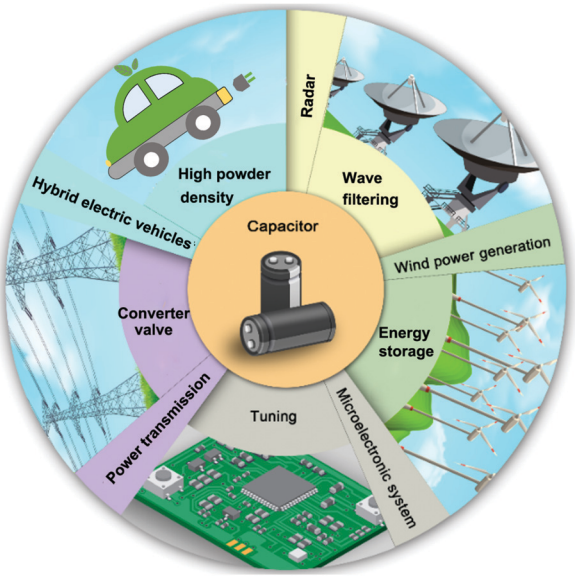

Fig. 1 The emerging applications of dielectric capacitors.

with other energy storage devices such as lithium ion batteries and supercapacitors.[7,19–27]

In order to enhance polymer properties for applications, such as those in Fig. 1, a wide variety of polymer based composite systems are being explored. These are based on a polymer matrix that contains organic, ceramic, and carbon-based fillers that can be either randomly dispersed, aligned or ordered in a multi-layer form.[28–32] The properties of polymer composites do not solely rely on the structure and properties of the individual components, since we will see in this review that interfacial interactions between the matrix and filler has an important role in determining the overall performance.[33–35]

In such composite systems, an additional third phase, namely the interfacial region is introduced and due to the high specific surface area of nanoscale fillers, the volume ratio of the interfacial phase can be as high as 50–70 vol%. As a consequence, the interfacial properties can have a significant impact on the overall performance of nanocomposites and their devices.

For a linear dielectric capacitor, the energy stored is related to the working voltage (V) and the capacitance (C): $\frac{1}{2}CV^2$, the "energy density" is therefore given by eqn (1):

$$\frac{1/2CV^2}{v_d} = \frac{1}{2}\varepsilon_r\varepsilon_0 E_b{}^2 \quad (1)$$

where v_d is the volume of the capacitor material, ε_r is the relative permittivity, ε_0 is the permittivity of free space and E_b is the dielectric strength.[8,11,36] This leads to a merit index of $\varepsilon_r \times (E_{dielectric})^2$ for the maximum energy density (J m^{-3}). The energy storage performance is also influenced by the dielectric loss ($\omega\varepsilon''\varepsilon_0$; where ω is angular frequency and ε'' is imaginary permittivity), and the associated $\tan\delta = \varepsilon''/\varepsilon'$. The dielectric displacement as a function of applied electric field should also be considered in order to account for material non-linearities, which are often observed at high electric field, and avoid the above simplification of assuming a linear dielectric response.[16,37–39]

For polymer based nanocomposite systems, the surface modification of inorganic fillers using organic modifiers is often employed to enhance the interfacial interaction, material compatibility, and dispersion of the filler in a polymer matrix. However, the mismatch of relative permittivity or electrical conductivity between the inorganic fillers and polymer matrix often leads to the development of an inhomogeneous electric field distribution throughout the composite, and generally

Table 1 Summary of the properties of dielectrics for capacitor applications, which include biaxially oriented polypropylenes (BOPP), polyethylene naphthalate (PEN), polyphenylene sulfide (PPS), poly(ethylene terephthalate) (PET), polyimide (PI), poly(vinylidenefluoride) (PVDF) and multi-layer ceramic capacitor (MLCC)

Dielectrics for capacitors	Relatively permittivity (1 kHz)	Dielectric loss (1 kHz)	Breakdown strength (kV mm^{-1})	Max. operating temperature (°C)	Thermal conductivity (W (m K)$^{-1}$)	Energy density (J cm^{-3})
BOPP	2.2	~0.0002	~640	105	2.1–2.35	1–1.2
PEN	3.2	~0.0015	~550	125	~0.26	1–1.5
PPS	3.0	~0.0003	~550	200	~0.3	1–1.5
PET	3.6	~0.005	~570	125	0.29	1–1.5
PI	3.5	0.04	~238	~200	6.58–11.7	1.4
PVDF and its co/ter-polymer	~>10	~0.02–0.2	~200–600	125	~0.24	~>4
Ceramics/polymer composites	~50	~0.02–0.08	~300–500	~150	—	~10–30
MLCC	~100–3000	—	—	~125	—	~10
Bulk ceramics	~10^2–4 × 10^3	—	~10–50	~200	—	~1–7

Table 2 Comparison of key performance indicators for a variety of energy storage devices

Energy storage devices	Power density (W kg^{-1})	Energy density (W h kg^{-1})	Efficiency	Stability	Cost
Dielectric capacitor	~10^4–10^7	~10^{-2}–10^{-1}	High	Good	Low
Supercapacitor	~>10^4	~<10	Low	Good	High
Lithium-ion batteries	~<1000	~150–250	High	Low	Low

leads to a significant reduction of the breakdown strength of dielectric composites. We will see later in this review that this is due to the electric field being concentrated in the low permittivity phase as a consequence of Gauss' law.[40,41] This field concentration can be overcome to some extent by constructing an inorganic shell layer, grafting multifunctional organic shell layers, using multiple hierarchical shells on the surface of the fillers and building topological structures, including sandwiched or multi-layered structures.

The aim of this review is to overview the important role of the interface and interphase to allow tailoring of the properties of nanocomposite dielectrics. Polymer nanocomposites for energy storage applications continues to be a growing area that has attracted increasing discussion *via* a variety of existing reviews. These include a wide variety of key topics, which include an examination of PVDF and its copolymers, and their nanocomposites for high energy density capacitor applications;[7,8,11,22,42–45] high-temperature dielectric nanocomposites;[10,15] high-κ dielectrics;[18,46,47] recent achievements on $BaTiO_3$ nanomaterials and their synthesis, dielectric and ferroelectric properties;[48] dielectric and energy storage properties of polymers and multilayered dielectrics films;[3,49,50] ceramic films and bulk ceramics for energy storage capacitors;[12,16,25,32,51] the effects of fillers on the dielectric and energy storage properties of polymer composites;[2,52] carbon based polymer composites for energy storage;[9,53,54] polymer based nanodielectric design for advanced capacitors;[45,55,56] interface engineering in polymer nanocomposites to improve energy storage;[36,57] and the strategies for engineering the surfaces of fillers.[58]

This review will cover methods of interface design by introducing the range of interface layers and structures. Examples include the creation of core–shell structures that use organic, insulating ceramic (dielectric) and electrically conductive outer-layers on nano-fillers; including sandwich and multi-layer architectures (Section 2). The efforts to create multiple shells with hierarchical and controlled graded structures to further improve nanocomposite performance are discussed (Section 3). The effect of the interface on polarization mechanisms, breakdown strength and growth of defects is then discussed. There is an in-depth examination of the influence of filler morphology, such as filler dimensionality, aspect ratio and volume fraction, along with an overview of the variety of models being developed for prediction of properties and understand effective properties (Section 4). Specific examples of interfacial design strategies and its impact for high performance energy storage capacitors are discussed (Section 5). Finally, an outlook and future perspectives of high-performance polymer composite capacitors are proposed.

2. Architectures for interface design

In this section we will provide an overview of the interface types observed in dielectric nanocomposites, as shown in Fig. 2. The fillers can be considered at a range of dimensions,[59–61] namely zero dimensional (0D) nanofillers which include spherical nanoparticles, nanocubes and nanoparticles with irregular morphologies, one dimensional (1D) nanofillers which include nanowires, nanofibers, nanotubes and nanoribbons, and two dimensional (2D) nanofillers which include nanosheets and nanoplatelet, as shown in the left column of Fig. 3. The outer surface of the fillers can be coated with a range of materials, as seen in the center column of Fig. 3, which can be used to tune the interface between filler and matrix; see right column of Fig. 3.

The strategies of core shell synthesis including adsorption, grafting from, grafting to, star-like nanoreactors and sol–gel/hydrothermal approaches will now be described based on organic or inorganic shells, hierarchical outer layers (Fig. 2a), and multi-layer structures (Fig. 2b). As a representative structure, 0D nanofillers will be firstly covered used to describe

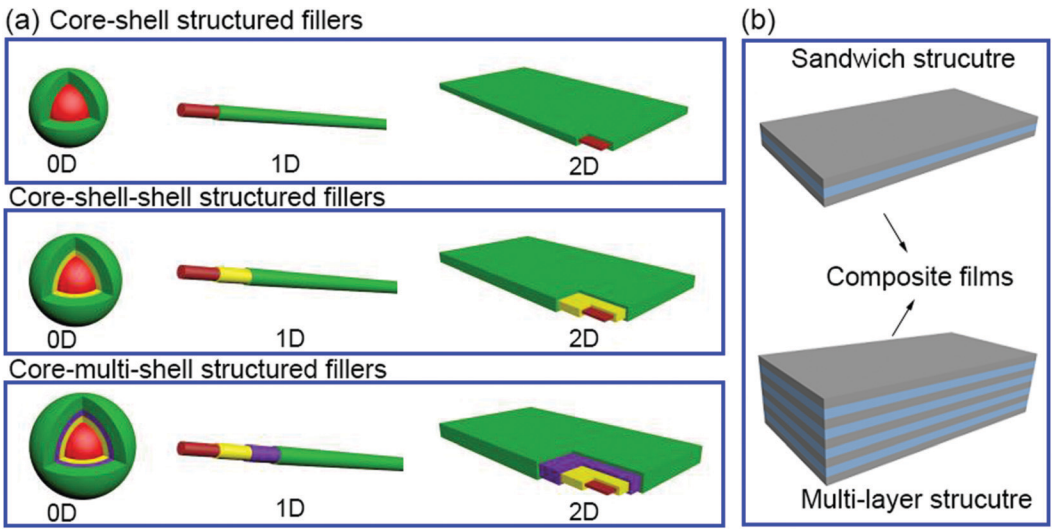

Fig. 2 (a) Core–shell structured fillers including core–shell, core–shell–shell and core–multi-shell structures in 0D, 1D and 2D form, (b) composites films including sandwich and multi-layer structures.

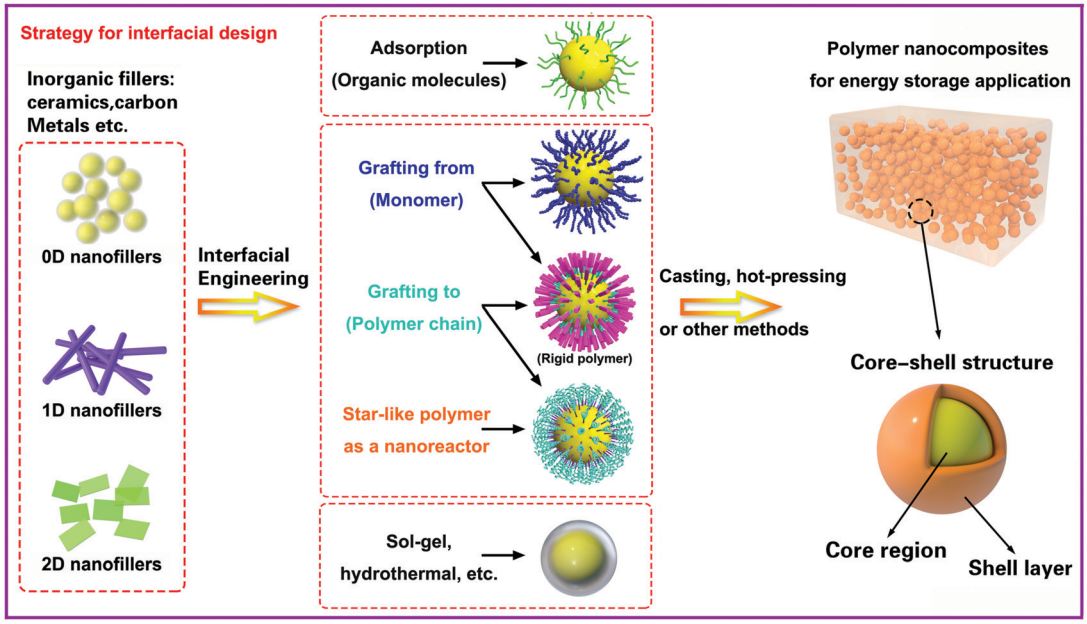

Fig. 3 General methods associated with the design and control the interface of core–shell structured fillers for dielectric capacitor application. The left column shows the range of filler types, the central column indicates the core–shell interfacial control methods and the right column shows the final nanocomposite structure.

the processes of interfacial engineering and nanocomposite preparation.

2.1 Theory of surface energies

Ceramic fillers such as $Pb_{1-x}Zr_xTiO_3$ (PZT), $BaTiO_3$, TiO_2, $Ba_{1-x}Sr_xTiO_3$ (BST), and carbonaceous particles such as graphene and carbon nanotubes (CNT) are often incompatible with the polymer matrix due to the significant difference in surface energy compared to the matrix and poor polymer–particle interfacial interactions.[62] Inorganic fillers therefore tend to form agglomerates within polymer matrices which results in phase separation and poor properties.

Nano-scale fillers can readily agglomerate easily due to their high surface energy, high van der Waals forces or high electrostatic forces, resulting in the poor dispersity in the polymer matrix. The surface energy of a material is defined as the excess energy per unit area due to the existence of a free surface; it can also be the thermodynamic work done per unit area of surface extension. When the filler material possess a high surface energy, they tend to agglomerate in order to form a more stable lower energy state. Generally, high-surface energy materials include metals, metal oxides, and inorganic compounds (such as sapphire, nitrides, oxides, silica, and diamond), which exhibit dense, refractory, and hard properties, where the surface energy values of such materials is approximately 200–5000 dyn cm^{-1}. Organic polymers, which act as the composite matrix, are typically low surface energy materials, where the surface energy is approximately 10 and 50 dyn cm^{-1}. The reader is referred to the work of the Menachem Lewin group for a summary of surface tensions and surface energy values of these materials,[63] where the values of a range of polymers, minerals, oxides and clays based on theoretical calculations or empirical equations were also presented. In order to account for the difference of surface energy between the polymer-based matrix and inorganic fillers, the high-energy surfaces of inorganic fillers are often coated with low-energy surface materials, such as siloxane coupling reagents or polymers, whereby a thin layer can reduce the surface energy of inorganic fillers. Therefore, the design and construction of an interfacial layer using modifiers with different function properties is an attractive approach to enhance the dispersion properties of inorganic nano-scale fillers. Additional approaches to increase the compatibility between the filler and polymer matrix can be to exploit electrostatic interactions, hydrogen bonding or dipole–dipole interactions, which is summarized in Fig. 4.

2.2 Core–shell structure

To date, core–shell structured nanoparticles have been explored in depth for surface modification and multi-functional applications.[64–67] In polymer based nanocomposites, the ability to enhance dispersion of nanofillers and tailor the interfacial properties remain important technical challenges to be addressed[68–70] and the surface modification of fillers with a variety of organic modifiers is an effective approach to overcome these issues.[71,72] Organic modifiers can be physically adsorbed onto the filler surface through electrostatic interactions or by hydrogen bonding. A variety of modifiers have been used, as shown in Fig. 5, which include dopamine,[73,74] silanes,[75] phosphonic acid,[76] ethylene diamine,[77] polyvinyl alcohol,[78] and paraffin.[79] These organics have been utilized to modify the surfaces of inorganic fillers and are of interest due to their simple treatment process, for example by solution mixing. Alternatively, the organic shell can be

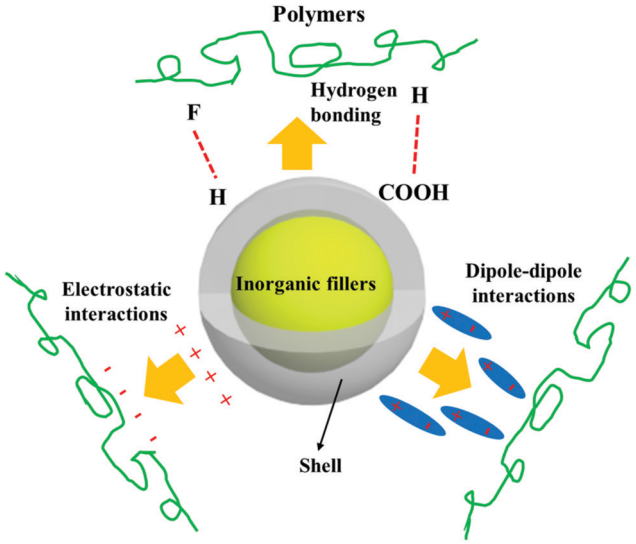

Fig. 4 Schematic of the range of interactions between the core–shell structured filler and polymers matrix.

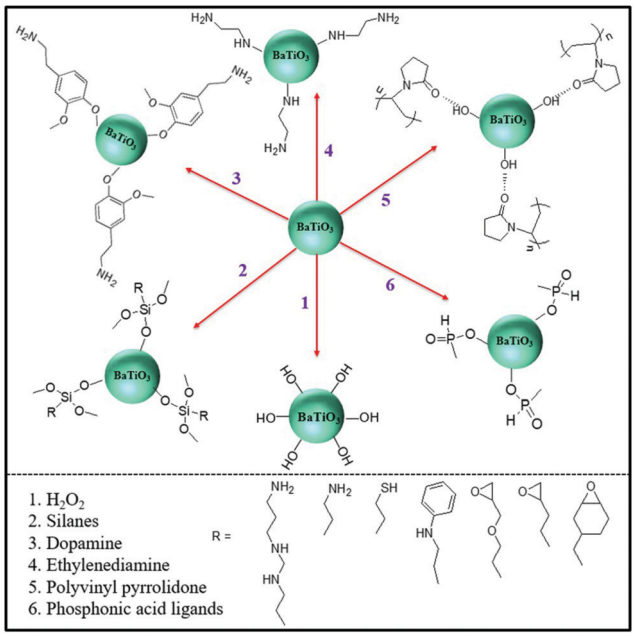

Fig. 5 Examples of organic modifiers for surface engineering of a ceramic filler particle, in this case $BaTiO_3$.[73–79]

chemically grafted onto the filler surfaces *via* "grafting to" or "grafting from" approaches through living/controlled free radical polymerization or click-chemistry reactions. The "grafting from" approach relies on the formation of a core–shell structure by the *in situ* polymerization of monomers on initiator-functionalized nanoparticle surfaces. In contrast, the "grafting to" approach leads to the formation of a core–shell structure by grafting the pre-prepared polymer chains onto the nanoparticle surface *via* a reaction between the polymer end-groups and the functional groups on the nanoparticle surface. Moreover, an additional strategy for the creation of a well-defined nanoparticle/polymer core–shell structure was developed using star-like polymers as nanoreactors; see central column of Fig. 3. These three methods will be examined in more detail in Section 3.1.

Table 3 summarizes the range of organic modifiers that have been employed to date for improving filler dispersion and compatibility in dielectric nanocomposites. The development of an organic shell not only improves interface compatibility between the polymer matrix and inorganic fillers, it can also prevent the inner core from agglomerating and thus improve filler dispersion. As an example, dopamine has been used for surface modification of a variety of filler particles[80] due to its versatile "adhesive" properties and its ability to readily form a polydopamine layer *via* self-polymerization at ambient conditions. Dopamine modified $BaTiO_3$ nanofibers have an amorphous layer with a thickness of ~5 nm, which have resulted in an improvement of relative permittivity by ~20% and breakdown strength by ~100% compared to epoxy composites with $BaTiO_3$ nanofibers.[73] The use of physically adsorbed organic modifiers leads to the presence of free residual species in the composite, which can lead to increased leakage currents and increased dielectric loss.[75,81] In contrast, chemically grafted polymer layers may overcome this problem due to its covalently bonded nature.[82,83]

Fluoro-polymers, such as PVDF and its copolymers, are generally immiscible with a number of inorganic fillers due to their low surface energy. Although a number of strategies have been used to modify nanofillers using a hydrocarbon modifier, this continues to result in filler agglomeration and the creation of voids and defects in the nanocomposite films which can initiate dielectric breakdown.[84] To overcome this challenge, a fluoro-phosphonic acid has been used to engineer the surface of $BaTiO_3$ nanoparticles, and effectively reduce its surface energy. This resulted in a good dispersion of the nanoparticles in poly(vinylidene fluoride-*co*-hexafluoro propylene) (P(VDF–HFP)) based composites.[85] In addition, a series of core–shell structured $BaTiO_3$@fluoro-polymer hybrid nanoparticles with a variety of shell structures and thicknesses were prepared *via* a surface-initiated Reversible Addition–Fragmentation Chain Transfer Polymerization (RAFT) polymerization, which led to uniformly dispersed $BaTiO_3$ nanoparticles in the polymer matrix and thereby improved the electrical properties of the nanocomposites.[86] These reports demonstrate that the use of a fluoro-polymer is a promising route to modify and engineer the surface of ceramic fillers. The fluorine atoms from the modifier and matrix can reduce the mismatch of interfacial properties, and since fluorine atoms possess a high electronegativity they can easily form hydrogen bonds with hydrogen atoms from the modifiers and polymer matrix.

The organic modifiers described above with long hydrocarbon chains generally possess a lower relative permittivity compared to ceramic fillers and the PVDF homopolymer or copolymer matrix. It has been shown that a large difference in relative permittivity between an inorganic ceramic filler and the polymer matrix leads to an inhomogeneous electric field distribution, since electric fields tends to concentrate in phases of low permittivity.[40,41] Therefore, the introduction of a

Table 3 Summary of the range of modifiers used for filler surface modification in dielectric nanocomposites. The filler type, filler morphology and polymer matrix are also indicated

Filler	Morphology of the fillers	Polymer matrix	Modifier	Method	Ref.
$BaTiO_3$	0D	P(VDF–HFP)	Phosphonic acid	Surface absorption	76
$BaTiO_3$	0D	PVDF	Carboxylic acids	Surface absorption	96
$BaTiO_3$	0D	Poly(vinyl alcohol) (PVA)	Gallic acid (GA)	Surface absorption	97
$BaTiO_3$	0D	PVDF	Polyvinylprrolidone (PVP)	Surface absorption	98
$BaTiO_3$	0D	PVDF	Titanate coupling agent	Surface absorption	99
$BaTiO_3$	0D	PVDF	PVP	Surface absorption	100
$Ba(Fe_{0.5}Ta_{0.5})O_3$	0D	PVDF	Dopamine	Polycondensation	101
$BaTiO_3$	0D	Poly(vinylidene fluoride-*co*-chlorotrifluoroethylene) (P(VDF–CTFE))	GA	Polycondensation	102
$BaTiO_3$	0D	PVDF	Polydopamine	Polycondensation	73
SiO_2	0D	P(VDF–HFP)	Fluoride 1*H*,1*H*,2*H*,2*H*-perfluorooctyltriethoxy-silane	Grafting to	103
$BaTiO_3$	0D	P(VDF–HFP)	Hydantoin epoxy	Grafting to	104
$BaTiO_3$	0D	Glycidyl methacrylate functionalized P(VDF–HFP)	Amino-terminated silane molecules	Grafting to	105
Al_2O_3	0D	Polypropylene	Phosphonic acid-terminated poly(ethylene-*co*-1-butene)	Grafting to	106
$BaTiO_3$	0D	Poly(vinylidene fluoride-trifluoroethylene-chlorotrifluoroethylene (P(VDF–TrFE–CTFE))	Poly(2,5-bis[(4-trifluoromethoxyphenyl) oxycarbonyl]styrene) (PTFMPCS)	Grafting from	107
$BaTiO_3$	0D	Poly(methyl methacrylate) (PMMA)	PMMA	Grafting from	108
$BaTiO_3$	0D	Poly(2-hydroxylethyle methacrylate) (PHEMA)@PMMA	PHEMA@PMMA or poly(acrylate)sodium@PHEMA	Grafting from	109
$BaTiO_3$	0D	PMMA	PMMA	Grafting from	110
$BaTiO_3$	0D	Poly(vinylidene fluoride-trifluoroethylene-chlorofluoroethylene) (P(VDF–TrFE–CFE))	Hyperbranched aromatic polyamide (HBP)	Grafting from	111
$BaTiO_3$	0D	HBP@PMMA	HBP@PMMA	Grafting from	83
$BaTiO_3$	0D	P(VDF–HFP)	Poly(trifluoroethyl acrylate) (PTFEA)	Grafting from	86
$BaTiO_3$	0D	Polystyrene	Polystyrene	Grafting from	112
$SrTiO_3$	1D	PVDF	PVP	Surface absorption	113
$BaTiO_3$	1D	P(VDF–HFP)	Fluoro-polydopamine	Surface absorption	114
$Ba_{0.8}Sr_{0.2}TiO_3$	1D	PVDF	Ethylenediamine	Surface absorption	115
$BaTiO_3$	1D	P(VDF–TrFE–CFE)	Ethylenediamine	Surface absorption	116
$SrTiO_3$	1D	PVDF	Dopamine	Polycondensation	117
$0.5Ba(Zr_{0.2}Ti_{0.8})O_3$–$0.5(Ba_{0.7}Ca_{0.3})TiO_3$	1D	PVDF	Polydopamine	Polycondensation	118
$Ba_{0.6}Sr_{0.4}TiO_3$	1D	PVDF	H_2O_2	Oxidation	119,120
MWCNT	1D	Polypropylene	Poly(ethylene-*co*-butylene)–OH	Grafting to	121
MWCNT	1D	P(VDF–HFP)	Methoxypolyethylene glycol (mPEG)	Grafting to	122
$NaNbO_3$	1D	PVDF	Polydopamine	Polycondensation	123
$BaTiO_3$	1D	P(VDF–HFP)	PMPCS	Grafting from	124
$Na_2Ti_3O_7$	1D	P(VDF–HFP)	PMPCS	Grafting from	125
Reduced graphene oxide (RGO)	2D	PVDF	PVA	Surface absorption	126
$BaTiO_3$/graphene	2D	P(VDF–HFP)	Polydopamine	Polycondensation	127
Graphene oxide	2D	Nitrile butadiene rubber	γ-Aminopropyl triethoxysilane	Condensation reaction	128
Boron nitride	2D	PVDF	Hydroxyl groups	Oxidation	71
Graphene-oxide	2D	PI	*p*-Phenylenediamine	Grafting to	129
Graphene	2D	Poly(*p*-phenylene benzobisoxazole)	Hyperbranched aromatic polyamide	Grafting from	130

high-permittivity inorganic filler will lead to a decrease in the composite breakdown strength as a result of an electric field concentration formed in the interfacial region. Therefore, the ability to decrease the permittivity contrast between the filler and polymer matrix of a nanocomposite is potentially an effective route to enhance the breakdown strength and energy storage density; see eqn (1). This can be achieved by introducing a low-permittivity ceramic shell layer on the surface of the high-permittivity nanofiller to mitigate the permittivity mismatch between the filler particle and polymer matrix. A number of examples are shown in Table 4, which demonstrate that TiO_2,[87] Al_2O_3,[88,89] and SiO_2,[90–93] have been often chosen as the buffer layer due to their intermediate relative permittivity which is of a magnitude between that of the high-permittivity filler and low-permittivity polymer matrix. Fig. 6 shows the microstructure of 2D Bi_2Te_3@Al_2O_3 nanoplates, where a uniform Al_2O_3 shell has been successfully formed on the surface.[89] The materials selected also exhibit a low dielectric loss; for example Al_2O_3, $\varepsilon_r \sim 10$,[94] SiO_2, $\tan\delta \sim 0.0002$.[95]

Table 4 Summary of the range core–shell fillers with inorganic ceramic or carbon shells. The core material and its morphology, the shell materials and the polymer matrix are indicated

Core	Morphology of the filler	Shell	Matrix	Method	Ref.
$BaTiO_3$	0D	TiO_2	P(VDF–HFP)	Hydrothermal	131
Ag	0D	TiO_2	Polytetrafluoroethylene	Sol–gel	133
$BaTiO_3$	0D	Al_2O_3	PVDF	Heterogeneous nucleation	88
Ceramic	0D	Al_2O_3	Polyolefin	Metallocene polymerization	134
$BaTiO_3$	0D	Fe_3O_4	PVDF	Chemical precipitation	135
$BaTiO_3$	0D	Fe_3O_4	PVDF	Chemical precipitation	136
CCTO	0D	Fe_3O_4	PI	Hydrothermal	137
$BaTiO_3$	0D	SiO_2	PVDF	Hydrolysis reaction	91
$BaTiO_3$	0D	SiO_2	PVDF	Stöber method	95
Zn	0D	ZnO	PVDF	Calcination	138
$BaTiO_3$	1D	TiO_2	PVDF	Hydrothermal	139
$BaTiO_3$	1D	TiO_2	PVDF	Electrospinning	140
$BaTiO_3$	1D	TiO_2	PVDF/P(VDF–HFP)	Electrospinning	141
$BaTiO_3$	1D	TiO_2	P(VDF–HFP)	Kinetics-controlled coating	142
$BaTiO_3$	1D	Al_2O_3	PVDF	Electrospinning	143
$BaTiO_3$	1D	Al_2O_3	PVDF	Electrospinning	94
SiC	1D	SiO_2	PVDF	Sol–gel	144
Bi_2S_3	1D	SiO_2	PVDF	Sol–gel	145
BZT–BCT	1D	$CoFe_2O_4$	PVDF	Sol–gel and electrospinning	146
$BaTiO_3$	1D	SiO_2	PI	Electrospinning	147
$BaTiO_3$	1D	SiO_2	PVDF	Hydrolysis reaction	92
Bi_2Te_3	2D	Al_2O_3	PVDF	Sol–gel	89
Bi_2Te_3	2D	SiO_2	P(VDF–HFP)	Sol–gel	90
$BaTiO_3$	0D	C	P(VDF–HFP)	CVD	148
SiO_2	0D	RGO	Epoxy	Electrostatic assembly	149
$BaTiO_3$	0D	Ag	PVDF	Deposition	150
Ag	1D	C	PVDF	Hydrothermal	151
$BaTiO_3$	0D	Ag@polydopamine	P(VDF–HFP)	Chemical precipitation and absorb	152
TiO_2	1D	C@SiO_2	PVDF	CVD and sol–gel	153
$BaTiO_3$	1D	TiO_2@Al_2O_3	PVDF	Electrospinning	154
$BaTiO_3$	1D	Polydopamine–Pt	P(VDF–HFP)	Polycondensation and reduction reaction	155

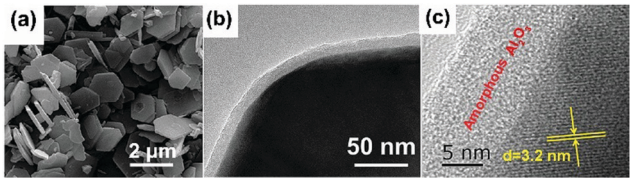

Fig. 6 (a) SEM image of 2D Bi_2Te_3 nanoplates; (b) TEM image, and (c) HRTEM image of 2D Bi_2Te_3@Al_2O_3 nanoplates. Reproduced from ref. 89 with permission from the Royal Society of Chemistry.

Rahimabady *et al.*[87] prepared P(VDF–HFP) based nanocomposites using TiO_2 coated $BaTiO_3$ nanoparticles ($BaTiO_3$@TiO_2). The relative permittivity, ε_r, of the P(VDF–HFP) nanocomposite with 50 vol% $BaTiO_3$@TiO_2 at 1 kHz was increased to $\varepsilon_r \sim 110$, which is over three times higher than $BaTiO_3$/P(VDF–HFP) nanocomposites due to the strong interfacial interaction and space charge accumulation at interfaces. The enhanced polarization was attributed to a highly interactive interface between the multiple dielectric materials due to the introduction of an intermediate TiO_2 layer. The results showed that nanocomposites with a core–shell structured filler achieved a higher breakdown strength compared to $BaTiO_3$/P(VDF–HFP) nanocomposites. The reasons for the improved breakdown strength include the introduction of an inorganic TiO_2 shell with an intermediate relative permittivity between the $BaTiO_3$ filler and P(VDF–HFP) matrix, which reduced the local electric field concentration. The TiO_2 shell was also thought to tightly adhere to the polymer matrix and both factors can act to enhance the breakdown strength of the nanocomposites. As an alternative approach, a graded dielectric filler was proposed by Huang *et al.*[131] to overcome the paradox of attempting to achieve an improved breakdown strength and increased relative permittivity in nanocomposite systems. This included the use of a shell layer with an intermediate relative permittivity (such as TiO_2, $\varepsilon_r \sim 40$), a high-permittivity core ($BaTiO_3$, $\varepsilon_r \sim 1000$) and a polymer matrix (*e.g.* P(VDF–HFP), $\varepsilon_r \sim 10$). The use of a gradient of dielectric fillers resulted in not only an enhanced interfacial polarization induced by the TiO_2 nanowire layer grown on the $BaTiO_3$ nanoparticles, but also improved the breakdown strength by smoothing the inhomogeneous electric field distribution within the composite.

In addition to inorganic dielectrics at the interface, inorganic conductive materials, such as carbon, have been considered as a novel interfacial modifier to modulate the performance of dielectric nanocomposites. Yang *et al.* prepared a novel core–shell structure including TiO_2 nanowires that acted as a core and a conductive carbon layer as the shell which was formed by a hydrothermal reaction and chemical vapor deposition (CVD) processes, as shown in Fig. 7.[132] From the SEM image of the TiO_2@C, it was found that the carbon layer on the surface of TiO_2 nanowires was compact and smooth, and the interface thickness could be precisely modulated by controlling the duration of the CVD process. It is of interest to note that this work discovered a novel strategy to tailor the dielectric properties of PVDF based nanocomposites by

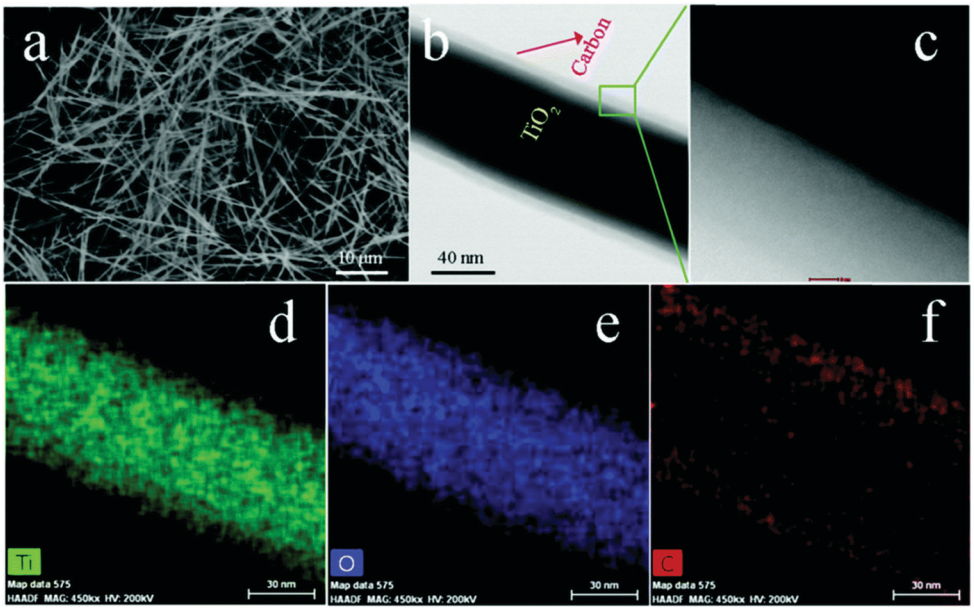

Fig. 7 (a) SEM image of TiO_2 nanowires, (b) TEM image, (c) high-angle annular dark field (HAADF) pattern of a TiO_2 nanowire coated by C layer, (d–f) Mapping images of Ti, O, and C elements. Reproduced from ref. 132 with permission from the Royal Society of Chemistry.

tuning the carbon shell thickness. In addition, a novel percolative dielectric nanocomposites was formed with enhanced relative permittivity by introducing a small loading level of TiO_2@C nanowires; for example, the highest relative permittivity achieved was to $\varepsilon_r \sim 2171$ at 1 kHz, which was 80 times higher than the composite fillers with untreated TiO_2 nanowires at the same filler loading level.

2.3 Building hierarchical interfaces

Interfacial polarization is a dominant factor affecting the performance of polymer nanocomposites,[57,156] due to the mismatch in relative permittivity and electric conductivity of the interfacial layer between the polymer matrix and filler particles.[129,130] As discussed in Sections 2.2 and 2.3, simple core–shell structures formed using organic or inorganic modifiers are effective routes to improve energy storage performance. This core–shell approach can be enhanced by the use of multiple-shells to provide a hierarchical functional interface layer. Such as structure, as shown in Fig. 2, can further assist in the dispersion, polarization, buffering, or shielding. For example, the use of an outer dispersion layer can contribute to the dispersion and interfacial interaction of the ceramic fillers in the polymer nanocomposites, while an inner polarization layer can act to increase the relative permittivity of the nanocomposites. Additional buffer layers can relieve the local electric field concentrations due to a permittivity mismatch, and a shielding layer can also act to prevent the mobility of free electrons, resulting in suppression of the dielectric loss and electric conductivity in the polymer nanocomposites.[157] Therefore, the design and manufacture of hierarchical interfaces can provide novel core–shell architectures with multi-functional roles in polymer nanocomposites.

Recently, a core–multi-shell structure $BaTiO_3$@TiO_2@Al_2O_3 nanowire has been developed to improve the performance of nanocomposites, whereby the individual shells possess a different relative permittivity or electric conductivity.[110] Due to the decrease in relative permittivity between the $BaTiO_3$ ($\varepsilon_r \sim 1000$), TiO_2 ($\varepsilon_r \sim 110$), Al_2O_3 ($\varepsilon_r \sim 10$), and PVDF ($\varepsilon_r \sim 8$), the composites incorporated with $BaTiO_3$@TiO_2@Al_2O_3 nanofibers exhibited a decreased dielectric loss, enhanced relative permittivity, and enhanced breakdown strength compared with composites with only $BaTiO_3$ nanofibers or $BaTiO_3$@TiO_2 nanofibers.[143,158] In addition, a novel structure with hierarchical interfaces based on $NaNbO_3$@dopamine–Ag nanofibers were employed in PVDF based nanocomposites, as shown in Fig. 8. Compared with composite with $NaNbO_3$ or $NaNbO_3$@dopamine nanofibers, the composite with $NaNbO_3$@dopamine–Ag nanofibers achieved an enhanced energy density (16.04 J cm^{-3} at 485 MV m^{-1}) and suppressed energy loss.[159] In addition, Gupta *et al.* designed polydopamine functionalized core@double-shell nanoparticles which included a TiO_2 nanoparticle core and a $BaTiO_3$–TiO_2 double-shell (defined as TiO_2–$BaTiO_3$–TiO_2@dopamine) as

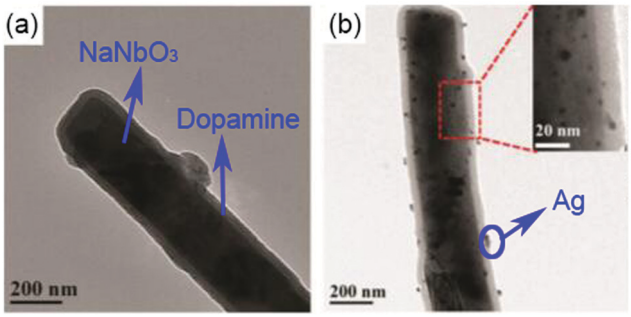

Fig. 8 TEM images of (a) $NaNbO_3$@dopamine nanofibers, and (b) $NaNbO_3$@dopamine–Ag nanofibers. Reproduced from ref. 160 with permission from the Royal Society of Chemistry.

fillers to incorporate into a polymer matrix. Due to the mismatch of electrical conductivity and relative permittivity between TiO_2 and $BaTiO_3$, each TiO_2–$BaTiO_3$–TiO_2@dopamine nanoparticle acted as an individual capacitor. This resulted in the core/outer TiO_2 shells acting as capacitor plates because of their high electrical conductivity ($\sim 10^{-4}$ S m^{-1}) and the $BaTiO_3$ layer acting as a dielectric due to its high permittivity ($\varepsilon_r > 200$). The use of a double shell configuration aided in tailoring the interface, and resulted in enhanced polarization, breakdown strength and suppressed leakage currents for the composites employing TiO_2–$BaTiO_3$–TiO_2@dopamine nanoparticles.[160]

A novel percolative nanocomposite with high relative permittivity and low dielectric loss was formed by introducing multi-phase hierarchical fillers, including dopamine modified barium strontium titanate (BST) nano-cuboid decorated functionalized graphene sheets.[161] The dopamine acted as an adhesion layer to improve the interfacial bonding between the fillers and the polymer matrix, while the BST nano-cuboid layer acted as an isolation layer to prevent the graphene from making contact with each other to minimise electrical conductivity and dielectric loss. In addition, due to increased interfacial polarization of the hierarchical interfaces between the BST, graphene, dopamine, and P(VDF–HFP), the nanocomposites achieved a high relative permittivity of $\varepsilon_r \sim 170.4$ and low dielectric loss of 0.114 at 1 kHz.

2.4 Sandwich- and multi-layer structures

The above sections have indicated that a variety of core–shell structures that are created at a range of dimensions, see Fig. 2 and 3, can enhance the performance of dielectric nanocomposites due to an improved dispersivity and compatibility of the fillers in polymer matrix. However, the breakdown strength of the nanocomposites is often reduced with an increase of inorganic filler loading level. This is particularly true in 0–3 type nanocomposites (namely zero dimensionally connected filler particles in a three-dimensionally connected polymer matrix), where the filler loading levels can be as high as 50–60 vol%. Recently, the building of topological-structures including sandwich or multi-layer structures has been considered in the form of 2–2 type composite, where two dimensional connected fillers are dispersed in a two dimensional connected polymer matrix, by introducing an additional insulating layer into the composites; see Fig. 2. This approach provides an intriguing new strategy to enhance or maintain breakdown strength, while increasing relative permittivity.[162–165]

Pristine polymers, such as P(VDF–HFP),[166] PVDF,[167–169] P(VDF–TrFE–CFE),[170] and PMMA, and acrylic rubber (EDs)[171] have been selected as the insulating layer, which is due to their inherent high dielectric strength and low loss. Zhang *et al.*[166] prepared sandwich-structured composites that consisted of a pure poly(vinylidene fluoride-*co*-hexafluoropropylene) (P(VDF–HFP)) central layer and $BaTiO_3$/P(VDF–HFP) upper and lower layers formed by spin-coating, and the three individual layers were stacked to form a sandwich-structure. The thickness of the central layer was modulated to investigate the effects of central layer thickness on the effective properties of the composites. However, this type of sandwich-structured composite often suffers from a low relative permittivity and polarization due to the central polymer layer being of low relative permittivity, which limits the overall energy density. To overcome this issue, a small amount of ceramic nanofiller, such as $NaNbO_3$ platelets,[172] $(Na_{0.5}Bi_{0.5})_{0.93}Ba_{0.07}TiO_3$ platelets,[78] $BaTiO_3$ nanoparticles,[173] $BaTiO_3$ nanofibers,[162] boron nitride nanosheets (BNNs),[174,175] and $BaSrTO_3$ (BST) nanofibers,[115] have been incorporated into the polymer central layer to create an insulating layer with enhanced relative permittivity. As an example, Wang *et al.*[176] presented a trilayer-structured nanocomposite prepared by hot pressing. The three individual layers were PVDF/BNNs, PVDF/BST, and PVDF/BNNs nanocomposites, respectively. A small amount of $BaSrTO_3$ nanofibers was introduced to the PVDF polymer matrix in the central layer and compared to a sandwich structure with a pure PVDF central layer. The BST/PVDF nanocomposite exhibited improved relative permittivity from $\varepsilon_r \sim 9.3$ to $\varepsilon_r \sim 14.2$. As a result, a discharge energy density of 20.5 J cm^{-3} was achieved due to the contributions of an enhanced breakdown strength by the BNNs/PVDF outer layer and improved relative permittivity of the BST/PVDF central layer.

Recently, a layered-structure was designed in order to achieve a large electric displacement and high breakdown strength.[173] This three-tiered PVDF-based nanocomposite was prepared by gradually increasing the $BaTiO_3$ nanoparticle loading level layer-by-layer, as shown in Fig. 9. Due to the graded $BaTiO_3$ nanoparticle loading level, a weak electric field region was formed that acted as an efficient insulating barrier, which effectively increased the breakdown strength of the nanocomposite compared with a nanocomposite containing homogeneously dispersed $BaTiO_3$ nanoparticles.

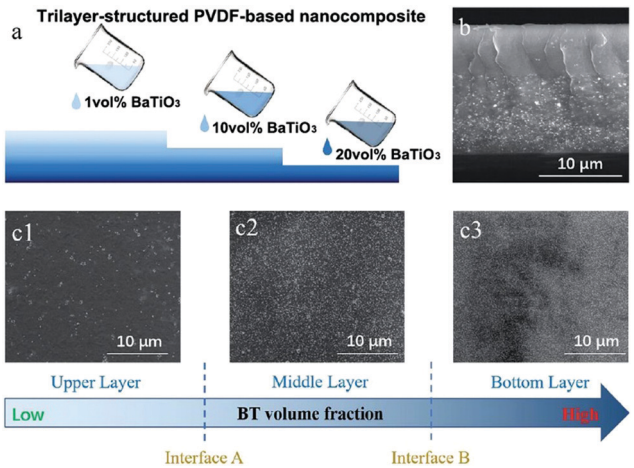

Fig. 9 (a) Fabrication process of the trilayer-structured nanocomposite, (b) cross-sectional SEM image of the nanocomposite, (c1–c3) SEM images of the upper, middle and bottom layers with different $BaTiO_3$ nanoparticle loading levels. Reproduced from ref. 173 with permission from the Royal Society of Chemistry.

3. Methods to control the interfacial layer in nanocomposites

The previous section has described the range of architectures used to tailor the interface such as core–shells, hierarchical core–shells and sandwich or multi-layer structures. This section overviews the processing methods used to create and control such interfaces.

3.1 Preparation of core–shell structures by organic flexible polymer shells

Many modifiers are coated on the surface of inorganic fillers simply *via* physical adsorption due to the lack of functional groups. A physical coating can be achieved by mixing the modifiers and fillers in solvents while under the action of mechanical stirring or ultrasonication.[146] Deng and co-workers reported a ternary PVDF nanocomposite with dopamine modified $BaTiO_3$ nanoparticles and γ-aminopropyl triethoxysilane (KH550) modified Bi_2S_3 nanorods.[177] The dopamine surfactant and KH550 were diluted in deionized water and potassium hydrogen phthalate buffer solution, respectively, then mixed with the ceramic filler by simple stirring. The processed hybrid fillers were incorporated into the polymer matrix to prepare PVDF composites by a casting method, as shown in Fig. 10.

As discussed in Section 2.2, physically adsorbed surfactants often leave free residual species in the composites, resulting in a high leakage current and dielectric loss. To solve this problem, covalently bonding organic modifiers *via* "grafting to" or "grafting from" approaches have been studied.[178] The "grafting to" approach is particularly suitable for preparing polymer based nanocomposites with a high loading level of ceramic fillers since the shell layer can also be utilized as the polymer matrix.[105] To realise a "grafting to" strategy, active groups of the modifier and the surface of inorganic fillers are both essential elements. Huang *et al.* prepared PS and PMMA with active thiol-terminated end groups by a RAFT polymerization method, which was directly reacted with vinyl-functionalized $BaTiO_3$ nanoparticles to form a core–shell structure.[57] As another example, in the process of preparing a $BaTiO_3$@hydantoin epoxy resin,[104] the epoxy group from the hydantoin epoxy resin was able to react with hydroxyl ions on the surface of $BaTiO_3$ nanoparticles through a ring-opening reaction, and was further cross-linked by a curing agent, namely dipropylenetriamine. The hydantoin epoxy resin modified $BaTiO_3$ nanoparticles exhibited a homogeneous dispersion and strong interfacial adhesion with the P(VDF–HFP) matrix.

Recently, a number of successful processing methods were reported, such as a methoxypolyethylene glycol (mPEG) graft on the surface of carbon nanotubes (CNT) by esterification between the –OH from mPEG and –COOH from CNT. Due to the tight encapsulation of CNT by the mPEG, a high relative permittivity of $\varepsilon_r \sim 69.7$ and a low dielectric loss of 0.042 were simultaneously achieved in a P(VDF–HFP) nanocomposite.[122] Core–shell structured $BaTiO_3$@PS and $BaTiO_3$@PMMA nanocomposites with high relative permittivity and low dielectric loss were prepared by Jiang *et al.*,[82] using a "grafting to" method and thiol–ene click reaction. It was shown that the organic shell layer, including grafting density and molecular weight, can be easily tailored which contributed to a detailed understanding of the structure–dielectric property relationships of the core–shell structured nanocomposites.

The main features of the "grafting from" strategy is to build a shell layer *via* an *in situ* polymerization of monomers *via* the initiating sites on the nanoparticle surface.[109,112,179] Atom Transfer Radical Polymerization (ATRP) and reversible RAFT methods are usually employed in the "grafting from" strategy process. As shown in Fig. 11, poly(2-hydroxylethyle methacrylate) (PMMA), poly(hydroxyethyl methacrylate) (PHEMA) and sodium polyacrylate (PANa) were coated on the surfaces of $BaTiO_3$ nanoparticles by ATRP method, respectively, and core@double-shell structured $BaTiO_3$ nanoparticles were prepared by grafting PHEMA-*block*-PMMA and PANa-*block*-PHEMA block copolymer using ATRP method. For RAFT method, the process is outlined in Fig. 12. Firstly, the RAFT reagent *e.g.* 4-cyanopentanoic acid dithiobenzoate (CPDB) is introduced on the surface of any modified nanoparticles, then the monomer of the modifier polymer initiates *in situ* polymerization by the RAFT reagent. In this method, the thicknesses of the polymer

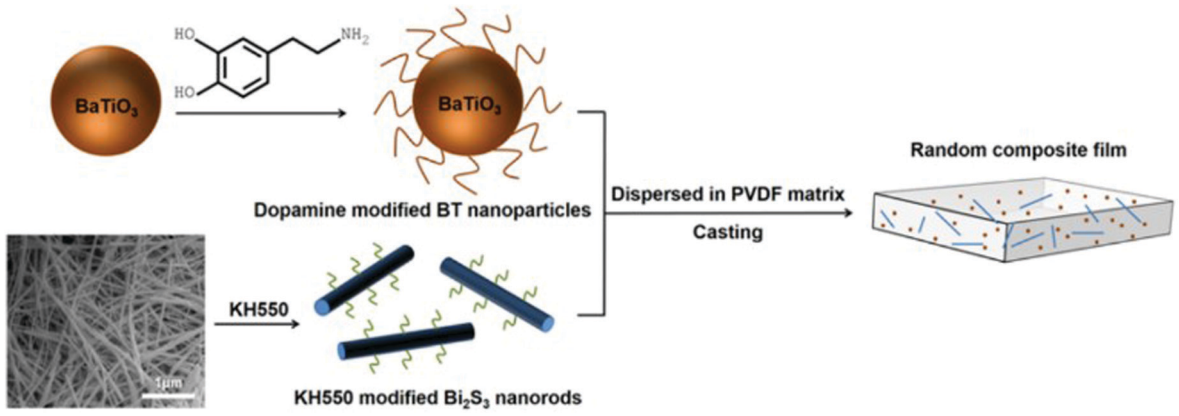

Fig. 10 Schematic of processing procedure of PVDF nanocomposite with dopamine modified $BaTiO_3$ nanoparticles and KH550 modified Bi_2S_3 nanorods. Reprinted from ref. 177, Copyright (2018), with permission from Elsevier.

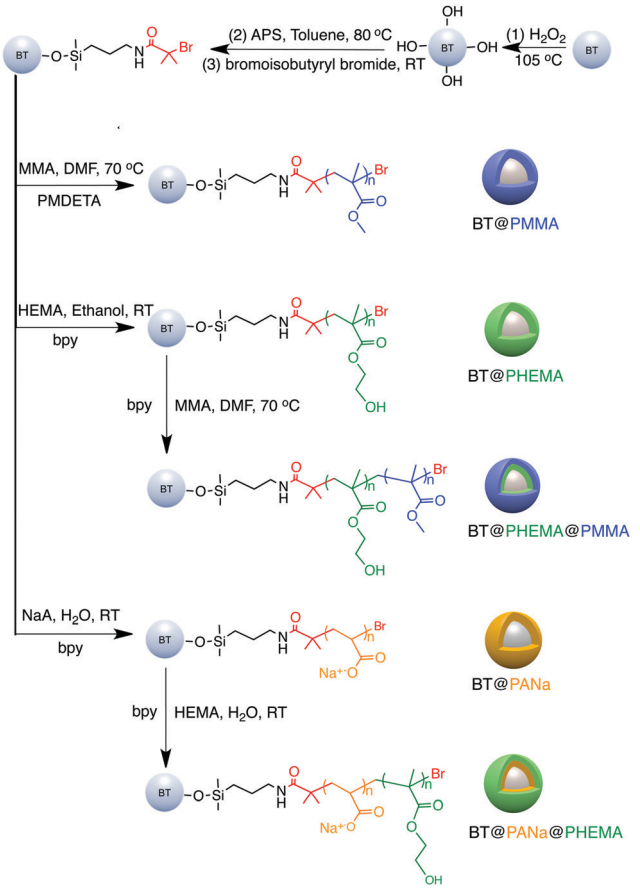

Fig. 11 Synthesis of functionalized $BaTiO_3$ nanoparticles using a "grafting from" strategy. Reprinted with permission from ref. 109. Copyright (2016) American Chemical Society.

shell can be tailored by varying the molecular weight of the grafted polymer. Core–shell structured $BaTiO_3$ nanoparticles with either different shell thickness or different molecular structures were prepared by grafting two types of fluoroalkyl acrylate monomers *via* RAFT polymerization. It was shown that a high energy density and low dielectric loss could be successfully realized in the nanocomposites. Moreover, the energy storage densities of the P(VDF–HFP)-based nanocomposites could be tailored by adjusting the structure and thickness of the fluoro-polymer shell.[86] As an example, nanocomposites with a thick fluoro-polymer shell were prepared using fluoroalkyl acrylate monomers with short side groups, which exhibited a high breakdown field and enhanced energy storage capability in comparison with the pure P(VDF–HFP); for example 6.23 J cm^{-3} for a nanocomposite with 50% $BaTiO_3$–PTFEA2 and 4.10 J cm^{-3} for P(VDF–HFP).

Recently, the reduction of nanoparticle agglomeration and improving their dispersibility in nanocomposites *via* strong bonding,[48,180–191] has led to the development of a viable route to prepare organic–inorganic nanocomposites composed of monodisperse ferroelectric nanoparticles, which were directly bonded with polymers utilizing rationally designed amphiphilic star-like diblock copolymer as nanoreactors. Star-like diblock copolymers, such as poly(acrylic acid)-*block*-poly(vinylidene fluoride) (PAA-*b*-PVDF), were prepared by sequential ATRP and copper-catalysed azide–alkyne cyclo additions. The precursors were selectively incorporated into the space occupied by the inner PAA blocks and converted into $BaTiO_3$ nanoparticles directly and were stably capped with PVDF chains, as shown in Fig. 13. The PVDF-capped $BaTiO_3$ nanoparticles were highly uniform and after hot-pressing the chemically synthesized PVDF-capped $BaTiO_3$ nanoparticles, homogeneous PVDF/$BaTiO_3$ nanocomposites were fabricated. It was found that the PVDF/$BaTiO_3$ nanocomposite filled with 84.7 wt% nanoparticles ($\sim$16 nm) possessed a high relative permittivity of $\varepsilon_r \sim 85$ (at 2 MHz) and dielectric loss of $\sim$0.028. In comparison, pristine PVDF exhibits a relative permittivity of $\varepsilon_r \sim 10$ and dielectric loss of $\sim$0.16. This improvement can be attributed to the large interfacial areas and strong interfacial interactions in the PVDF/$BaTiO_3$ nanocomposite which promote interfacial exchange coupling through a dipolar interface layer, thereby leading to the enhanced polarization, improved relative permittivity and reduced dielectric loss.

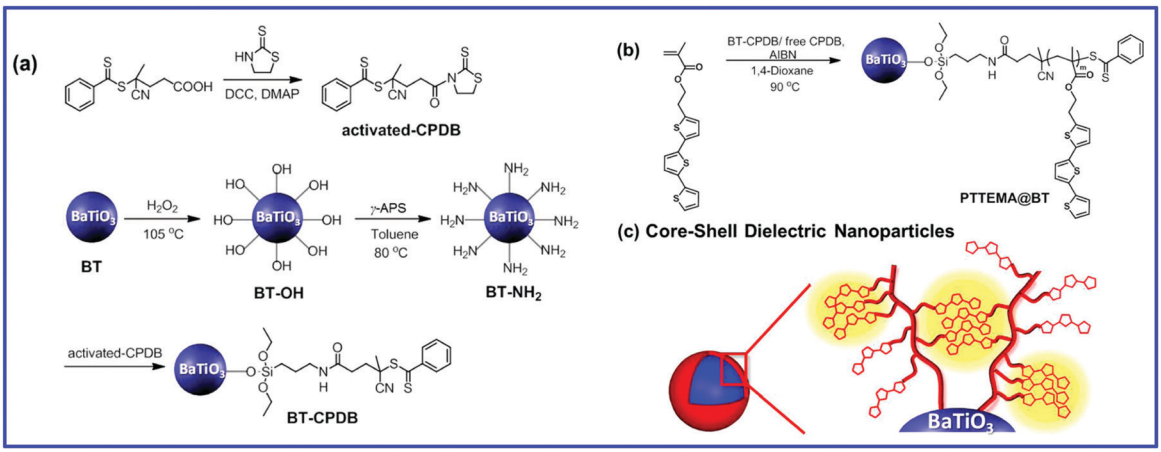

Fig. 12 Synthesis of functionalized $BaTiO_3$ nanoparticles using "grafting from" strategy. Reprinted figure with permission from ref. 179. Copyright (2014) American Chemical Society.

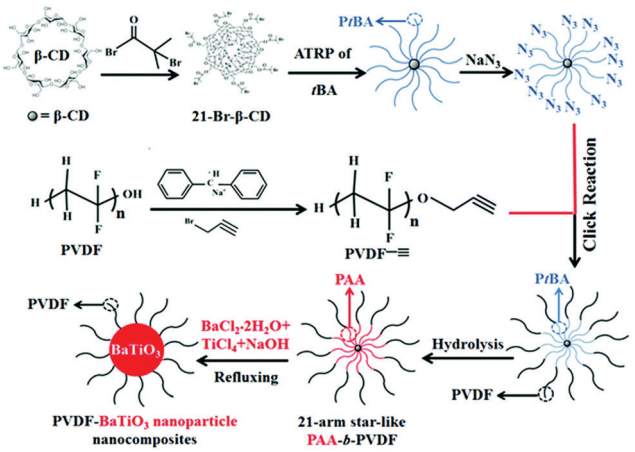

Fig. 13 Synthetic route to amphiphilic 21-arm, star-like PAA-*b*-PVDF diblock copolymer and subsequent conversion into PVDF-capped $BaTiO_3$ nanoparticles and PVDF/$BaTiO_3$ nanocomposites. Reproduced from ref. 48 with permission from the Royal Society of Chemistry.

3.2 Tailoring the interfacial thickness by organic rigid liquid crystalline polymers

The interfacial region can be considered as a shell of a certain thickness on the nanoparticle surface, as shown in Fig. 14a.[36] The volume fraction of the interfacial region ($f_{\text{interface}}$) of a spherical nanocomposite filler can be calculated by eqn (2):

$$f_{\text{interface}} = f_{\text{particle}}\left[\left(1+\frac{2t}{d}\right)^3 - 1\right] \quad (2)$$

where t is the interfacial thickness, d is the diameter of the nanoparticle and f_{particle} is the volume fraction of the filler. As shown in Fig. 14b, the magnitude of $f_{\text{interface}}$ will be significantly increased with an increase of interfacial layer thickness and a decrease of nanoparticle diameter. Therefore, the interfaces and interfacial layer thickness between the ceramic filler and polymer matrix is a dominant factor that influences the effective electric properties of nano-scale based composites and ultimately their properties and performance in storage applications.[192] However, control of the interfacial layer thickness and understanding the detailed effects of interfacial regions on the dielectric properties and energy storage density of the nanocomposites continues to be a challenge.

As discussed in Section 3.1, many of the polymers employed as interfacial modifiers are flexible organics, which generally have a random walk or Gaussian coil chain shape due to the flexibility of their molecular backbone.[58,193,194] The interfacial thickness tends to be proportional to the molecular weight of polymer, however, it cannot be precisely calculated *via* the average degree of polymerization of the polymer. Rigid chain structures, *i.e.* π-conjugation along the polymer backbone (semiconducting polymers), helical secondary structures (biomolecules), aromatic groups (aramid and aromatic polyester high-performance resins) or mesogen-jacketed liquid crystalline polymers, all lead to the adoption of extended and rigid chain conformations. Among them, the mesogen-jacketed liquid crystalline polymers can be synthesized by a living radical polymerization and the polymer-chain length can be tailored by controlling the degree of polymerization, thereby resulting in an interfacial modified thickness that can be accurately controlled by design of the degree of polymerization of the mesogen-jacketed liquid crystalline polymers; as shown in Fig. 15.[193,195]

Kuang and Xie *et al.*[196] successfully grafted a liquid crystalline polymer with azobenzene mesogens as the side chain to

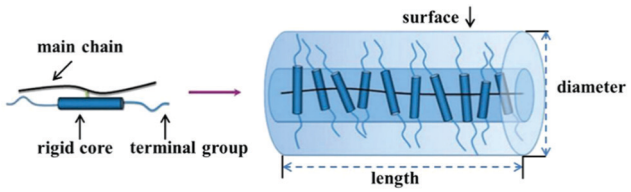

Fig. 15 Schematic of a rod-like mesogen-jacketed liquid crystalline polymers (MJLCP). Reproduced from ref. 193 with permission from the Royal Society of Chemistry.

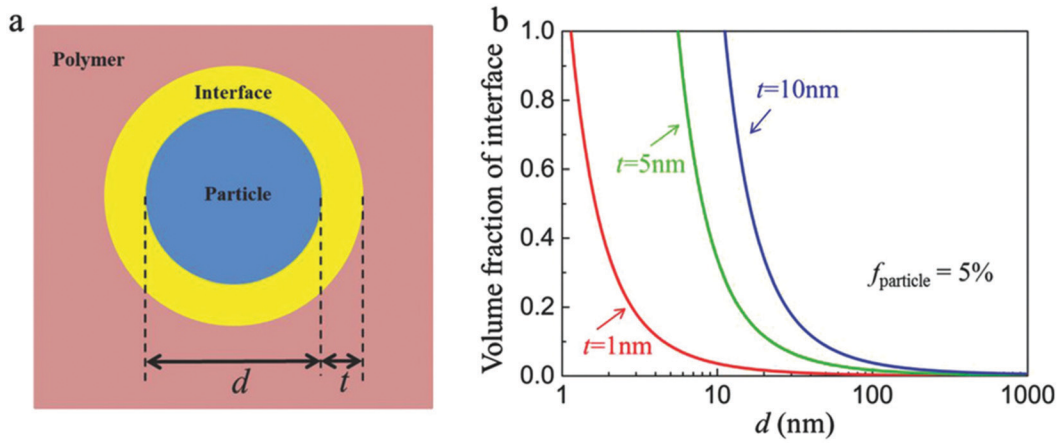

Fig. 14 (a) Schematic of the ceramic/polymer interface structure in a nanocomposite. (b) Volume fraction of interface in the nanocomposites with the diameter of nanoparticles and interface thicknesses. Reproduced with permission from ref. 36. Copyright 2018, John Wiley and Sons.

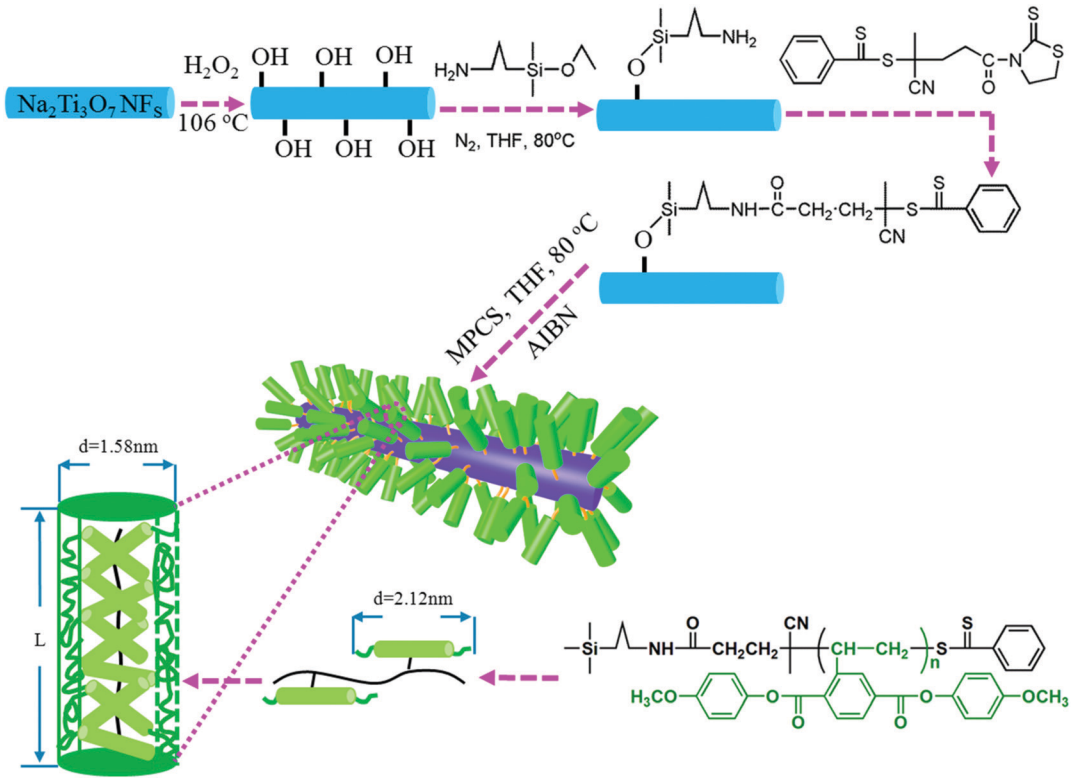

Fig. 16 Modulation of the interfacial layer thickness on $Na_2Ti_3O_7$ nanofibers by rigid polymer PMPCS. Reprinted with permission from ref. 125. Copyright (2017) American Chemical Society.

golden nanoparticles by the two-phase Brust–Schiffrin method. In addition, Luo *et al.*[125] utilized a liquid-crystalline polymer, PMPCS to design and tailor the interfacial region, and focused on the effects of the interfacial layer thickness between a $Na_2Ti_3O_7$ nanofiber filler and the polymer matrix on the performance of the nanocomposites, as shown in Fig. 16. PMPCS is a rigid polymer with crowded, and bulky side groups connected with the main chain through a short spacer or with a single covalent bond.[197,198] These interesting features lead to the PMPCS forming a rigid polymer structure, and when the molecular weight of the PMPCS is greater than 10^4, the main chain is constrained to form a straight conformation. The size of the straight conformation unit can be calculated by eqn (3):[199,200]

$$L_{rod} = 0.154\ (nm) \times 2N_{rod} \times \sin 52^\circ \approx 0.24N_{rod}\ (nm) \quad (3)$$

As shown in Fig. 14, a mace-like structure is formed, including "sticks" that originate from the $Na_2Ti_3O_7$ nanofibres and "spikes" that originate from the rigid PMPCS columnar units. The size of the mace-like structure could be tailored by the length and diameter of $Na_2Ti_3O_7$ nanofibres, as well as the length of PMPCS column units. The PMPCS column units were grafted onto the $Na_2Ti_3O_7$ nanofibre surface *via* a RAFT *in situ* polymerization method, and the length of the PMPCS column units was determined by eqn (3). It is of interest to note that the prepared $Na_2Ti_3O_7$@PMPCS/P(VDF–HFP) nanocomposites showed an increased relative permittivity from $\varepsilon_r \sim 10.7$ to $\varepsilon_r \sim 69.6$ at 1 kHz with a change in thicknesses from 9 nm to 25 nm of the PMPCS shell. This approach provides a route to modulate the properties of the dielectric nanocomposites, in addition to the loading level and ceramic filler type. The authors proposed that the PMPCS layer between the $Na_2Ti_3O_7$ nanofibers and P(VDF–HFP) matrix acted as insulating isolation layer, which prevented the movement of free electrons, and the cumulative free electrons on the interface with the increase in PMPCS layer thickness led to a strong polarization. As discussed in Section 2.2, a fluoro-polymer is an improved modifier to engineer the surface of ceramic fillers compared with hydrocarbon modifier.

A novel liquid-crystalline polymer PTFMPCS was also investigated by introducing fluoro-atoms into the PMPCS to engineer the surfaces of $BaTiO_3$ nanoparticles.[107,201,202] As a result, a significantly improved energy density was achieved by accurate interfacial control using this fluoro-polymer in a polymer nanocomposite. Subsequently, a series of fluoro-liquid-crystalline polymers with three to seven fluoro-atoms were prepared, which were used to engineer the surface of $BaTiO_3$ platelets and nanoparticles and modulate the performance of the composites.

3.3 Formation of a controllable inorganic ceramic shell layer

A number of routes have been used for the preparation of core–shell structures with an inorganic ceramic shell layer of moderate to high relative permittivity to mitigate electric field concentrations at the interface between the filler and matrix.[203] The methods used included sol–gel,[87] hydrothermal,[204]

hydrolysis reaction,[205] coaxial electrospinning,[206] CVD,[153] and the Stöber method.[95] Coaxial electrospinning is a method recently employed; firstly, a homogeneous precursor solution with a designed molar ratio of the raw target nanofibers was prepared by a solution method.[207–210] Secondly, the viscosity of the solution is modulated using polymers, such as poly(vinyl pyrrolidone). Thirdly, the solution is transferred to the syringe of the electrospinning instrument and an appropriate electric field is applied. Finally, the core–shell structured ceramic nanofibers are obtained after an annealing treatment.

Although efforts on preparing core–shell structured fillers with different ceramic shell layers have been made to improve the dielectric and energy storage performance, the effects of ceramic shell layer thickness on the performance of polymer based dielectric nanocomposites is less well explored. Huang *et al.*[142] prepared $BaTiO_3$ nanowires encapsulated by TiO_2 shells of variable thickness by a kinetically-controlled coating method, as shown in Fig. 17. Two kinds of materials with shell layer thickness dimensions of 50 and 110 nm were obtained by tailoring the tetrabutyl orthotitanate content. The performance of the P(VDF–HFP) polymer nanocomposites with $BaTiO_3$@TiO_2 and bare $BaTiO_3$ nanowires were investigated. The results showed that the nanocomposites with $BaTiO_3$@TiO_2 nanofibers achieved significantly improved performance, including higher breakdown strength and energy storage density due to the more uniform electric field distribution and enhanced polarization in the nanocomposites by the moderate TiO_2 buffer layer compared with nanocomposites containing only uncoated $BaTiO_3$ nanofibers. For example, a high energy density of 9.53 J cm^{-3} at 440 kV mm^{-1} was obtained for nanocomposites with core–shell structured nanowires compared to a lower energy density of 5.60 J cm^{-3} at 360 kV mm^{-1} for nanocomposites with 5 wt% uncoated fibers.

It is of interest to note that the energy storage density of nanocomposites can be modulated by the TiO_2 shell thickness. To reveal how the thickness of the TiO_2 buffer layer can affect the properties of the composites, Hu *et al.*[211] prepared $BaTiO_3$@TiO_2 nanoparticles with a modulated TiO_2 shell layer thickness from 0–10 nm. The core–shell structured nanoparticles were prepared *via* a surface coating approach in solution and, following heat treatment, the thickness of the TiO_2 shell layer could be tailored by modulating the amount of the titanate coupling agent employed in the preparation process. The core–shell fillers were incorporated into a PVDF polymer matrix and used for energy storage applications where the dielectric properties, breakdown strength, and energy storage performance of the nanocomposites were strongly related to the thickness of the TiO_2 shell layer. Nanocomposites with a TiO_2 shell layer thickness of 1–3 nm achieved the highest relative permittivity and breakdown strength compared with the nanocomposites with other TiO_2 shell layer thickness. The authors proposed that the introduction of a TiO_2 shell layer on the surface of the $BaTiO_3$ nanoparticle induced a two-charged interface and therefore more electronic charge was captured in the interfacial region to enhance interfacial polarization.

Recently, TiO_2 nanowires with multiple shells including carbon and SiO_2 layers have been prepared.[153] The detailed synthesis procedure is shown in Fig. 18. As shown, TiO_2 nanowires was synthesized by a hydrothermal and calcination method using a raw material of TiO_2 nanoparticles, and the carbon layer was formed on the surface of TiO_2 nanowires using a CVD treatment; the outer shell SiO_2 layer was formed by a sol–gel synthesis method. The composite with TiO_2@C nanowires showed the typical characteristics of a composite containing conductive fillers, where the permittivity and dielectric loss sharply increased with an increase of TiO_2@C nanowire

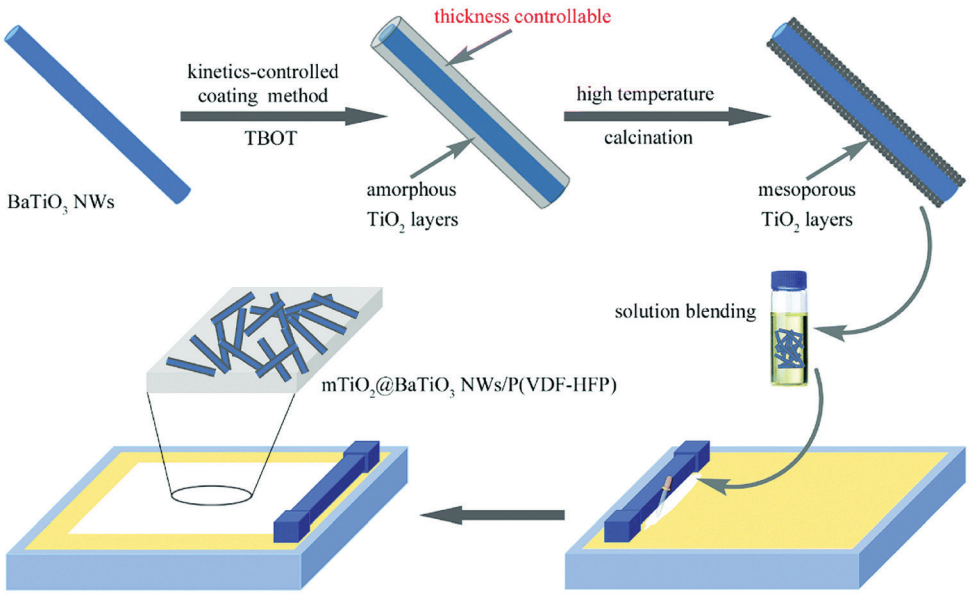

Fig. 17 Preparation process of $BaTiO_3$@TiO_2 nanowires by a kinetics-controlled coating method. Reproduced from ref. 142 with permission from the Royal Society of Chemistry.

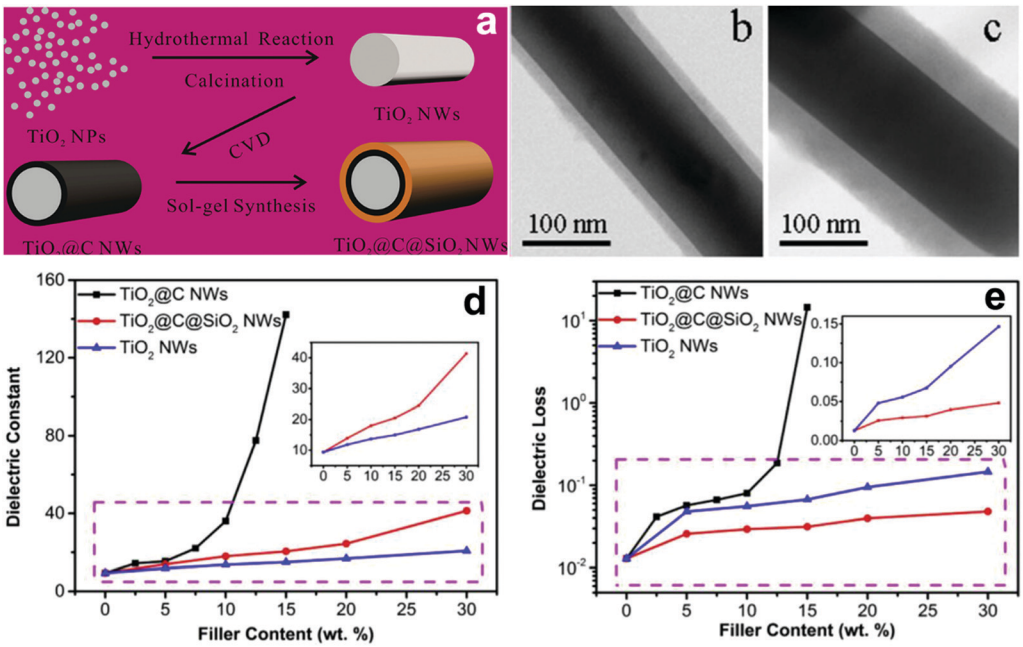

Fig. 18 (a) Schematic of the synthesis of TiO_2@C@SiO_2 nanowires starting with TiO_2 nanoparticles and TEM images of the core–shell structured (b) TiO_2@C and (c) TiO_2@C@SiO_2 nanowire. Relative permittivity (d) and dielectric loss (e) of PVDF-based nanocomposites loaded with TiO_2 nanowires, TiO_2@C nanowires, and TiO_2@C@SiO_2 nanowires as a function of filler content. Reprinted from ref. 153, Copyright (2018), with permission from Elsevier.

loading level, see Fig. 18d and e. The percolation response disappeared when the TiO_2@C nanowires were coated with an insulating SiO_2 layer. As a result, the composites with 30 wt% TiO_2@C@SiO_2 nanowires achieved an enhanced permittivity of $\varepsilon_r \sim 41$ and suppressed dielectric loss of 0.05 at 1 kHz, which were superior to the composites containing only TiO_2 nanowires.

3.4 Characterization of interfaces in polymer nanocomposites

It is well-known that the interfacial region between the nanoparticles and the polymer matrix plays an important role in the electric polarization, mechanical, thermal, and optical properties of nanocomposites. However, it remains a challenge to characterize the interfacial region and its electric properties since the interfacial region cannot be isolated from nanocomposites based on the existing characterization methods, such as dipolar polarization, space charge density and electric field distribution. At present, there are two important methods to study the interfacial region: indirect analysis techniques (theoretical simulation based on experiment results) and direct analysis techniques. For the former, the interphase bonding, interphase density, and thickness can be quantified using Fourier transform infrared spectroscopy (FTIR), transmission electron microscopy (TEM)/thermal gravimetric analysis (TGA). However, FTIR is applicable only to metal–polymer composites in which the interfacial interactions generate considerable changes in the infrared spectrum of the polymer arising from bonding between the two moieties at the interface.[212] Using the data gleaned from TGA/TEM or FTIR and subsequent analysis, the interphase density and thickness could be calculated *via* the number of anchoring points per chain. For the latter, there are limited reported on efforts to directly observe the interface structure and assess their physical properties. For example, Li and He *et al.* have recently detected the local polarization properties at the matrix/particle interface in ferroelectric nanocomposites *via* a modified Kelvin Probe Force Microscopy (KPFM) method with nanoscale spatial resolution. In principle, the surface potential of ferroelectric polymers can be influenced by dipolar polarization and KPFM can be effective in measuring nanoscale variations in the local surface potential at the interface. Compared with the standard KPFM approach, the main features of the modified KPFM include open-loop control and PeakForce Tapping mode imaging; Fig. 19 shows such a setup. The results indicated that the electric polarization in the matrix/particle interfacial region was higher than the polymer matrix under the application of an electric field.[213]

4. Interfacial models, polarization mechanism and simulations

We have seen that nano-sized ceramic fillers embedded in a polymer matrix lead to the formation of a large interfacial region area, which plays an important role in determining the properties of the nanocomposites since the interface has a significant impact on the physicochemical properties of materials.[214–217] In general, the interfacial region in polymer nanocomposites is characterized as a region that extends from the surface of the nanoparticle, through the modification layer and interfacial polymer layers (with modified chain structures), and finally to the host matrix polymer.[36] This section reviews

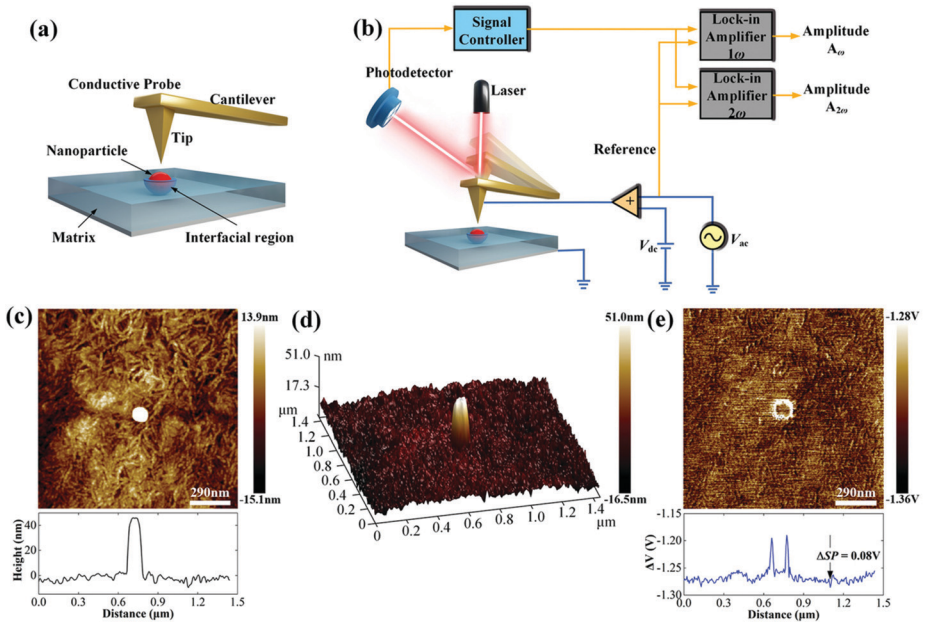

Fig. 19 (a) Schematic of the Kelvin Probe Force Microscopy (KPFM) testing process. (b) Schematic of the working principle. (c) Topography signal near an embedded nanoparticle. (d) 3D image of the surface topography near an embedded nanoparticle. (e) The ΔV signal near an embedded nanoparticle. With permission from ref. 213. Copyright 2019, John Wiley and Sons.

the interfacial models, polarization mechanisms and simulations to examine polymer based nanocomposites.

4.1 Interface models

Usually, ceramic–polymer nanocomposites consist of three regions, the polymer matrix, the ceramic filler and the interfacial layer. It is a challenge to fully characterize and understand the interfacial regions, such as nanoparticle surface states, polymer chain configurations, inorganic/organic compatibility and local interfacial electrical and dielectric behaviour. The development of interface models can enable an improved understanding of interface effects on the electrical and dielectric properties of such nanocomposites. According to previous studies,[218,219] the interface can change the distribution and motion of space charges, resulting in improved polarization, and act as scattering points to prolong carrier path length, thereby improving breakdown strength. Moreover, interfaces often serve as traps for charges and can result in regulated local charge mobility and conductivity. In addition, the modified electronic states of interfaces can create traps or change the depth of traps, which is closely related to the space-charge (interfacial) polarization and breakdown behaviour. Interfaces can also induce a change in the polymer molecular structure that initiates from the interfacial region to the matrix (free volume fraction, mobility, crystallinity, and configuration of polymer chains), which affects the dielectric properties of the polymer matrix.

A variety of interface models have been proposed to describe the interfacial interactions in dielectric nanocomposites, the mode of charge transportation and its effect on electrical properties.[220–222] Tanaka developed a multi-core model to describe the interactions between the polymer and spherical ceramic nanoparticles.[221] In this model, the interfacial layer includes three layers: (i) the bonded layer, (ii) the bound layer and (iii) the loose layer, as seen in Fig. 20a.[4] The bonded layer is based on polymer chains, which are bonded tightly to both the inorganic filler and the polymer network. The interactions holding these chains in place are electrostatic, covalent, hydrogen bonding or van der Waals forces. The bound layer is considered to be ~1 nm thickness and prevents the formation

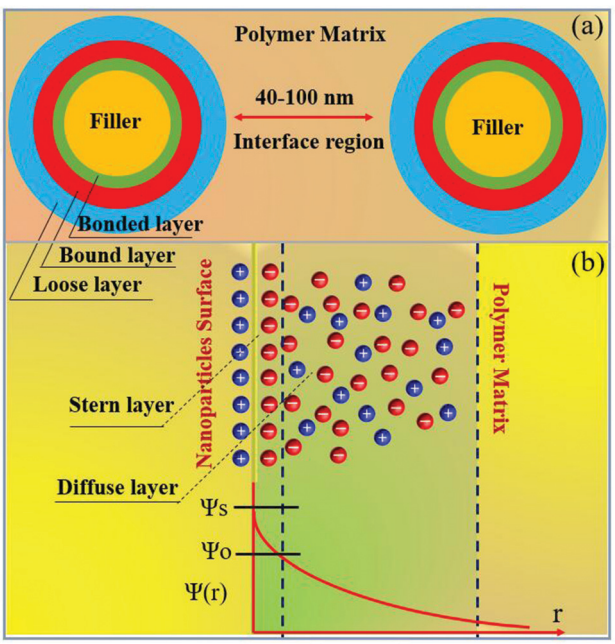

Fig. 20 (a) The multi-core model for polymer nanocomposites, (b) charge distribution of a diffuse electrical double layer.

of polar dipoles, reducing the relative permittivity of the composite. The middle layer of the model is the bound layer. In this layer, the polymer chains interact strongly with the bonded layer and the surface of the filler. Typically, the thickness of the layer ranges from 2 nm to 9 nm, which depend on the interfacial interaction strength of the bonded layer. The polymer chains in the bound layer form structures around the filler nanoparticle that affect chain folding, mobility and conformation. The final layer is termed the loose layer which loosely interacts with the bound layer, leading to a different conformation and mobility to the polymer matrix and can span tens of nanometres. This layer is attributed to the contribution of the reduction in the free volume of the composite. At high filler levels, the loose layers can overlap and this results in an area with combined effects from individual filler particles, thereby increasing the impact that the fillers have on the macroscopic properties of the composites.

Lewis proposed a diffuse electrical double layer model for describing polymer nanocomposites.[220] As shown in Fig. 20b the surface of the nanoparticle becomes charged due to the difference in Fermi levels or chemical potential of the nanoparticles and polymer matrix. This results in screening of ionic charges in the surrounding polymer, which in turn suppresses charge accumulation on the nanoparticles. An electrical double layer consisting of a Stern layer and a Gouy–Chapman diffused layer are formed. When the nanoparticle is positively charged inside the nanocomposite, a layer exhibiting a positive potential ψ_s is formed by the surface states related with immobile charged impurities, trapped carriers, mobile electrons, and holes in the nanoparticle. The negatively charged Stern layer is formed on the nanoparticle surface, which contains small molecules, special absorbed ions, and solvated ions, and cannot move freely. Outside this layer is the Helmholtz plane (OHP) with an electrical potential of ψ_o. Taking TiO_2–$BaTiO_3$–TiO_2@dopamine/PVDF nanocomposite as an example, the Fermi level difference between TiO_2 and $BaTiO_3$ is above 0.5 eV, which results in accumulated space charges on TiO_2 and $BaTiO_3$. The surface charge densities (σ') in different layers of TiO_2–$BaTiO_3$–TiO_2 nanoparticles follow the trend of σ' (TiO_2) core $>$ σ' ($BaTiO_3$) middle layer $>\sigma'$ (TiO_2) outer layer to maintain charge neutrality. The positive charges in the TiO_2 layer in turn develop negative charges on the dopamine layer due to polar interaction. The interfacial charges present in the polymer matrix form a Gouy–Chapman–Stern layer at the interface of TiO_2–$BaTiO_3$–TiO_2 nanoparticles, and the interfacial polarization and permittivity is enhanced.[160]

An extension of the OHP into the polymer matrix is the Gouy–Chapman diffused layer, which is formed around the Stern layer by a distribution of negative and positive ions. This layer potentially works as an ''interaction zone'' to affect the dielectric and electrical properties of the nanocomposite. The distribution of charges in this layer is related to the electrical potential $\psi(r)$ across the interface region. The magnitude of $\psi(r)$ changes with the distance (r) from the particle surface and can be described with a combined Poisson–Boltzmann equation, and the $\psi(r)$ function is shown as follows:

$$\nabla^2\psi(r) = -e\varepsilon^{-1}\sum z_i n_i(\infty)\mathrm{e}^{-z_i e\psi(r)/kT}$$

where ε is the relative permittivity of the medium, k is the Boltzmann constant, z_i and $n_i(\infty)$ are the ion valency and concentration of ion species i in the bulk matrix, respectively. When the potential is small, the $\psi(r)$ can be reduced to the simple Debye–Hückel form, as shown below:

$$\psi(r) = \psi_0\mathrm{e}^{-kr}; k = \left(\frac{2e^2}{\varepsilon kT}\sum_i z_i^2 n_i(\infty)\right)^{1/2}$$

where κ is the Debye–Hückel parameter and has a unit of m^{-1}. The inverse of κ is terms the ''Debye length'', and defines the extent of the exponential decay of the double layer. This equation indicates the variation of potential in the diffused part of the double layer, starting from the Stern layer.

The charge density (ρ_i) in the double layer is expressed as follows:

$$\rho_{i(r)} = \rho_i(\infty)\mathrm{e}^{-z_i e\psi(r)/kT}$$

In addition, at the nanoparticle surface ($r = 0$), the total charge density is given by:

$$\sum_i \rho_i(0) = \sum_i \rho_i(\infty) + \frac{\sigma^2}{2\varepsilon kT}$$

and is associated with the surface conductivity (σ) of the nanoparticles. This equation implies that the charge density, ρ_i, in the double layer can be increased by increasing the σ, which is useful to induce polarization at opposite ends of nanoparticles under an applied electric field since charges at the interfaces are efficiently transferred.

The multi-core model of Fig. 20 and 21a was later modified by Li *et al.*[223] to produce a multi-regional structure model, as shown in Fig. 21b. The bonded region was considered to be rich in charge traps with the deep traps replaced by shallower traps as the distance away from the filler increased. The deep traps prevent charge mobility, reduce space charge and increase the breakdown strength of the nanocomposite.[91]

A different approach to the interface model was developed by Ezzat *et al.*[224] who considered the composite interfaces as a three-phase system, namely filler, polymer matrix and a void between both regions. The model, known as the interphase model, considered the shape and orientation of the filler, rather than assuming a spherical morphology; this is shown in Fig. 21c. The model considered that as the filler concentration increased, the concentration of void spaces also increased in the composite.[225,226] The voids are important since they contribute to the enhancement of mobile charge interference from charge trapping, charge distribution and molecular and ionic relaxation processes at the filler interface.[227]

A bipolar charge-transport model has been used to describe the mode of charge transport when an electric field is applied to the system. It has successfully shown that increasing the charge trap depths and densities increases the breakdown strength of a composite. However, this model makes a number of assumptions,[228,229] where it treats the energy barriers for trapping and detrapping for electrons and holes as being of the same energy.[230,231] Macroscopically, the model fails to take into

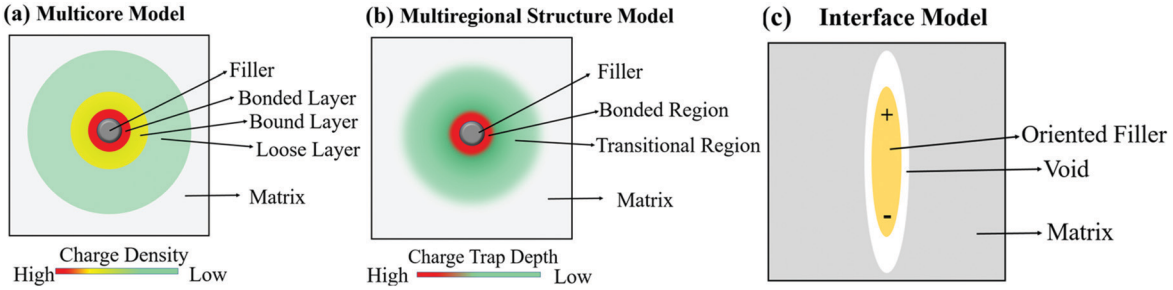

Fig. 21 Schematic visualising the difference in how the (a) multi-core model, (b) multi-regional structure model and (c) interface model treat the interface between filler and matrix.

account ion transport or Maxwell–Wagner–Sillars polarization and its impact of relative permittivity or electrical conductivity. In addition, an induced dipole moment model has been used to describe the polymer–filler interface. The approach assumes that polar groups are permanent dipoles and that the nanoparticles have induced dipoles under an electric field.[232] The fillers result in the formation of deep charge traps, which vary based on the relative permittivity, shape and size of the filler. The traps led to a reduction in space charge, when the particle size was below 200 nm and when its relative permittivity increased. The interfacial models have been discussed, experimental efforts to understand polarization are now described, along with polarization mechanisms.

4.2 Polarization mechanism

There are four principle types of polarization, which include electronic polarization, interfacial polarization, dipolar polarization and ionic polarization. Electronic polarization relates to when an atom or molecule is located in electric field and its electrons are displaced slightly toward the positive direction of the electric field and form impermanent polarizations. Electronic polarization is present in all materials and persists over the entire frequency range, which can contribute to the permittivity, while it does not contribute to conductivity or dielectric loss in most dielectrics. Ionic polarization is the result of the displacement of cations and anions in an electric field, which is the main contributor of permittivity to the dielectrics and present as predominant polarization in inorganic crystals, glasses and ceramics. Dipolar polarization is a result of dipole orientation in the direction of the electric field and which occurs in polar dielectrics, such as polar polymers and ceramics. Interfacial polarization was recognized before 1900, and Maxwell–Wagner–Sillars (MWS) is a well-known mechanism for interfacial polarization. Interfacial polarization is observed at relatively low frequencies and formed in dielectric composites with two or more compositions, which associate with permittivity, dielectric loss and conductivity.[233–237] Usually, the formation of interfacial polarization will lead to the enhancement of relative permittivity in a nanocomposite. However, under the application of a high electric field, space charges are blocked at the interface and trapped due to the long relaxation process of interfacial polarization in the discharge cycle, which leads to low energy storage efficiency as a result of an inefficient energy discharge. The increased local electric field may also create AC conduction and result in increased dielectric loss and decreased breakdown strength. Therefore, numerous approaches have been utilized to achieve dielectric enhancement with suppressed dielectric loss and improved breakdown strength in nanocomposites.

To study the polarization mechanism in detail, Niu *et al.*[192] modified $BaTiO_3$ with different aromatic modifiers in a PVDF matrix. The range of modifiers acted to vary the number of carboxylic acid groups bound to the surface of $BaTiO_3$ and the number of fluorine atoms attached to the benzene ring. In all cases, the chemically modified $BaTiO_3$ showed a lower relative permittivity compared to pure $BaTiO_3$, which was attributed to polar groups promoting a stronger dipole interaction with the PVDF matrix, thus reducing the interfacial polarization and increasing the dispersion. In addition, the modifiers on the $BaTiO_3$ surface acted as charge traps which reduced space charge polarization and minimized the conduction pathways in the polymer film. A high breakdown strength, high energy displacement, high energy density and high efficiency was achieved when the modifier was from a single carboxylic acid linkage to $BaTiO_3$ with four fluorines attached to the ring. This was attributed to the ability of the aromatic ring to orientate under an electric field, while the rings with two carboxylic acid linkages were severely restricted from any movement.[238] Dual modification of $BaTiO_3$ with partial modification with OH groups and a titanate coupler (D-h-$BaTiO_3$) is shown in Fig. 22a.[239] The hydroxyl groups improved the compatibility of the nanoparticles with PVDF and resulted in amorphous regions whilst the oligomeric chains on DN-101 re-introduced a crystalline structure to the PVDF matrix. Compared with pure PVDF, the increased relative permittivity and reduced dielectric loss at low frequencies was achieved for D-h-$BaTiO_3$ in PVDF, which was attributed to the OH groups on $BaTiO_3$ acting as charge traps to minimize charge conduction pathways in the film.[240] The discharged energy density and stored energy density were enhanced upon inclusion of the filler into the PVDF film. The OH groups act as free electron traps for the $BaTiO_3$ and thus lead to an increased negative charge build-up on the surface of the nanoparticle. This increased the interfacial polarization between the nanoparticles and PVDF matrix, thereby increasing the overall polarization in the composite, as shown in Fig. 22b.

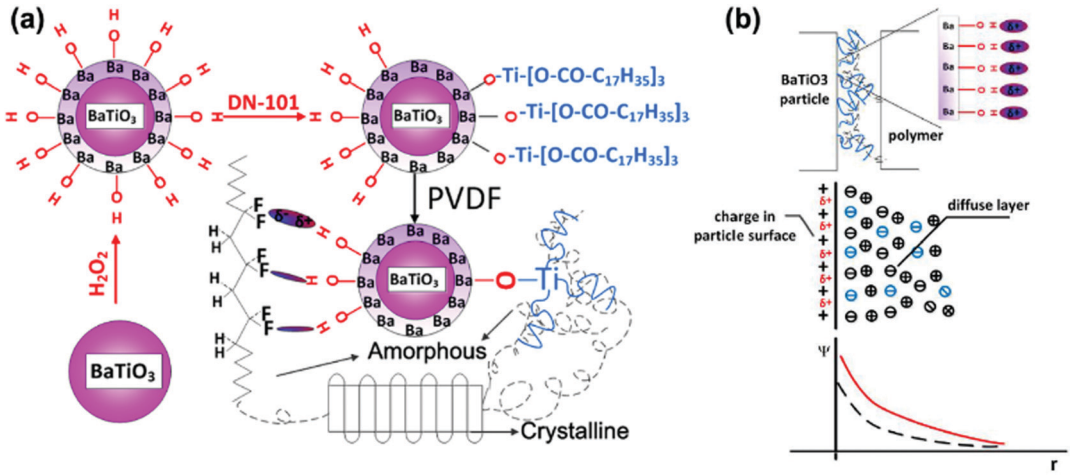

Fig. 22 (a) Diagrams of the modification of $BaTiO_3$ particles and interaction in D-h-$BaTiO_3$/PVDF. (b) Charge distribution in D-h-$BaTiO_3$/PVDF interface. Reprinted with permission from ref. 239. Copyright (2014) American Chemical Society.

Liu *et al.*[92] studied the correlation between the interfacial polarization and discharged energy density in dielectric nanocomposites that consisted of core–shell structured $BaTiO_3$@SiO_2 nanofibers in a PVDF polymer matrix. The results showed that coating SiO_2 layers on the surface of $BaTiO_3$ nanofibers can act to block the movement of charge carriers through the nanocomposite by providing a shielding role on the charge-rich inter layer, which resulted in weak Maxwell–Wagner–Sillars interfacial polarization and thus reduced the energy loss and improved the energy discharged density of the nanocomposite. As shown in Fig. 23, without any interfacial polarization, there is no significant gain in the charge and discharge process and all stored charges can be completely released during the discharge process. With a high interfacial polarization, the polarization charges are stored in the charging process and trapped in the discharge process, resulting in a lower discharge and lower energy storage efficiency.

Rahimabady *et al.*[87] obtained a higher relative permittivity in PVDF–HFP based nanocomposites with TiO_2 coated $BaTiO_3$ nanoparticles compared to unmodified $BaTiO_3$. The enhancement was attributed to the build-up of interfacial polarization between the $BaTiO_3$/TiO_2 interface and the TiO_2/PVDF–HFP interface as well as an increase in the charge trapping by the TiO_2 shell. More specifically, Rahimabady *et al.* indicated that the increase in interfacial polarization was the result of the high density of oxygen vacancies that act as n-type semiconductors on TiO_2, resulting in a Fermi level difference of 0.5 eV between TiO_2 and $BaTiO_3$ so that the TiO_2 exhibits positive space charge and BaTiO3 exhibits negative space charge. PVDF–HFP is electronegative and therefore formed a negatively charged layer at the interface.

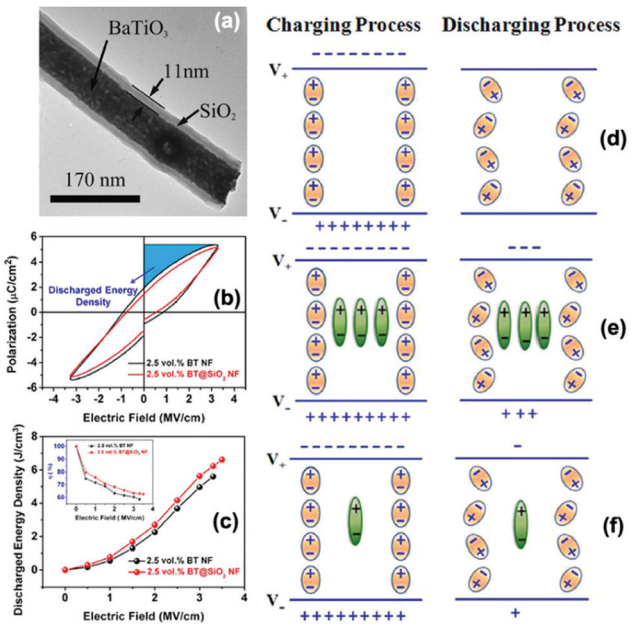

Fig. 23 (a) TEM of the morphology of core–shell structured $BaTiO_3$@SiO_2 nanofibers. (b and c) Polarisation–electric field loops, discharged energy density and energy storage efficiency of nanocomposites with $BaTiO_3$ nanofibers and $BaTiO_3$@SiO_2 nanofibers. Schematic of charge and discharge mechanism under an electric field across a nanocomposite: (d) without interfacial polarization, (e) with high interfacial polarization, and (f) with low interfacial polarization. Interfacial polarization charges are represented by green dipoles. Charges completely released in discharge process are represented by orange dipoles. Reprinted from ref. 92 with permission of AIP Publishing.

TiO_2 with an organic dopamine core–shell that was decorated with silver nanoparticles (nAg) have been introduced into a nitrile-butadiene-rubber (NBR) matrix by Yang *et al.* with a view to introducing a Coulomb blockade effect from enhanced quantum confinement of the silver nanoparticles, as shown in Fig. 24.[241] The mechanism of the Coulomb blockade effect is a result of the nanoparticles having a higher energy barrier to allow tunneling electrons to pass compared to micro-scale particles. This higher energy barrier typically prevents a second electron from tunneling, in this case from TiO_2,[241] which prevents space charge accumulation, as free electrons from TiO_2 are quantum confined to the filler. The Coulomb blockade effect has been used to reduce the leakage current and increase the breakdown strength of composites.[242] In this case, the nAg

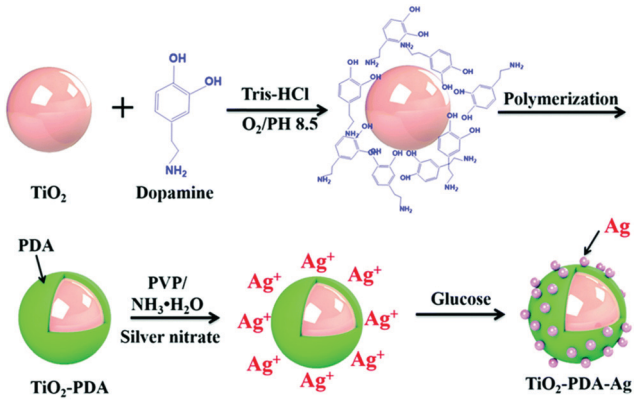

Fig. 24 Schematic of dopamine coated TiO_2 with silver nanoparticles to introduce the Coulomb blockade effect. Reproduced from ref. 241 with permission from the Royal Society of Chemistry.

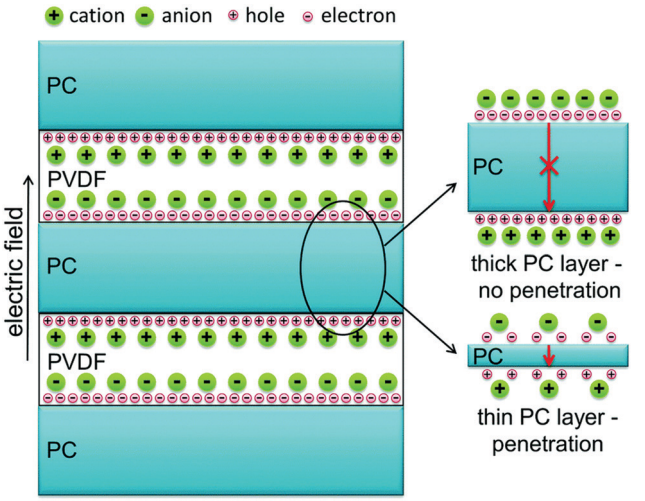

Fig. 25 Schematic of interfacial polarization of space charges in polycarbonate (PC)/PVDF multi-layer films under an applied electric field. A thick PC layer prevents space charges from penetrating through the film to increase interfacial polarization, whereas a thin PC layer allows space charges to penetrate. Reproduced from ref. 246 with permission from the Royal Society of Chemistry.

reduced the space charge polarization and prevented electron migration[243] since the nAg introduced a barrier that required more energy than the thermal motion of an electron to overcome and thus prevented a second electron passing through. The nAg particles can be thought of as a "Coulomb island". In the work, ten parts per hundred parts of rubber of modified nAg–dopamine–TiO_2 filler was added. However, this resulted in degradation of the dielectric properties compared to the addition of dopamine–TiO_2 into NBR, with a lower relative permittivity, higher dielectric loss tangent and lower breakdown strength. The explanation was that the decoration of the nAg particles on the surface of the filler increased interfacial polarization, leading to the introduction of ions, which could lead to breakdown of the composite at a lower electric field.[244] In addition, the nAg particles reduced the space charge through the Coulomb blockade effect.[245]

In the case of multi-layer structured composites, the interfacial polarization at the interface between layers plays an important role in the electric and dielectric properties of nanocomposites. For multi-layer structured composites with PVDF-based ferroelectric polymer layers, its enhanced electric displacement often results from the C–F bonds and the spontaneous alignment of dipoles in the crystalline phases of its PVDF based ferroelectric polymer layers (with a low relative permittivity) at a largely enhanced local electric field. Importantly, in addition to the polarization from the PVDF ferroelectric layer, interfacial polarization can also build up at the interface of multi-layer structured composites in response to the application of an electric field and plays an important role in the electric and dielectric properties of composites. Chen *et al.*[246] developed a multi-layer film comprised of PVDF and polycarbonate (PC) with either 32 layers or 256 layers, but maintained the same total polymer thickness by reducing the thickness of the individual polymer layers; a schematic is shown in Fig. 25. The breakdown strength of the 32-layer multi-layer film was greater than the multi-layer film with 256 layers. This was attributed to the inability of the space charges to penetrate the PC, resulting in greater interfacial polarization. However, in the 256-layer multi-layer film, space charges could penetrate more easily leading to a lower interfacial polarization and a lower breakdown strength and higher DC conductivity.

Xie *et al.*[247] developed a linear/ferroelectric bilayer-heterostructured polymer nanocomposite with an ultra-high discharged energy which exhibited an enhanced breakdown strength and a large difference between the maximum dielectric displacement and remnant polarization (D_{max}–P_r). The enhancement was attributed to the interfacial barrier and the interfacial polarization effect at the interface of two layers. A linear PI was employed as the bottom insulating layer to provide high breakdown strength, while ferroelectric P(VDF–CTFE) with dispersed $BaTiO_3$ nanoparticles was used as the top layer to provide a high relative permittivity, as shown in Fig. 26a and b. In this structure, both the PI single or a $BaTiO_3$/P(VDF–CTFE) single

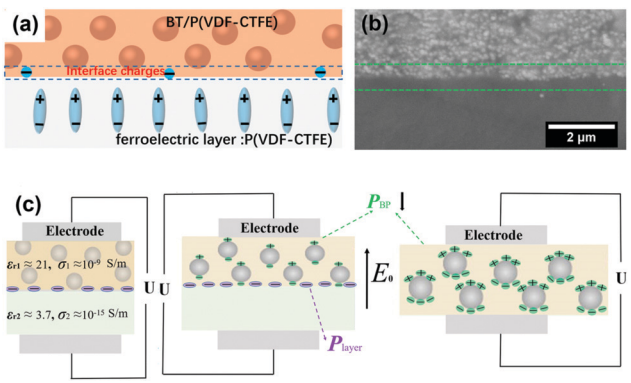

Fig. 26 (a) Schematic and (b) cross-section SEM image of bilayer heterostructure $BaTiO_3$/P(VDF–CTFE)–polyimide (PI) nanocomposite. (c) Schematic of two-layer dielectric considered in the Maxwell–Wagner–Sillars model for interfacial polarization and the poling mechanism of the bilayer heterostructure $BaTiO_3$/P(VDF–CTFE)–PI. Reprinted from ref. 247, Copyright (2018), with permission from Elsevier.

layer exhibited a lower breakdown strength compared with the bilayer composite. The polarization in the $BaTiO_3$/P(VDF–CTFE) layer (P_{BP}, polarization associated with an electric field, such as dipole orientation polarization, interfacial polarization between the filler and the polymer matrix) was weakened with a decrease of the local electric field, as shown in Fig. 26c. Thus, although the overall applied electric field of the $BaTiO_3$/P(VDF–CTFE)–PI nanocomposite was improved, the contribution of the $BaTiO_3$/P(VDF–CTFE) layer to the overall polarization was limited. The contribution to the overall polarization enhancement was attributed to the interface of the bilayer films. Due to the large contrast in relative permittivity and conductivity between the linear and ferroelectric layer, a higher Maxwell–Wagner–Sillars interfacial polarization builds up at the PI/PVDF interfaces in response to the application of an electric field. Hence, space charges that include free electrons, ions in the $BaTiO_3$/P(VDF–CTFE) layer and bound charges near the PI layer result in an additional enhancement of polarization at $BaTiO_3$/P(VDF–CTFE)/PI interface, as shown in Fig. 26c.

In addition to experimental methods, computational methods have also been employed to understand the factors that affect the performance of dielectric nanocomposites. In polymer nanocomposites, it is a challenge to predict the relative permittivity and electric field distribution due to the large numbers of factors that should be considered in any model. Finite element simulation is an effective theoretical approach to examine the interface charge density distribution and spatial potential distribution in nanocomposites.[248,249] The method is based on microstructure-specific space discretization, whereby discrete meshes are used that coincide with the interfaces of the multi-phase microstructure of a nanocomposite. However, for the range of microstructures to be considered, different meshes are needed, and the numerical complexity significantly increases with increasing complexity of the composite structure. To overcome this challenge, phase field simulation has been developed,[250] which solves electrostatic equations in terms of a polarization vector field in reciprocal space using a fast Fourier transform technique and a parallel computing algorithm.[251] For this method, the interphase boundary conditions are automatically satisfied without explicitly tracking the inter-phase interfaces when calculating the effective permittivity, local electric field distribution, and charge density in the nanocomposite. In Sections 4.3 and 4.4, respectively, we discuss the use of finite element simulation and phase field simulation in nanocomposites to assess their properties.

4.3 Finite element simulation

Shen *et al.* utilized the finite-element method to investigate the space charge effects on the dielectric response of polymer nanocomposites.[252] In this model system, two kinds of polymer nanocomposites with randomly distributed and aggregated $SrTiO_3$ nanoparticle fillers in the polyethylene matrix were developed, as shown in Fig. 27a and b. The equilibrium distributions of space charge in these two polymer composites are respectively shown in Fig. 27c and d. Fig. 27e and f provide the space charge distribution along the A–A and B–B cross sections. It was found that the positively charged ions concentrate at the interfaces and gradually reduced into the bulk matrix if the nanoparticles in the polymer composite were negatively charged. The results were consistent with the electric double layer model, as described in Section 4.1. Moreover, the high density of charges can lead to high local electrical conductivity. Space charge has a significant contribution to the increase of relative permittivity and to the dielectric loss, especially when the nanofillers aggregate and the ion concentration in the bulk polymer is high. Preventing the nanoparticles

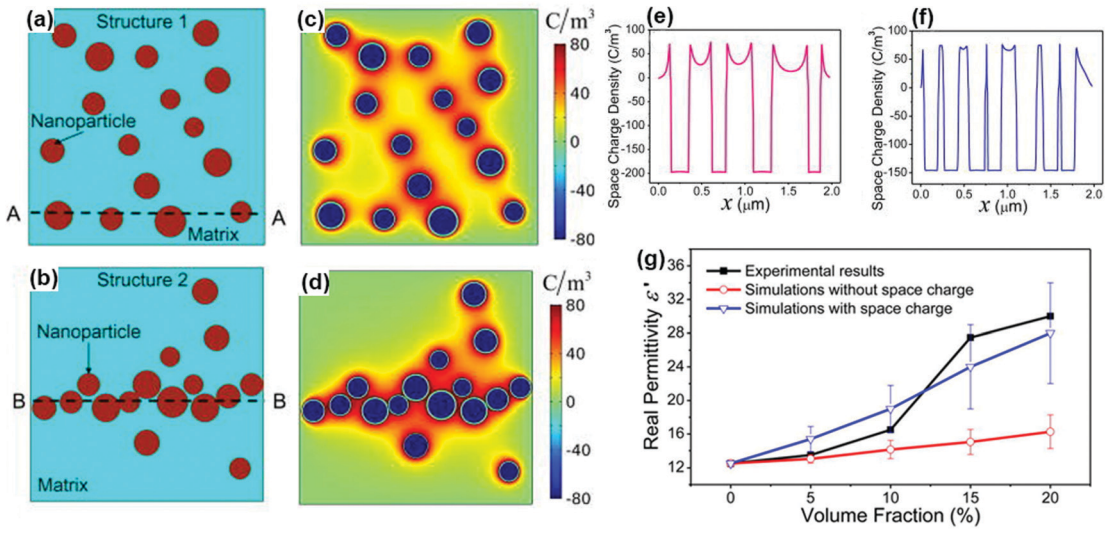

Fig. 27 (a and b) Schematics of polymer nanocomposites with 12% volume fraction of randomly distributed and aggregated $SrTiO_3$ nanoparticles with radii ranging from 70 to 120 nm. (c and d) Corresponding equilibrium distributions of space charge and (e and f) cross section profiles along A–A and B–B. (g) Effects of the nanoparticle volume fraction on the relative permittivity of P(VDF–HFP)/TiO_2 nanocomposites predicted from the model and by experiment. Reprinted from ref. 252 with permission of AIP Publishing.

from aggregating is beneficial to the increase of relative permittivity without increasing the loss significantly. Using the present model, Fig. 27g shows the calculated relative permittivity as a function of the volume fraction of the nanoparticle filler for the P(VDF–HFP)/TiO_2 polymer composite. It was noted that the relative permittivity exhibited a slow increase with increasing filler volume fraction without consideration of the space-charge contribution. However, after taking space-charge effects into account, the relative permittivity increased to a large extent, which was in better agreement with the experimental results. The computational results demonstrated that the dielectric response is largely determined by space charges accumulating at interfaces.

Roscow *et al.*[253] used finite element modelling to examine the electric field distribution and dielectric properties of composites containing conductive fillers at a range of aspect ratios and orientations. Electric field maps for an aspect ratio of eight are shown in Fig. 28a where they investigated the influence of filler angle with respect to applied electric field and the aspect ratio of a filler on the normalized breakdown strength (E_b*), ε_r and energy density (eqn (1); $\varepsilon_r.(E_b^*)^2$). The data is shown in Fig. 28b–d, respectively, where the data was normalized with respect to the filler-free matrix which is indicated by the dotted line. Fig. 28b shows that high aspect ratio inclusions aligned perpendicular to the applied field provided the highest breakdown strength, since this orientation led to the lowest electric field concentrations, as seen in Fig. 28a. The lowest breakdown strength occurred when the high aspect ratio particles were parallel to the applied electric field. The model indicated that for the wide range of filler orientations and aspect ratios, the breakdown strength is always lower than that the filler-free matrix in which the field is homogenous at all points in the matrix. An opposing trend was observed for the relative permittivity since electric field concentrations benefit relative permittivity, but are detrimental to dielectric strength. Since energy density depends on the square of the breakdown strength, the inclusion of conductive fillers of any orientation or aspect ratio reduces the energy storage capabilities of the composite compared to the matrix material, as shown in Fig. 28d. However, the model does not include ion transport, in particular at interfaces, and the impact of filler on the polymer materials, but nevertheless explains the challenge of using filler materials to increase relative permittivity, while not degrading the breakdown strength. Fillers with high aspect ratio were also modeled using a finite element approach in Luo *et al.*[254]

Finite element simulations were also successfully used to examine the electric field distribution and dielectric properties of nanocomposites with a core–shell or hierarchical structured fillers. Pan and Zhai *et al.* used finite element simulations to analyse the electric field and electric current density distribution in the PVDF-based nanocomposites filled with dopamine coated $BaTiO_3$ nanoparticles and dopamine coated $BaTiO_3@Al_2O_3$ nanofibers.[143] For the $BaTiO_3@Al_2O_3$ nanofibers, $BaTiO_3$ nanoparticles were homogeneously embedded in the Al_2O_3 nanofibers, as shown in Fig. 29. In both the experiment method and simulation, the majority of nanofillers were located along the in-plane-oriented direction of the polymer matrix. The experimental results revealed that the dopamine coated $BaTiO_3@Al_2O_3$ nanofibers improved the dielectric performance and breakdown strength of the nanocomposites, leading

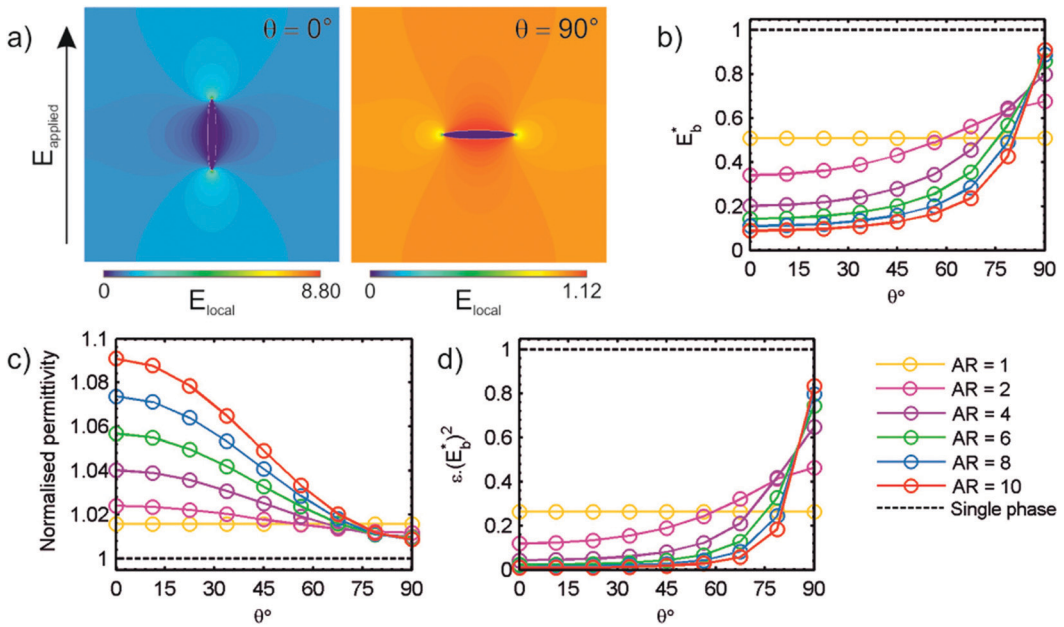

Fig. 28 (a) Contour maps of electric field distribution for an individual conductive inclusion with high aspect ratio (AR = 8), and angle with respect to applied field (φ = 0° (left) and 90° (right)) contained within a dielectric matrix; and variation of (b) effective breakdown strength, E_b^2, (c) relative permittivity and (d) energy density, $\varepsilon_r.(E_{dielectric})^2$ with changing angle and aspect ratio of single inclusion. Reprinted with permission from ref. 253. Copyright (2017) American Chemical Society.

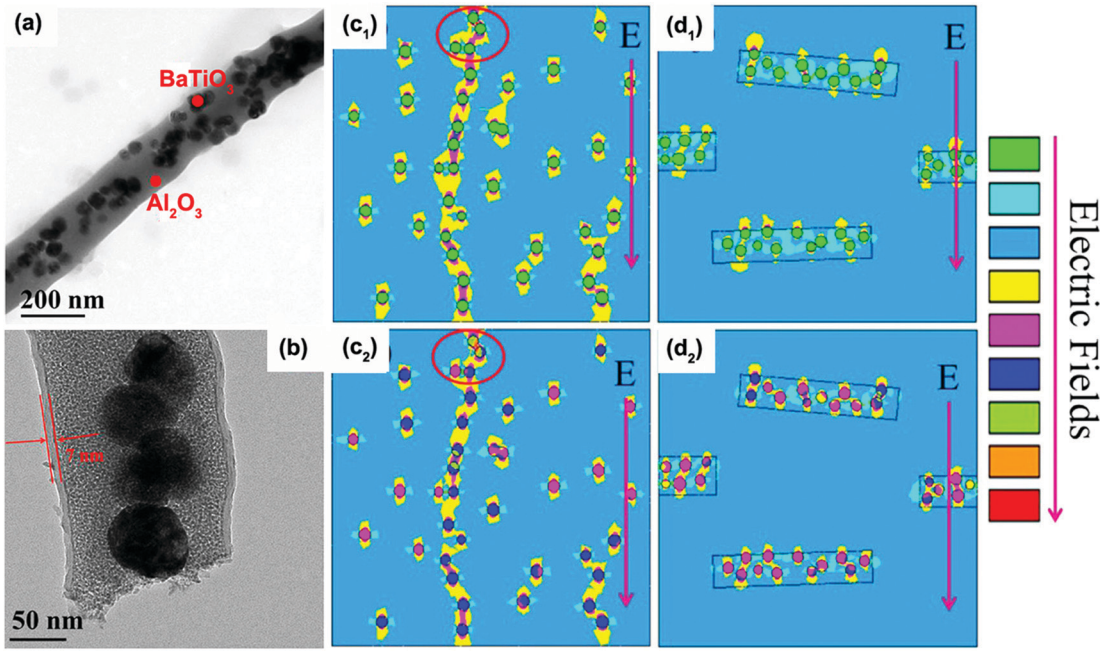

Fig. 29 TEM images of (a) $BaTiO_3$@Al_2O_3 nanofiber and (b) dopamine coated $BaTiO_3$@Al_2O_3 nanofiber. Distributions of electric field and electric current density simulated for the nanocomposites with dopamine coated $BaTiO_3$ nanoparticles (c_1 and c_2), and the nanocomposites with dopamine coated $BaTiO_3$@Al_2O_3 nanofibers (d_1 and d_2). Reprinted with permission from ref. 143. Copyright (2017) American Chemical Society.

to an enhanced energy density. In terms of the simulation results, it was found that the local electric field strength in the nanocomposites with dopamine coated $BaTiO_3$ nanoparticles was significantly higher than the nanocomposites with dopamine coated $BaTiO_3$@Al_2O_3 nanofibers located between the adjacent fillers, as indicated by the intensified pink region in Fig. 29. As a result of the larger permittivity contrast between the matrix and nanofillers, the local electric field strength is traceable to charge agglomeration at the interface. In addition, the nanocomposites with dopamine coated $BaTiO_3$@Al_2O_3 nanofibers also exhibited a significantly lower local electric current density than the nanocomposites with dopamine coated $BaTiO_3$ nanoparticles. It is known that the difference of the electric current density is attributed to the contrast of local electric resistivity between the matrix and nanofillers. The Al_2O_3 insulated layer was considered to be effective in restricting charge carrier migration in the space between the matrix and nanofillers. Moreover, in the nanocomposites with dopamine coated $BaTiO_3$ nanoparticles, the local electric field or electric current density at adjacent nanoparticles tended to form a channel along the electric field direction, exhibited by the intensified yellow region in Fig. 29, which can lead to a greater probability of breakdown. As a result, the dopamine coated $BaTiO_3$@Al_2O_3 nanofibers were more attractive in energy storage applications.

Sandwich/multi-layer structured nanocomposites have been widely studied for the high performance they can achieve, such as improved breakdown strength and high energy density. The formation of a weak electric field and incomplete breakdown are the key factors for achieving high performance. Wang *et al.*[167] used finite element simulations to prove that the improvement in energy density of sandwich-structured $BaTiO_3$/PVDF nanocomposites was attributed to the favourable electric field redistribution. Electric tree growth theory was used to explore the electric breakdown mechanism in sandwich structured nanocomposites. As can be seen in Fig. 30a, the spacing of adjacent equi-potential lines were used to show the heterogeneous distribution of electric field.[255] It is clear that the $BaTiO_3$/PVDF nanocomposite layer can endure higher electric field when it is formed as a sandwich structure, compared to a monolayer nanocomposite. In addition, the electric field of the $BaTiO_3$/PVDF layer with 1 vol% $BaTiO_3$ in the sandwich-structured nanocomposites is smaller than that on the single-layer composite with 20 vol% $BaTiO_3$. The weak internal electric field is formed to block the development of electrical trees in the interface of the adjacent layers in the sandwich $BaTiO_3$/PVDF nanocomposites, which was considered to be the main reason for the enhanced breakdown strength; see Fig. 30c. After introducing $BaTiO_3$ nanoparticles into the PVDF matrix, the electric field is increased in the regions above and below the $BaTiO_3$ nanoparticles, while it weakens the field on the left and right side of the ceramic fillers (perpendicular to applied field) and the authors indicate that the incomplete breakdown theory can explain the simulation results. It was thought that an incomplete breakdown path is formed only in the high electric field region when the local electric field is higher than its intrinsic breakdown strength, and the path will not grow through the whole composite film to achieve complete breakdown.[256] The functional region of low electric field can only be formed when the $BaTiO_3$ loading in the middle layer was at an optimal value, which was 20 vol% in this work. If the $BaTiO_3$ content is reduced, the distance between adjacent $BaTiO_3$ nanoparticles will be too far to form a low electric field region.

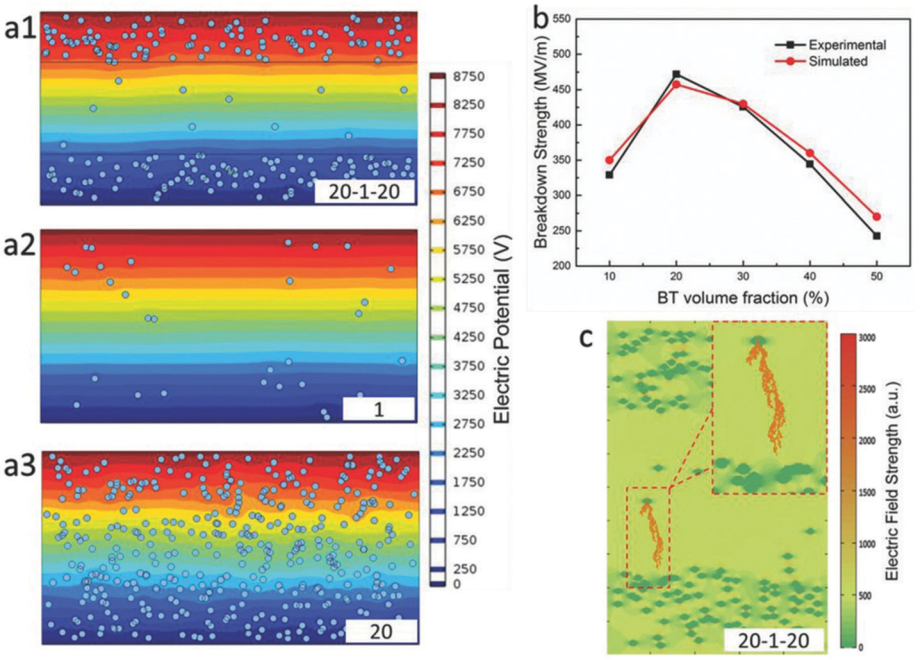

Fig. 30 Simulation of electric field in (a1) sandwich structured nanocomposite with 20 vol% $BaTiO_3$ nanoparticles in the outer layers and 1 vol% $BaTiO_3$ nanoparticles in the central layer, (a2) single PVDF nanocomposite with 1 vol% $BaTiO_3$ nanoparticles, (a3) single PVDF nanocomposite with 20 vol% $BaTiO_3$ nanoparticles, (b) comparison of the breakdown strength for experimental data and simulated results, (c) simulation of incomplete breakdown process in the sandwich structured nanocomposite. With permission from ref. 167. Copyright 2015, John Wiley and Sons.

4.4 Phase field simulation

The electrostatic breakdown propagation of dielectric materials is complex, however, the use of a phase-field model is a good approach to understand the breakdown behaviour arising from electrostatic stimuli.[257] For the phase field model, it is considered that the complete breakdown path of the composite is similar to the process of crack propagation, although a clear difference is that it incorporates electric energy, gradient energy, and phase separation energy. The calculation process was described in detail by Shen groups.[258] Through a continuum phase-field model, the microstructural effects on the effective relative permittivity, breakdown strength, and the energy density of polymer nanocomposites can be systematically studied, including the shape, the orientation and volume fraction of the nanofiller. Taking the PVDF–$BaTiO_3$ nanocomposite as an example, they performed a 2D simulation to predict the breakdown phase evolution under applied electric fields and the simulated results. The polymer nanofiber composites exhibited a shorter breakdown path than the nanoparticle based composites, suggesting that the breakdown phase tended to penetrate through the nanofiber rather than around the nanofiber. In addition, the electric field distribution indicated that the electric field concentrates at the two shoulders along the electric field direction for the polymer nanoparticle composite, which makes it easy to form a breakdown path. In comparison, the electric field concentrates at the vertices of the nanofibers for the polymer nanofiber composites. Therefore, the nanofiber composite exhibited a higher breakdown strength compared with the nanoparticle based composite, proving that phase-field model results coincided with the experimental results; this is also in agreement with observations in Fig. 28.

In subsequent work, the breakdown phase evolution of polymer based 3D nanocomposites with 10 vol% of nanofiller was examined by high throughput computation; see Fig. 31a. The structures examined included vertical nanofibers (S1), vertical nanosheets (S2), random nanoparticles (S3), parallel nanofibers (S4), parallel nanosheets (S5) and ellipsoidal nanoparticles (S6). In the simulation, the aspect ratio of the nanofiber was 1 : 20 and the length scale of the nanosheet was 1 : 6 : 6. The growth behaviour of the breakdown phase in these nanocomposites under applied electric fields along the *z*-direction is shown in Fig. 31b. The breakdown strength of nanocomposites were 230, 151, 195, 216, 223 and 310 kV mm^{-1} respectively from S0 to S5, as shown in Fig. 31c, revealing that the nanocomposites with vertical nanofibers exhibited the lowest breakdown strength, while the nanocomposites with parallel aligned nanosheets showed the highest breakdown strength, as highlighted also in Fig. 28. Fig. 31d defines the microstructure dataset for the high throughput computation by assigning different length ratios of the nanofillers. Based on the microstructure dataset, the breakdown strength, the effective relative permittivity, and the energy density were calculated by phase-field modelling, as shown in Fig. 31e–g. As the nanofiller changes from S1 to S5, the breakdown strength of nanocomposites gradually increases from 0.56 to 1.35 times that of polymer matrix breakdown strength while the effective

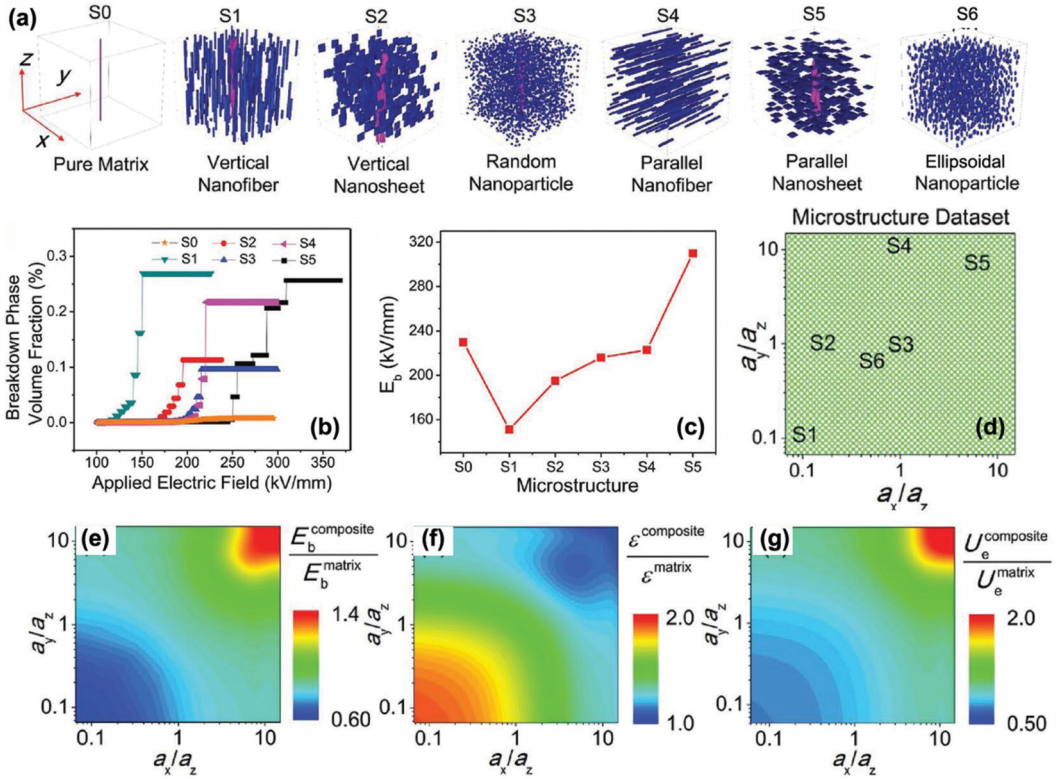

Fig. 31 (a) Simulations of nanocomposites with various 3D-microstructures and corresponding breakdown phase morphology. (b) Evolution of breakdown phase volume fraction with electric field and (c) extracted breakdown strengths. (d) Definition of the microstructure dataset. The datasets of (e) the breakdown strength, (f) the effective relative permittivity, and (g) the energy density from the high throughput calculation. With permission from ref. 257. Copyright 2017, John Wiley and Sons.

relative permittivity decreases from 2.24 to 1.08 times that of the polymer matrix relative permittivity. The nanocomposites with parallel nanosheets possess the highest energy density, which is about 1.97 times that of the polymer matrix.

Further, according to the high throughput calculation results, the Shen group searched for dielectric materials with a higher energy density by forming polymer nanocomposite with sandwich structures (Section 2.4). For example, a sandwich nanocomposite which was filled with parallel nanosheets at the upper and lower layers, and with vertical nanofibers at the middle layer, was designed and the energy density for this designed microstructure is 2.42 times higher than the polymer matrix.

Phase field simulation was also employed to study the nanocomposites with core–shell structured nanofillers for energy storage applications. Wang *et al.* investigated the electric field distribution in nanocomposites filled with high-permittivity core–shell structured nanofillers, as shown in Fig. 32.[251] In this simulation approach, a graded permittivity distribution was achieved by setting the dielectric susceptibility of core (χ_c), shell (χ_s), and matrix (χ_m) from a high level to a low level. The core–shell structured nanofillers were optimized by regulating the shell thickness (t) and χ_s for a given core size (r), and dielectric susceptibilities of χ_c and χ_m. Firstly, the electric field distributions in nanocomposites were simulated for nanofillers with and without a core–shell structure, as shown in Fig. 32c and d respectively. The core–shell structure was shown to be able to effectively reduce both the local electric field concentration and distortion at the interface region. Then, the effects of χ_s and shell thickness (t) were further investigated, which showed that the optimal χ_s was confirmed as $\chi_s : \chi_m : \chi_c = 1.81 : 1 : 100$, and the χ_c had little effect on the optimal χ_s, as shown in Fig. 32e. In addition, a thicker shell was beneficial to reduce the electric field concentration, as shown in Fig. 32f. The results theoretically confirmed that constructing a dielectric gradient in nanocomposites by core–shell structure is an effective approach to mitigate the field concentration and improve the breakdown strength.

In the case of sandwich/multi-layer structured nanocomposites, phase field simulation has also been used effectively to analyse the spatial distribution of electric field in the nanocomposites, Zeng and Nan *et al.* prepared a series of single-layer and multi-layer structured nanocomposites using P(VDF–HFP) as the matrix and parallel boron nitride nanosheets as the filler.[259] The detailed structures of nanocomposites are shown in Fig. 33a. The parallel boron nitride nanosheets can limit electron tunnelling through the matrix/filler interfaces and suppress the growth of electrical trees during breakdown, as shown in Fig. 33. Here, the main concern was the effect of different multi-layer structures on the electric field distribution in the nanocomposites. The results of phase field simulation, as shown in Fig. 33b, indicated that the 12L

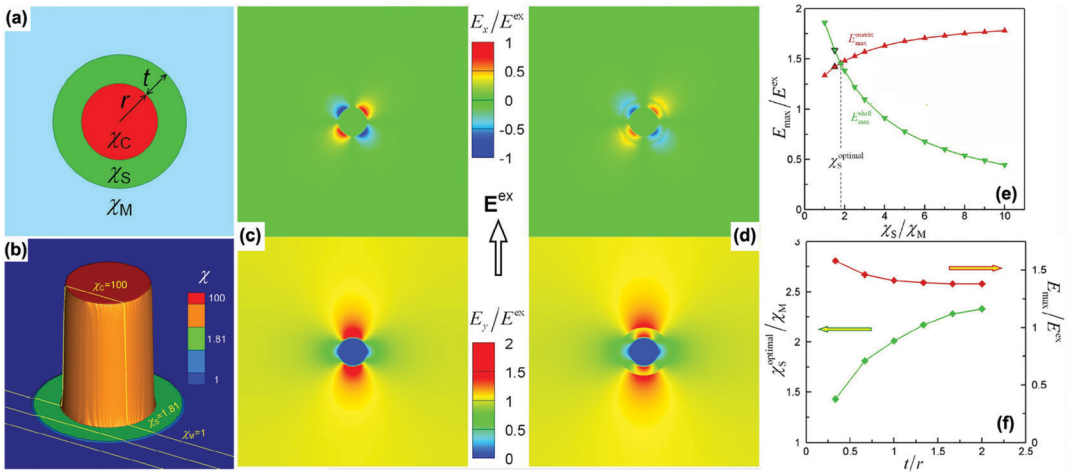

Fig. 32 (a) Schematic of the design variables in nanocomposite with core–shell structured nanofiller embedded in the matrix. (b) Three-dimensional visualization of dielectric susceptibility distribution in nanocomposite, where $\chi_m : \chi_s : \chi_c = 1 : 1.81 : 100$ and $t/r = 2 : 3$. Local electric field concentration in nanocomposite for nanofillers (c) without and (d) with core–shell structure. (e) Effect of χ_s on local electric field concentration in nanocomposite with $\chi_m : \chi_c = 1 : 100$ and $t/r = 2 : 3$. (f) Effects of t on optimal χ_s and maximum local electric field magnitude in nanocomposite with $\chi_m : \chi_c = 1 : 100$. Reprinted from ref. 251 with permission of AIP Publishing.

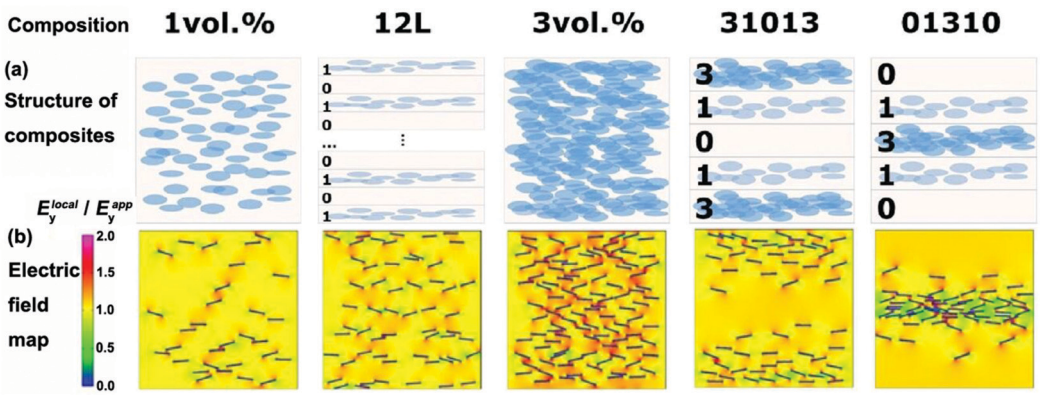

Fig. 33 (a) Composition and structure of nanocomposites with parallel boron nitride nanosheets. (b) Phase-field simulation of electric field distribution in corresponding nanocomposites. Reprinted from ref. 259 with permission of AIP Publishing.

(12 layer) structured nanocomposites exhibited the most homogeneous spatial distribution of electric field compared with other structured nanocomposites, which was beneficial for the suppression of dielectric loss. The multi-layer structured nanocomposites containing a multi-interfacial region can effectively block the growth of electrical trees, and thus improve the breakdown strength and energy density. These results indicate that developing phase-field models and performing high throughput calculations is an important approach to discover polymer nanocomposites with high storage properties and design potential architectures.

5. Strategies for high energy storage application of the composites

As discussed in above sections, interfacial design has been successfully applied to improve the performance of polymer composites. With the aid of some specific focussed examples, this section discusses the strategies to create new materials for high energy storage applications. This includes optimizing the morphologies of the fillers (type and dimensionality), filler orientation and structural design.

5.1 Optimization the morphologies of the ceramic fillers

The present section focuses on the morphology of ceramic fillers and corresponding performance of polymer composites where 0D, 1D and 2D ceramic fillers are taken into account.

In general, 0D ceramic fillers embedded in a polymer matrix were mostly studied and discussed by researchers. Linear dielectric nanoparticles with low relative permittivity and high breakdown strength, such as TiO_2, ZrO_2 and SiO_2, have been used to improve the breakdown strength of corresponding polymer composites. However, to improve the dielectric properties, ferroelectric ceramic nanoparticles, such as PZT, $BaTiO_3$, PMN-PT, and BST, have been intensively studied due to their

high permittivity. Combined with the interfacial design strategies, enhanced dielectric and energy storage properties can be achieved in 0D filler based polymer composites. Recently, Chen *et al.*[107] achieved a significantly improved energy density in a $BaTiO_3$ nanoparticle based polymer composite by accurate interfacial tailoring using a novel rigid-fluoro-polymer. As discussed in Section 3.2, the interfacial thickness can be tailored using rigid liquid crystalline polymers. In this study, RAFT polymerization was used to prepare the core–shell structured $BaTiO_3$@rigid-fluoro-polymer nanoparticles with different shell thicknesses. The dielectric performance and energy storage properties of $BaTiO_3$@rigid-fluoro-polymer/P(VDF–TrFE–CTFE) nanocomposites were investigated in detail. As shown in Fig. 34, the rigid-fluoro-polymer shell effectively improved the compatibility and the shell thickness had significant effects on the performance of nanocomposites. The unmodified $BaTiO_3$/P(VDF–TrFE–CTFE) nanocomposites exhibited higher relative permittivity and lower breakdown strength because of the strong interfacial polarization arising from the presence of voids and aggregation. In contrast, the $BaTiO_3$@rigid-fluoro-polymer/P(VDF–TrFE–CTFE) nanocomposites produced lower relative permittivity resulting from the high dispersion, compatibility and insulating nature of the material. However, with an increase of shell thickness, the breakdown strength of nanocomposites was improved. The highest breakdown strength of 514 kV mm^{-1} and discharged energy density of 16.18 J cm^{-3} were achieved in nanocomposites containing 5 vol% fillers, when the shell thickness was approximately 11 nm.

For 0D ceramic filler based polymer composites, a high volume fraction (> 50 vol%) of nanoparticles is often necessary to achieve high relative permittivity, which is often at the expense of breakdown strength and mechanical flexibility of the composites. As a result, 1D ceramic fillers are found to be more attractive for the preparation of high performance polymer composites.[260–262] 1D fillers achieve percolation more easily, leading to a higher relative permittivity and thermal conductivity. Their lower surface area compared with spherical nanoparticles is also beneficial for preventing filler agglomeration and the large dipole moment of 1D fillers facilitates the dielectric enhancement of polymer composites at a lower loading compared to 0D fillers.[2] Following this strategy, a number of 1D ceramic fillers, such as TiO_2,[260] $BaTiO_3$,[263] PZT,[264] $CaCu_3Ti_4O_{12}$,[265] $0.5Ba(Zr_{0.2}Ti_{0.8})O_3$–$0.5(Ba_{0.7}Ca_{0.3})TiO_3$,[118] $SrTiO_3$ nanofibers,[266] have been used to fabricate high performance nanocomposites. For example, Shen and Nan *et al.* prepared $BaTiO_3$@TiO_2 nanofibers where $BaTiO_3$ nanoparticles were embedded in TiO_2 nanofibers using a modified electrospinning process.[141,207] After dopamine modification, the nanofibers were incorporated into the PVDF and P(VDF–HFP) polymer matrix, respectively. In these systems, in addition to the nanofiber/polymer interfaces, further interfaces between the $BaTiO_3$ and TiO_2 were introduced into the nanocomposites without

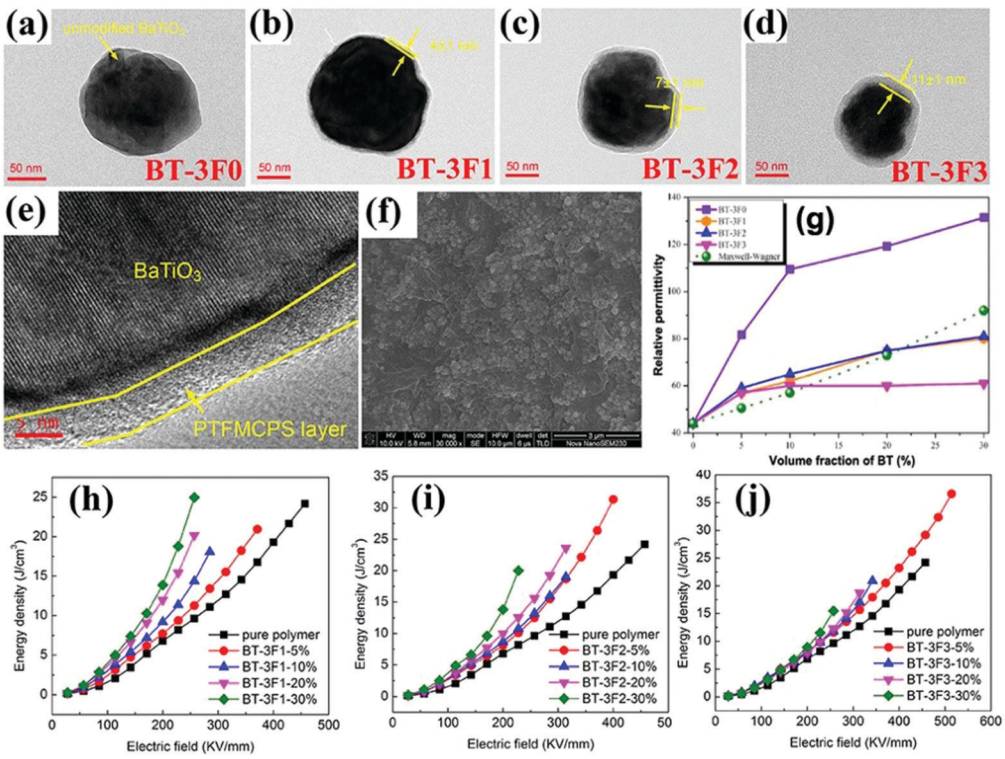

Fig. 34 TEM images of (a) $BaTiO_3$-3F0, (b and e) $BaTiO_3$-3F1, (c) $BaTiO_3$-3F2 and (d) $BaTiO_3$-3F3 nanoparticles. (f) SEM image of the freeze-fractured cross section of nanocomposite with 30 vol% $BaTiO_3$-3F3 nanoparticles. (g) Relative permittivity of nanocomposites with $BaTiO_3$-3F0, $BaTiO_3$-3F1, $BaTiO_3$-3F2 and $BaTiO_3$-3F3 nanoparticles at 1 kHz. (h–j) Energy density of pure polymer and nanocomposites. Reproduced from ref. 107 with permission from the Royal Society of Chemistry.

increasing the total volume fraction of nanofibers. Percolation of the $BaTiO_3/TiO_2$ interfaces gave rise to enhanced interfacial polarization of the $BaTiO_3@TiO_2$, leading to substantially increased relative permittivity of the nanocomposites at a low volume fraction of nanofibers. An improved breakdown strength was also achieved by taking advantages of the large aspect ratio of the nanofibers and dopamine modification, which resulted in an ultrahigh energy density. The dopamine coated $BaTiO_3@TiO_2$/PVDF nanocomposites with 3 vol% nanofibers showed a high breakdown strength of 646 kV mm^{-1} and energy density of $\sim$20 J cm^{-3}. For $BaTiO_3@TiO_2$/P(VDF–HFP) nanocomposites with 3 vol% nanofibers, the breakdown strength was $\sim$797.7 kV mm^{-1} and energy density reached $\sim$31.2 J cm^{-3}. Importantly, a high discharge efficiency of $\sim$78% was also achieved at a high electric field of $\sim$800 kV mm^{-1}.

2D ceramic fillers have also been introduced into the polymer matrix and proven to be effective in improving the energy density due to their ultrahigh specific surface area and superior mechanical flexibility, such as BNNs,[71,267] $(Na_{0.5}Bi_{0.5})_{0.93}Ba_{0.07}$-$TiO_3$,[78] $NaNbO_3$,[172] TiO_2,[268] Bi_2Te_3,[89,90] and $(Ba_{0.6}Sr_{0.4})TiO_3$ plate-like particles.[269] The high aspect ratio 2D fillers also build up efficient conduction barriers that limit charge migration toward the electrodes and hinder the growth of electric trees during breakdown, resulting in an enhanced breakdown strength. As shown in Fig. 35a and b, the BNNs were homogeneously dispersed in the polymer matrix without chemical surface modification, which was attributed to the polar surface of the BNNs with a large specific surface area. A uniform and dense insulating network of BNNs was formed in the polymer matrix, creating a robust scaffold to hinder the onset of electromechanical failure and functioning as an efficient barrier against the leakage current and the space-charge conduction. With the addition of BNNs, the Weibull E_b value was greatly improved and reached the highest value of 610 kV mm^{-1} at a filler content of 12 wt%, which increased by 70% compared with the pristine terpolymer. The value of shape parameter β, which is the Weibull modulus associated with the linear regressive fit of the distribution and indicate the concentration of data distribution,[270] also increased from 8.44 in pristine terpolymer to 15.8. A further increase of BNNs content would degrade performance due to aggregation of BNNs. The suppressed conduction loss also leaded to the reduction in remnant displacement. Moreover, the BNNs were thought to serve as nucleating agents to promote the population density of the nucleation centers for PVDF crystallization and result in increased crystallinity and decreased crystal size of polymer in the nanocomposites, which facilitated the reversal of dipoles within ferroelectric crystalline domains and thereby decreased the hysteresis loss. As a result, a high discharged energy density of 20.3 J cm^{-3} and efficiency of $\sim$80% was achieved in polymer composites with 12 wt% BNNs at 650 kV mm^{-1}. Importantly, the polymer composites exhibited considerably improved thermal conductivity with the addition of BNNs, beneficial for the breakdown stability and lifetime of polymer capacitors. Similarly, Wen and Guo *et al.*[268] obtained thin flexible PVDF based nanocomposites with a high energy density (21.1 J cm^{-3}) by adding 1 wt% 2D monolayer titania. The nanocomposites showed enhanced relative permittivity of $\varepsilon_r \sim 12$ at 1 kHz and a breakdown strength of 650 kV mm^{-1} compared with pure PVDF ($\varepsilon_r \sim 10.5$ at 500 kV mm^{-1}).

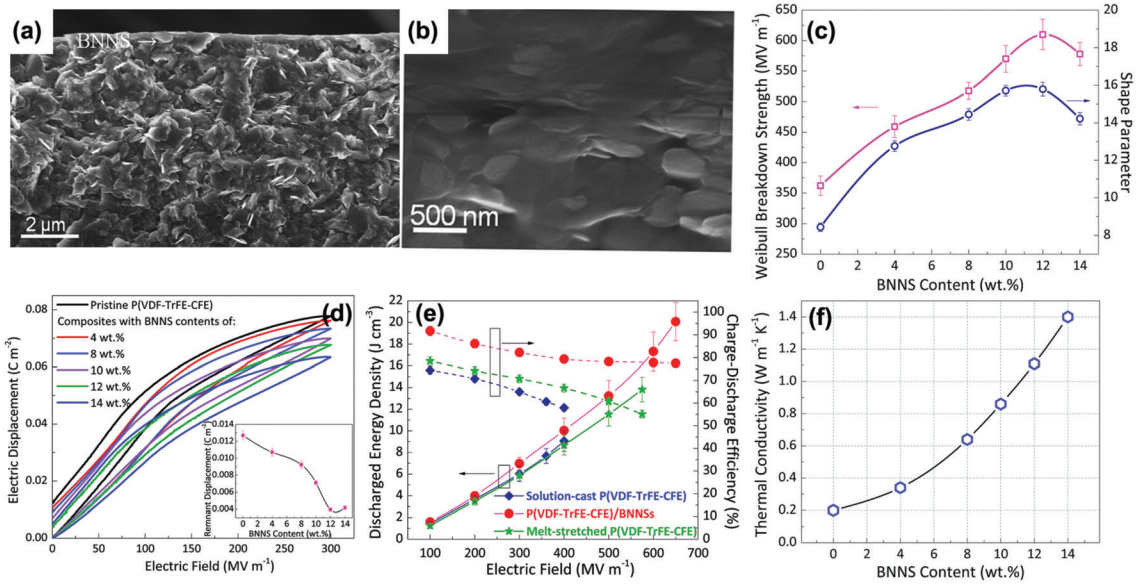

Fig. 35 (a) Large-scale and (b) zoom-in cross-section SEM images of the BNNs/P(VDF–TrFE–CFE) polymer composites with 12 wt% BNNs. (c) Weibull breakdown strength and shape parameter as a function of filler content. (d) Comparison of dielectric displacement-electric field (D–E) loops of pristine P(VDF–TrFE–CFE) and polymer composites with different filler contents at an electric field of 300 kV mm^{-1}. Insert: Remnant displacement as a function of filler content. (e) Comparison of discharged energy density and charge–discharge efficiency of pristine P(VDF–TrFE–CFE) and polymer composites with 12 wt% BNNs at different electric fields. (f) Thermal conductivity of polymer composites with different filler contents. Reproduced from ref. 267 with permission from The Royal Society of Chemistry.

5.2 Orientation of the fillers

In addition to the filler morphology and filler volume fraction, the filler orientation relative to the applied electric field also plays an important role in achieving high performance of polymer composites, as highlighted by the finite element simulation and phase field simulation discussions (Sections 4.3 and 4.4). Tang and Sodano *et al.*[264,271] experimentally investigated the effects of aspect ratio of PZT nanowires and their alignment in the PVDF matrix on the dielectric and energy storage performance of polymer composites. It was demonstrated that polymer composites with nanowires aligned in the axis of the electric field have higher relative permittivity than that with randomly dispersed nanowires while maintaining the breakdown strength. The alignment of the nanowires led to energy densities up to 51.6% greater than polymer composites with random alignment at 20% volume fraction.

It has been accepted that ceramic nanowires aligned perpendicular to the electric field in a polymer matrix benefits the enhancement of breakdown strength, while the ceramic nanowires aligned in the axis of the electric field can induce large electric polarization, as indicated in Fig. 31. Recently, Xie and Jiang *et al.*[272] fabricated P(VDF–CTFE) based nanocomposites with $BaTiO_3$ nanowires aligned perpendicular to the applied electric field $BaTiO_3$ nanowires $\perp E$, denoted as *X*–*Y*-aligned nanocomposites) and aligned in the direction of the applied electric field ($BaTiO_3$ nanowires $\| E$, denoted as *Z*-aligned nanocomposite), as shown in Fig. 36a and c. The nanocomposites under two different orientations with 3 vol% $BaTiO_3$ nanowires showed distinct electrical properties. The relative permittivity and electrical conductivity of the *Z*-aligned nanocomposite are higher than those of the *X*–*Y*-aligned nanocomposite. The difference of relative permittivity due to filler orientation can be explained by the effective medium theory,[273] which indicated that the effective relative permittivity of the *Z*-aligned nanocomposite is larger than that of the *X*–*Y*-aligned nanocomposite. However, the breakdown strength of *X*–*Y*-aligned nanocomposite was higher than that of pristine P(VDF–CTFE), because the $BaTiO_3$ nanowires $\perp E$ led to increased path tortuosity in the electrical treeing process during breakdown; this also has agreement with Modelling of Fig. 31b. However, the *Z*-aligned nanocomposite exhibited a reduced breakdown strength, which was attributed to that of the $BaTiO_3$ nanowires $\| E$ increased the path connection in the electrical treeing process during breakdown; as is also in agreement with the model in Fig. 28. In terms of the *D*–*E* loops, the *Z*-aligned nanocomposite has larger D_{max} and (D_{max}–P_r) values even at a lower electric field. The larger polarization achieved by $BaTiO_3$ nanowires $\| E$ and large relative permittivity were responsible for the enhanced dielectric displacement. As a result, the highest discharged density of 10.8 J cm^{-3} and efficiency of 61.4% were obtained in the *Z*-aligned nanocomposite at a lower electric field of 240 kV mm^{-1}.

The application of a nanowire array was also an effective way to achieve the alignment of nanowires in polymer composites

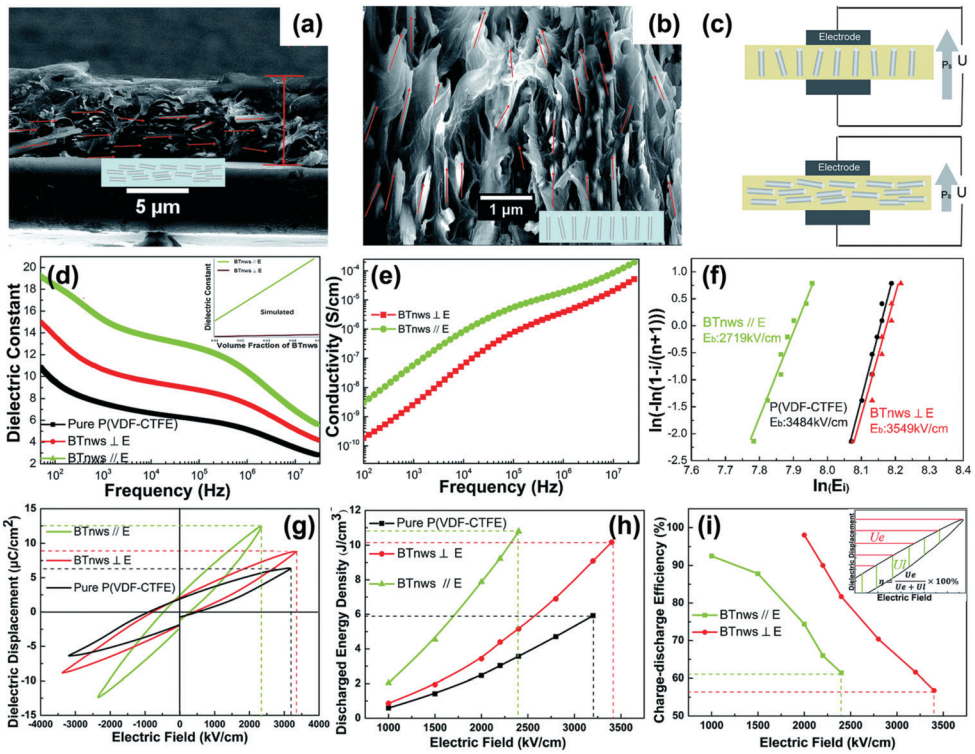

Fig. 36 Cross-sectional SEM images of the (a) *X*–*Y*-aligned and (b) *Z*-aligned nanocomposites. (c) Schematic of the poling mechanism for $BaTiO_3$ nanowires under different orientations. (d) The relative permittivity, (e) electrical conductivity, (f) breakdown strength, (g) *D*–*E* loops, (h) discharge energy density and (i) charge–discharge efficiency for the pure P(VDF–CTFE) and nanocomposites under different orientations. Reproduced from ref. 272 with permission from The Royal Society of Chemistry.

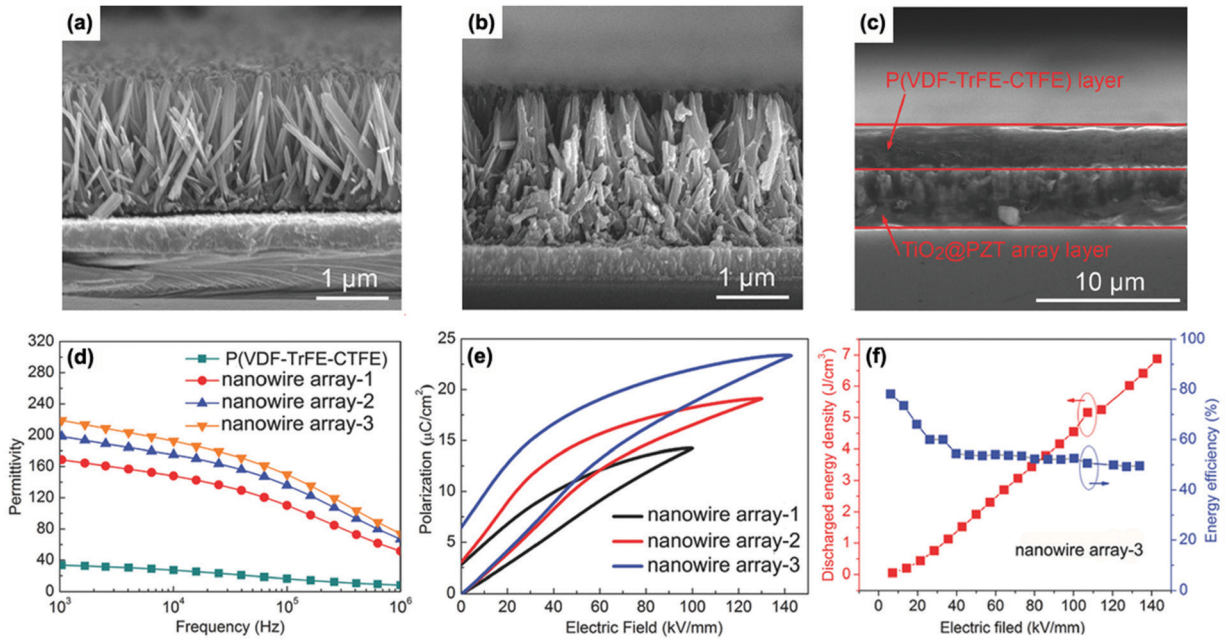

Fig. 37 Cross-sectional SEM images of (a) TiO_2 nanowire array-3 grown on FTO, (b) TiO_2@PZT nanowire array-3 and (c) TiO_2@PZT nanowire array-3/P(VDF–TrFE–CTFE) nanocomposite. (d) Relative permittivity and (e) *D*–*E* loops of the nanocomposites with different nanowire arrays. (f) The discharged energy density and efficiency of TiO_2@PZT nanowire array-3/P(VDF–TrFE–CTFE) nanocomposite.

and obtain enhanced dielectric and energy storage performance. Zhang and Luo *et al.*[274,275] successfully synthesized titanium dioxide/lead zirconate titanate (TiO_2–PZT) nanowire arrays by a simple two-step method, and demonstrated their ability to achieve high discharge energy density in P(VDF–TrFE–CTFE) based polymer composites under low operating voltage applications, as shown in Fig. 37. The orientation and density of nanowire arrays were important for the enhancement of dielectric properties and dielectric displacement. Nanowire array-1 to array-3 correspond to an intensified density of the nanowire array in polymer composites. The polymer composite with nanowire array-3 possessed the highest relative permittivity, breakdown strength, and dielectric displacement. As a result, a high discharge energy density of 6.9 J cm^{-3} was achieved at a low electric field of 143 kV mm^{-1}, which was attributed to the high relative permittivity of $\varepsilon_r \sim 218.9$ at 1 kHz and high polarization of 23.35 μC cm^{-2} at this electric field. The enhancement of relative permittivity and polarization was attributed to the different components of the composite and the interfaces between them. PZT has a high relative permittivity of $\varepsilon_r \sim 1800$ and the P(VDF–TrFE–CTFE) also has a relatively high relative permittivity of $\varepsilon_r \sim 40$.[276] The system consists of two large interfacial regions, namely the TiO_2/PZT and PZT/P(VDF–TrFE–CTFE) interfaces. Interfacial polarizations also contribute to the enhanced relative permittivity of the system, as discussed in Sections 4.1 and 4.2, and the discharge energy density obtained in this work is the highest known for a ceramic/polymer nanocomposite at such a low electric field. The filler orientation along the applied electric field direction therefore provides a promising strategy for high-energy density capacitors at a low operating voltage.

5.3 Structural design

As discussed in Sections 2–4, the use of fillers with core–shell or hierarchical structures help to improve interfacial interaction, compatibility, dispersion, breakdown strength, and interfacial polarization.[277,278] For example, Su and Yang *et al.*[278] successfully synthesized $BaTiO_3$@sheet-like TiO_2 core–shell nanoparticles with hierarchical interfaces, as shown in Fig. 38. The PVDF based nanocomposites with 2.5 vol% $BaTiO_3$@ sheet-like TiO_2 possessed a higher electric displacement (6.0 μm cm^{-2}) compared to that with 2.5 vol% $BaTiO_3$ (5.1 μm cm^{-2}) at 350 kV mm^{-1}, this was ascribed to the hierarchical interfacial polarization induced by the large surface area of the TiO_2 sheet assembled on $BaTiO_3$ nanoparticles in the nanocomposites. Moreover, an enhanced breakdown strength of 490 kV mm^{-1} was also achieved in 2.5 vol% $BaTiO_3$@TiO_2/PVDF nanocomposites compared to that of the 2.5 vol% $BaTiO_3$/PVDF nanocomposites (350 kV mm^{-1}). As a result, the energy storage density of the nanocomposites with 2.5 vol% $BaTiO_3$@TiO_2 nanoparticles attained 17.6 J cm^{-3}.

In terms of composite structures, sandwich or multi-layer structures have been shown to maintain a high dielectric strength.[279,280] Specifically, a layer with a higher breakdown strength, such as a pure polymer or a composite with a small amount of filler, is introduced into the multi-layer structured polymer composites which can improve the overall breakdown strength. The remaining nanocomposite layers contain a larger amount of fillers, which are beneficial in enhancing the electric displacement, as discussed in Section 2.4. Wang *et al.*[167] designed a sandwich-structured nanocomposite where the interfacial regions of the structure block the growth of electrical

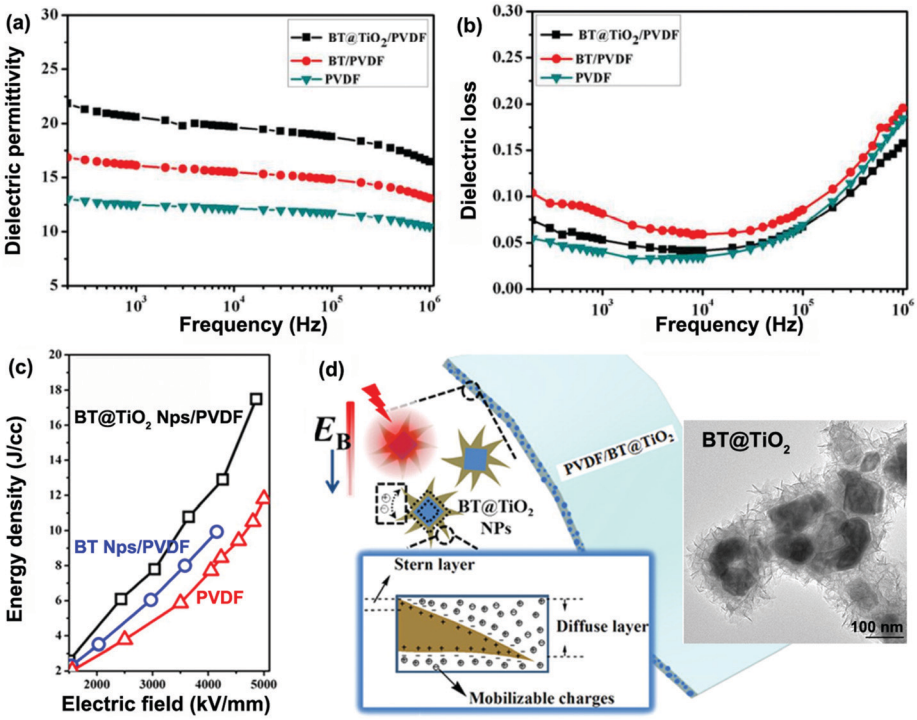

Fig. 38 (a) Frequency-dependent relative permittivity, (b) dielectric loss, (c) observed energy density of PVDF based nanocomposites embedded with $BaTiO_3$@TiO_2, $BaTiO_3$ nanoparticles and pure PVDF. (d) TEM image of $BaTiO_3$@TiO_2 nanoparticles and schematic of the origin of the ultrahigh energy density for $BaTiO_3$@TiO_2/PVDF nanocomposite. Reprinted with permission from ref. 278. Copyright (2016) American Chemical Society.

trees, thus enhancing the breakdown strength and energy density. In this structure, 1 vol% $BaTiO_3$ nanoparticles was introduced into the central layer (polymer matrix: PVDF) as the "hard layer" to ensure a high effective breakdown strength. The outer layers were based on 10–50 vol% $BaTiO_3$ nanoparticles/PVDF nanocomposites as "soft layers" to provide a high relative permittivity. The highest breakdown strength of 470 kV mm^{-1} and energy density of 18.8 J cm^{-3} were obtained when the $BaTiO_3$ loading in the soft layers was 20 vol%. Recently, a newly designed sandwich-structured $BaTiO_3$ nanoparticle/P(VDF–HFP) nanocomposite was presented where a high content of $BaTiO_3$ was introduced into the central layer to provide a high relative permittivity, while the two outer layers contained small amounts of $BaTiO_3$ to provide a favorable breakdown strength, as shown in Fig. 39a.[281] The nanocomposites with 9 wt% $BaTiO_3$ in the central layer and 1 wt% $BaTiO_3$ in the outer layers (abbreviated as 1-9-1) exhibited an ultra-high discharged energy density of 26.4 J cm^{-3} and a superior discharged efficiency of 72% at 526 kV mm^{-1}, which were the highest values achieved in sandwich-structured nanocomposites. Importantly, the performance of sandwich-structured nanocomposites 1-9-1 were better than sandwich-structured nanocomposites 9-1-9, pure P(VDF–HFP) and a single layer nanocomposite with 5 wt% $BaTiO_3$ nanoparticles, as shown in Fig. 39b–d, which indicated that the structure and filler contents of nanocomposites have a significant influence on their properties.

1D or 2D fillers have also been intensively employed in sandwich- and multi-layer structured nanocomposites. Shen and Nan *et al.*[162]

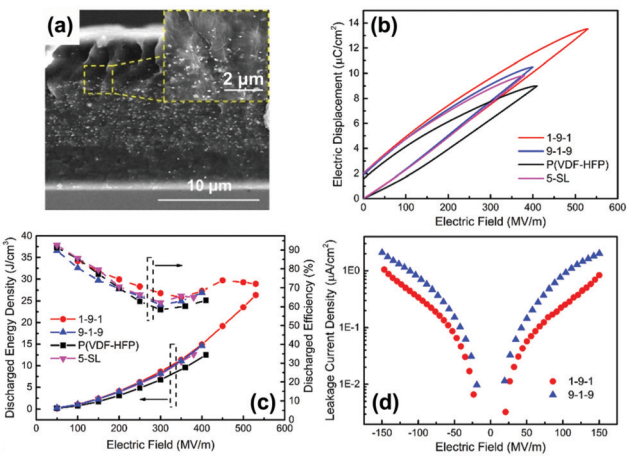

Fig. 39 (a) Cross-section SEM image of sandwich-structured $BaTiO_3$ nanoparticles/P(VDF–HFP) nanocomposites 1-9-1. Inset: SEM image of the interface between adjacent layers, scale bar 2 μm. (b) *D*–*E* loops, (c) discharged energy density and discharged efficiency of nanocomposites 1-9-1, 9-1-9, pure P(VDF–HFP), and single layer nanocomposite with 5 wt% $BaTiO_3$ nanoparticles. (d) Leakage current density-electric field curves of nanocomposites 1-9-1 and 9-1-9. Reprinted from ref. 281, Copyright (2018), with permission from Elsevier.

successfully prepared sandwich structured nanocomposites consisting of a central $BaTiO_3$ nanofiber/PVDF nanocomposite layer and two outer layers based on $BaTiO_3$ nanoparticles/PVDF nanocomposites. In the central layer, the $BaTiO_3$ nanofibers were in the preferred orientations of being perpendicular to the

applied electric field direction. The sandwich structured nanocomposites with 2 vol% $BaTiO_3$ nanofibers loaded in the central layer (thickness of 3–4 μm) and 10 vol% $BaTiO_3$ nanoparticles loaded in the outer layers (thickness of 5–6 μm) achieved the highest breakdown strength of 453 kV mm^{-1} and thereby the highest discharged energy density of 9.72 J cm^{-3}, in comparison with pure PVDF (258 kV mm^{-1}, 3.70 J cm^{-3}), 10 vol% $BaTiO_3$ nanoparticles/PVDF single layer nanocomposite (228 kV mm^{-1}, 4.23 J cm^{-3}) and 2 vol% $BaTiO_3$ nanofibers/PVDF single layer nanocomposite (347 kV mm^{-1}, 5.86 J cm^{-3}). Subsequently, they fabricated sandwich-structured nanocomposites with a GO–TiO_2/PVDF central layer and $Ba_{0.6}Sr_{0.4}TiO_3$ nanofibers/PVDF out layers.[282] The thickness of each layer was ~5 μm and the GO–TiO_2 indicates that the graphene oxide nanosheets were coated by TiO_2 nanoparticles. A high energy density of 14.6 J cm^{-3} was achieved at an electric field of 450 kV mm^{-1} in the sandwich-structured nanocomposites with 10 wt% GO–TiO_2 loading in the central layer and 3 vol% $Ba_{0.6}Sr_{0.4}TiO_3$ nanofibers loading in the outer layers. Jiang and Zhang *et al.*[78] utilized 2D $(Na_{0.5}Bi_{0.5})_{0.93}Ba_{0.07}TiO_3$ (NBBT) platelets with a size of up to 5 μm and a thickness of 0.2–0.5 μm to fabricate single layered, sandwich-structured and multi-layered NBBT@PVP/P(VDF–HFP) nanocomposites. The results indicated that five-layered nanocomposites containing three central hard layers (1 vol% NBBT loading) and neighbouring soft layers (30 vol% NBBT) showed a maximum energy storage density of 14.95 J cm^{-3} at 258 kV mm^{-1}. The energy efficiency remained 0.9 at 200 kV mm^{-1}.

Furthermore, modulation of the nanostructure of polymer composites in three dimensions has been developed in recent years to achieve a high performance. As an example, Zhang and Shen *et al.*[258,283] proposed a nonequilibrium processing method that combined electrospinning, hot-pressing and thermal etching. They fabricated several 10-layer nanocomposite films by collecting through a layer-by-layer process and simultaneously tuning the concentration and orientation of $BaTiO_3$ nanofillers in each layer, including the nanocomposites with small-large-small and large-small-large $BaTiO_3$ nanoparticles composition gradients (respectively denoted as sphere-SLS and sphere-LSL), as well as the nanocomposites with parallel and orthotropic oriented $BaTiO_3$ nanofibers (respectively denoted as fiber-parallel and fiber-orthotropic). For comparison, nanocomposites with randomly distributed $BaTiO_3$ nanospheres and nanofibers were also prepared (denoted as sphere-random and fiber-random), as shown in Fig. 40a. The out-of-plane Young's modulus and characteristic breakdown strength are shown in Fig. 40b and c, along with the

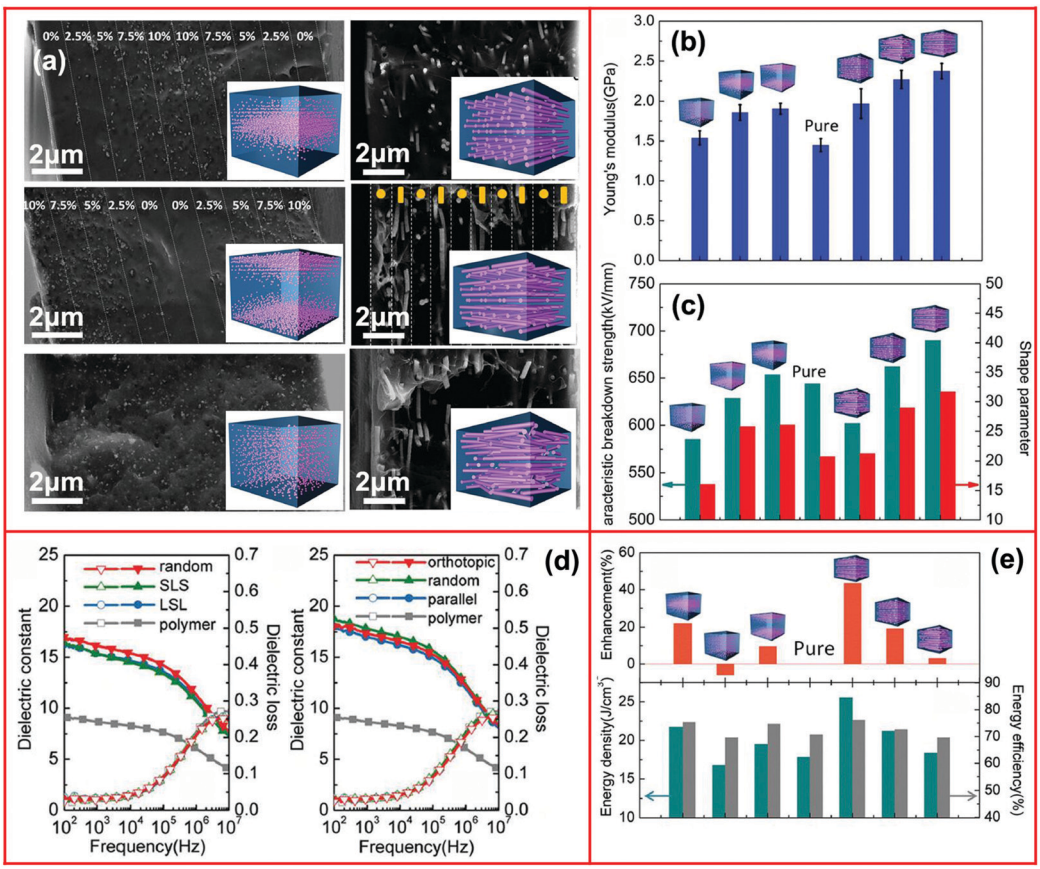

Fig. 40 (a) Schematic and cross-sectional SEM images of P(VDF–HFP)/$BaTiO_3$ nanocomposites with configurations of sphere-SLS, sphere-LSL, sphere-random, fiber-parallel, fiber-orthotropic and fiber-random. (b) The out-of-plane Young's modulus, (c) characteristic breakdown strength as well as shape parameter, (d) dielectric and (e) energy storage properties of different nanocomposites. With permission from ref. 258. Copyright 2018, John Wiley and Sons.

shape parameter of the different nanocomposites. As can be seen, the introduction of $BaTiO_3$ nanofillers can provide an improved Young's modulus compared with the pure polymer matrix. In terms of breakdown strength, only the sphere-SLS, fiber-parallel and fiber-orthotropic configurations show a higher breakdown strength compared to the polymer. Moreover, the sphere-random nanocomposites exhibited the lowest breakdown strength while the fiber-orthotropic nanocomposites showed highest breakdown strength. The enhancement of breakdown strength was attributed to the fibers impeding the propagation of breakdown paths along the out-of-plane directions and a substantial widening of breakdown paths. This was proven by a phase-field model, which simulated the initiation and real-time evolution of the electrical treeing process under an electric field along the out-of-plane direction of nanocomposite films. The relative permittivity of the nanocomposites showed an improvement compared with the pure polymer matrix, but the difference between the nanocomposite types was slight, as shown in Fig. 40d and e. Therefore the breakdown strength dominated the energy storage performance. As a result, the fiber-orthotropic nanocomposite delivered the highest energy density of 25.5 J cm^{-3} at 690 kV mm^{-1} with a discharged efficiency of 76.3%, which is an enhancement of 45.8% over that of the pure polymer ($\approx$17.8 J cm^{-3} at 640 kV mm^{-1}), as shown in Fig. 40e.

6. Summary and outlook

The state-of-the-art designs of interfaces in polymer based dielectric nanocomposites for energy storage applications have been overviewed. A wide range of interface structures have been investigated; these include the creation of core–shell structures that use (i) organic shells to improve the dispersion and compatibility with the polymeric matrix, (ii) dielectric inorganic ceramic shells to reduce electric field concentrations and mitigate the permittivity contrast between the filler and matrix; and (iii) inorganic conductive shells in an attempt to exploit the high permittivity of the system near percolation. In addition to single-phase shells, the building of hierarchical and controlled gradient structures have also been examined for multi-scale control of properties. Sandwich and multi-layer architectures have been considered to tailor the electric field distribution in layers of different relative permittivity and thereby influence the breakdown field. The influence of the morphology of additives on the interface such as filler dimension, aspect ratio, orientation with respect to applied electric field and volume fraction has been described. The impact of such interface structures on composite polarization and the energy storage capability have been discussed, along with an overview of existing models to understand the polarization mechanism and quantitatively assess the potential benefits for energy storage applications.

A detailed comparison of composites based on a variety of components, modifiers, performance and their benefits/limitations are summarized in Table 5. In summary, ceramic/polymer nanocomposites are potential dielectrics to obtain high performance, such as improved permittivity, high breakdown strength, high energy density, low density and flexibility. With regards to the use of a ceramic filler, ferroelectric ceramics with high permittivity, such as $BaTiO_3$ and $(Ba,Sr)TiO_3$ are typical choices. One-dimensional structured fillers, such as $BaTiO_3$ nanowires, with high aspect ratio is an attractive filler since introducing a low loading level (*e.g.* $<$10 vol%) of such one-dimensional structured fillers can allow the nanocomposites to obtain a high relative permittivity and maintain a high breakdown strength. Any fillers dispersed in a polymer matrix should be modified using organic materials before being incorporated into the polymer matrix, and the fluorine–polymer is an excellent modifier to improve the surface properties of the fillers, and living polymerization methods including ATRP and RAFT can obtain dense and tailored shell layers. The thicknesses and electric conductivity of the shell layers play an important role in determining the performance of the nanocomposites. Rigid polymers, such as liquid crystal polymers can be utilized to accurately control the thicknesses of the shell layers and a low electrical conductivity is needed to obtain a high breakdown strength. Generally, optimized hierarchically layered composites, such as sandwich/multi-layer structures is a feasible method to balance the paradox between high permittivity and high breakdown strength in single-layered composites and their performance can be controlled by varying the interface, chemical structure and ratios of the constituent layers.

In terms of simulation tools, finite element and phase field approaches are effective methods to theoretically describe the electric field distribution and the breakdown process in the layered composites. In addition, the oriented distribution of the fillers in polymer matrix exhibit the advantages of being able to achieve high performance, such as high breakdown strength and energy density when the aligned fillers are perpendicular to the direction of electric field; the permittivity and polarization can be enhanced when the aligned fillers are parallel to the direction of electric field.

Based on the review, a number of points can be highlighted for future research avenues on interfacial design for energy storage;

(i) The introduction of a filler of high electrical conductivity or high permittivity into a low permittivity polymer leads to electric field concentrations, in particular around the filler. While this leads to an increased relative permittivity, it also acts to increase the probability of dielectric breakdown. This technical challenge can be tackled by the fabrication of sandwich structures, but further work is required to understand the mechanisms for their intriguing properties.

(ii) Models often consider either single particle and the influence of charge transport and mobility in the composites, or the distribution of electric field in the composite structure. It would be of interest to combine such approaches to develop a unified model that considers such aspects. There is a need to examine whether an enhanced polarization at an interface, which enhances relative permittivity, is also likely to lead to dielectric breakdown.

(iii) Greater experimental characterization of the dielectric properties and phase structure of the filler–polymer interface, this can also inform modelling studies.

Table 5 Comparison of composites based on a variety of components, modifiers, performance and their benefits/limitations

Ceramic	Polymer matrix	Modifier	Modifier thickness (nm)	Molecular weight of modifier	Permittivity (at 1 kHz)	Breakdown strength (kV mm^{-1})	Discharged energy density (J cm^{-3})	Benefits	Limitations	Ref.
$BaTiO_3$	P(VDF–HFP)	Phosphonic acid	—	—	32 (50 vol%)	~215	3.2	Effectively improve dispersion using simple process	Improved dielectric loss and leakage current from residual modifiers	76
$BaTiO_3$	PVDF	Carboxylic acids	—	—	28 (50 vol% F4CBT-1)	~325	9.89	Permittivity of the nanocomposite can be adjusted by varying the coverage level of the modifiers	Modifiers do not form strong interaction with the fillers	96
$BaTiO_3$	PVA	Gallic acid (GA)	1.6	—	51 (40%BT@ GA)	144	0.554 (at 50 kV mm^{-1})	Well-dispersed nanocomposites by strengthened interfacial interaction	Limited breakdown strength and energy density due to the residual modifier (GA)	97
$BaTiO_3$	PVDF	Titanate coupling agent	2–3	—	~11.3 (4 vol% mBT-2)	517	11.27	Breakdown strength of nanocomposites was enhanced by the improved compatibility between BT nanoparticles and PVDF matrix	The shell layer is not dense and designable	99
$BaTiO_3$	PVDF	PVP	—	—	~14 (10 vol%)	336	6.8	Dielectric permittivity of the nanocomposites was enhanced by a simple surface treatment	Limited breakdown strength and energy density due to the residual modifiers PVP	100
$BaTiO_3$	P(VDF–HFP)	Hydantoin epoxy	2–3	—	~49.5 (50 vol%)	~187	7.9 (calculated value)	Environmental-friendly modifier with simple process	Limited breakdown strength and energy density due to the residual modifiers	104
$BaTiO_3$	(P(VDF–TrFE–CTFE))	(PTFMPCS)	11 ± 1	M_n = 25 800	~55 (5 vol%)	514	16.18	Thickness of shell layer can be controlled, with large effect on the performance of nanocomposites	Mismatch between the designed theoretical and practical values of shell thicknesses due to the polydispersity of modifiers	107
$BaTiO_3$	PMMA	PMMA	10	—	14.6 (76.88 wt%)	—	—	Composites with low dielectric loss due to the dense shell layer with low dielectric loss	Limited permittivity of the nanocomposite due to the low permittivity of PMMA matrix	110
$BaTiO_3$	P(VDF–TrFE–CFE)	Hyperbranched aromatic polyamide (HBP)	—	—	1484.5 (40 vol%)	17.1	—	Super-high permittivity due to enhanced interfacial polarization from the hyperbranched aromatic polyamide modifier	Limited energy density due to the low breakdown strength	111
$BaTiO_3$	HBP@PMMA	HBP@PMMA	~15	—	39.3 (56.7 wt%)	—	—	Enhanced permittivity by the double-shell modifier, which also acted as the matrix	Limited energy density due to the HBP@PMMA matrix	83
$BaTiO_3$	P(VDF–HFP)	PTFEA	2–3	M_n = 4100	~45 (50 vol%)	—	—	Improved dispersion and compatibility of $BaTiO_3$ nanoparticles in P(VDF–HFP) matrix by the dense and controllable shell layer	Modifier layer has limited effect on the permittivity of composites	86
$BaTiO_3$	Polystyrene	Polystyrene	7	—	24.51 (47.69 vol%)	—	—	Low dielectric loss and controllable by design of shell layer thickness	Low permittivity of the PS shell is not beneficial for enhancement of the nanocomposites	112

Table 5 (*continued*)

Ceramic	Polymer matrix	Modifier	Modifier thickness (nm)	Molecular weight of modifier	Permittivity (at 1 kHz)	Breakdown strength (kV mm^{-1})	Discharged energy density (J cm^{-3})	Benefits	Limitations	Ref.
$SrTiO_3$	PVDF	PVP	7	Mw = 1 300 000	~10 (2.5 vol%)	380	6.8	Improved dispersion and compatibility of $SrTiO_3$ nanofibers in PVDF matrix	Limited energy density by the existing residual modifier PVP	113
$BaTiO_3$	P(VDF–HFP)	Fluoro-polydopamine	~10	—	~14 (5 vol%)	480	12.87	Prevention of nanofiller agglomeration in the polymer matrix is more effective than dopamine functionalization	Existing residual fluoro-polydopamine in the nanocomposite due to the weak bonding force	114
$Ba_{0.8}Sr_{0.2}TiO_3$	PVDF	Ethylenediamine	—	—	~17.5 (7.5 vol%)	450	14.86	High energy density by the functionalized high aspect ratio $Ba_{0.8}Sr_{0.2}TiO_3$ nanowires	Residual ethylenediamine will increase dielectric loss of the nanocomposites and it is not beneficial for obtaining high energy efficiency	115
$BaTiO_3$	P(VDF–TrFE–CFE)	Ethylenediamine	—	—	69.5 (17.5 vol%)	300	10.48	Improved dispersion and compatibility of $BaTiO_3$ nanofibers	Relatively low breakdown strength and limited energy density by residual ethylenediamine and ternary-PVDF matrix	116
$SrTiO_3$	PVDF	Polydopamine	~10	—	~13 (5 vol%)	360	9.12	Improved the dispersion and compatibility of $SrTiO_3$ nanofibers	Relatively low breakdown strength and limited energy density due to residual dopamine	117
$0.5Ba(Zr_{0.2}Ti_{0.8})O_3$–$0.5(Ba_{0.7}Ca_{0.3})TiO_3$	PVDF	Polydopamine	—	—	~12 (3 vol%)	310	7.87	Improved dispersivity and compatibility between BZT–BCT nanofibers and PVDF matrix	Decreased breakdown strength and energy density with the increase of filler loading by the residual modifiers	118
$Ba_{0.6}Sr_{0.4}TiO_3$	PVDF	–OH	—	—	~12 (2.5 vol%)	398	6.4	Simple process to achieve enhanced breakdown strength and energy density	Cannot form a dense shell layer, therefore enhancement of energy density is limited	119
$BaTiO_3$	P(VDF–HFP)	(PMPCS)	33.3	M_n = 65 000	22.5 (7.5 vol%)	300	7.5	Dense and controllable shell layer	Enhanced interfacial polarization, relatively low energy density	124
$Na_2Ti_3O_7$	P(VDF–HFP)	PMPCS	25 ± 1.5	M_n = 60 200	69.6 (7.5 vol%)	—	—	Improvement in permittivity by the controllable shell layers thicknesses	High dielectric loss by the $Na_2Ti_3O_7$ fillers with high conductivity, enhanced interfacial polarization, limitation to energy storage	125
$BaTiO_3$/graphene	P(VDF–HFP)	Polydopamine	1–2	—	66.2 (10 vol% $BaTiO_3$ + 1.2 vol graphene)	40	—	High permittivity and low dielectric loss with conductive filler	Low breakdown strength and limitation of energy storage	127
Boron nitride	PVDF	Hydroxyl groups	5.1	—	11.1 (6 wt%)	517	13.1	Simple process to achieve enhanced breakdown strength and energy density	Cannot form a dense shell layer to effectively improve the dispersivity	71

(iv) The impact of nanofillers on the crystallisation behaviour of the matrix and enhancing the properties of the interface and matrix is of interest; further work would be of interest to explore the mechanical and dielectric properties of such interfacial regions to understand the composite properties and also inform modelling studies.

(v) The use of rigid polymers is an interesting approach, such as the use of liquid crystalline polymer to design the interface and interfacial layer thickness in a wide range of nanostructured composites for applications related to energy storage.

(vi) A high breakdown strength is extremely important for achieving a high energy density. Electric breakdown often occurs in composites with high leakage current and accumulated heat. It is of interest to further develop simulation methods, such as phase field simulations, to explore the breakdown mechanisms in such composites. Models that takes into account both the electric field concentrations, which initiates breakdown, and the subsequent breakdown path would provide a more detailed of the impact of composite architecture of dielectric strength and failure.

(vii) There is a need for the development of high-permittivity dielectric materials and high energy storage capacitors applied over a wide temperature range to meet the challenges and limitations of electronic devices with high-temperature working requirements; this can involve the use of high thermal stability polymers which brings new challenges in dielectric loss and conductivity.

(viii) Specific examples of demonstrator energy storage devices and systems related to the polymer nanocomposite dielectrics and their application is worthy of considering in future work in order to truly demonstrate the potential of these complex materials; for example applications related to Fig. 1.

Conflicts of interest

There are no conflicts to declare.

Acknowledgements

Dr H. Luo would like to acknowledge the funding from Hunan Natural Science Foundation (2019JJ40349), China Postdoctoral Science Foundation (2017M620353), Special Funding for the Postdoctoral Science Fund of China (2018T110840), and State Key Laboratory of Powder Metallurgy, Central South University, Changsha, China; Prof. D. Zhang would like to acknowledge the funding from National Natural Science Foundation of China (51672311), Science and Technology Project of Hunan Province, China (2016WK2022).

References

1 S. Luo, J. Yu, S. Yu, R. Sun, L. Cao, W.-H. Liao and C.-P. Wong, *Adv. Energy Mater.*, 2019, **9**, 1803204.
2 X. Huang, B. Sun, Y. Zhu, S. Li and P. Jiang, *Prog. Mater. Sci.*, 2019, **100**, 187–225.
3 Y. Qiao, X. Yin, T. Zhu, H. Li and C. Tang, *Prog. Mater. Sci.*, 2018, **80**, 153–162.
4 Z. Pan, L. Yao, J. Zhai, X. Yao and H. Chen, *Adv. Mater.*, 2018, **30**, 1705662.
5 Q. Li, L. Chen, M. R. Gadinski, S. Zhang, G. Zhang, H. Li, A. Haque, L.-Q. Chen, T. N. Jackson and Q. Wang, *Nature*, 2015, **523**, 576–579.
6 Y. Yang, J. He, Q. Li, L. Gao, J. Hu, R. Zeng, J. Qin, S. X. Wang and Q. Wang, *Nat. Nanotechnol.*, 2019, **14**, 151–155.
7 Prateek, V. K. Thakur and R. K. Gupta, *Chem. Rev.*, 2016, **116**, 4260–4317.
8 Q. Chen, Y. Shen, S. Zhang and Q. M. Zhang, *Annu. Rev. Mater. Res.*, 2015, **45**, 433–458.
9 Z.-M. Dang, M.-S. Zheng and J.-W. Zha, *Small*, 2016, **12**, 1688–1701.
10 J. S. Ho and S. G. Greenbaum, *ACS Appl. Mater. Interfaces*, 2018, **10**, 29189–29218.
11 X. Hu, K. Yi, J. Liu and B. Chu, *Energy Technol.*, 2018, **6**, 849–864.
12 L. Yang, X. Kong, F. Li, H. Hao, Z. Cheng, H. Liu, J.-F. Li and S. Zhang, *Prog. Mater. Sci.*, 2019, **102**, 72–108.
13 J. R. Laghari and W. J. Sarjeant, *IEEE Trans. Power Electron.*, 1992, **7**, 251–257.
14 H. Qi and R. Zuo, *J. Mater. Chem. A*, 2019, **7**, 3971–3978.
15 Q. Li, F.-Z. Yao, Y. Liu, G. Zhang, H. Wang and Q. Wang, *Annu. Rev. Mater. Res.*, 2018, **48**, 219–243.
16 Z. Yao, Z. Song, H. Hao, Z. Yu, M. Cao, S. Zhang, M. T. Lanagan and H. Liu, *Adv. Mater.*, 2017, **29**, 1601727.
17 H. Kishi, Y. Mizuno and H. Chazono, *Jpn. J. Appl. Phys.*, 2003, **42**, 1–15.
18 H. Du, X. Lin, H. Zheng, B. Qu, Y. Huang and D. Chu, *J. Alloys Compd.*, 2016, **663**, 848–861.
19 B. Chu, X. Zhou, K. Ren, B. Neese, M. Lin, Q. Wang, F. Bauer and Q. M. Zhang, *Science*, 2006, **313**, 334–336.
20 P. Khanchaitit, K. Han, M. R. Gadinski, Q. Li and Q. Wang, *Nat. Commun.*, 2013, **4**, 2845.
21 Q. M. Zhang, H. Li, M. Poh, F. Xia, Z. Y. Cheng, H. Xu and C. Huang, *Nature*, 2002, **419**, 284–287.
22 H. Li, F. Liu, B. Fan, D. Ai, Z. Peng and Q. Wang, *Small Methods*, 2018, **2**, 1700399.
23 S. Guan, H. Li, S. Zhao and L. Guo, *Compos. Sci. Technol.*, 2018, **158**, 79–85.
24 Y. Qiao, M. S. Islam, K. Han, E. Leonhardt, J. Zhang, Q. Wang, H. J. Ploehn and C. Tang, *Adv. Funct. Mater.*, 2013, **23**, 5638–5646.
25 X. Hao, *J. Adv. Dielectr.*, 2013, **3**, 1330001.
26 M. S. Whittingham, *MRS Bull.*, 2008, **33**, 411–419.
27 D. Han, J. Zhang, Z. Weng, D. Kong, Y. Tao, F. Ding, D. Ruan and Q. H. Yang, *Mater. Today Energy*, 2019, **11**, 30–45.
28 H. Deng and Q. Fu, *Macromol. Rapid Commun.*, 2017, **38**, 1700444.
29 J. Yuan, *Chin. Chem. Lett.*, 2017, **28**, 2036–2044.
30 Y. Wu, Z. Wang, X. Shen, X. Liu, N. M. Han, Q. Zheng, Y.-W. Ma and J.-K. Kim, *ACS Appl. Mater. Interfaces*, 2018, **10**, 26641–26652.

31 J. Chen, Y. Wang, H. Li, H. Han, X. Liao, R. Sun, X. Huang and M. Xie, *Chem. Mater.*, 2018, **30**, 1102–1112.
32 Z. Liu, T. Lu, J. Ye, G. Wang, X. Dong, R. Withers and Y. Liu, *Adv. Mater. Technol.*, 2018, **3**, 1800111.
33 C. Yang, H. Wei, L. Guan, J. Guo, Y. Wang, X. Yan, X. Zhang, S. Wei and Z. Guo, *J. Mater. Chem. A*, 2015, **3**, 14929–14941.
34 Z.-M. Dang, J.-K. Yuan, J.-W. Zha, T. Zhou, S.-T. Li and G.-H. Hu, *Prog. Mater. Sci.*, 2012, **57**, 660–723.
35 S. Cho, J. S. Lee and J. Jang, *ACS Appl. Mater. Interfaces*, 2015, **7**, 9668–9681.
36 X. Zhang, B.-W. Li, L. Dong, H. Liu, W. Chen, Y. Shen and C.-W. Nan, *Adv. Mater. Interfaces*, 2018, **5**, 1800096.
37 Y. Zhang, C. Zhang, Y. Feng, T. Zhang, Q. Chen, Q. Chi, L. Liu, G. Li, Y. Cui, X. Wang, Z. Dang and Q. Lei, *Nano Energy*, 2019, **56**, 138–150.
38 L. Wu, K. Wu, C. Lei, D. Liu, R. Du, F. Chen and Q. Fu, *J. Mater. Chem. A*, 2019, **7**, 7664–7674.
39 B. Zhao, M. Hamidinejad, C. Zhao, R. Li, S. Wang, Y. Kazemi and C. B. Park, *J. Mater. Chem. A*, 2019, **7**, 133–140.
40 X. Hao, Y. Wang, J. Yang, S. An and J. Xu, *J. Appl. Phys.*, 2012, **112**, 114111.
41 B. Chu, M. Lin, B. Neese, X. Zhou, Q. Chen and Q. M. Zhang, *Appl. Phys. Lett.*, 2007, **91**, 122909.
42 S. Li, S. Yu and Y. Feng, *High Voltage*, 2016, **1**, 122–129.
43 P. Martins, A. C. Lopes and S. Lanceros-Mendez, *Prog. Mater. Sci.*, 2014, **39**, 683–706.
44 H. Tran Doan, S. Boggs, G. Teyssedre, C. Laurent, M. Cakmak, S. Kumar and R. Ramprasad, *Prog. Mater. Sci.*, 2016, **83**, 236–269.
45 S. L. Zhong, Z. M. Dang, W. Y. Zhou and H. W. Cai, *IET Nanodielectr.*, 2018, **1**, 41–47.
46 Z. M. Dang, J. K. Yuan, S. H. Yao and R. J. Liao, *Adv. Mater.*, 2013, **25**, 6334–6365.
47 L. Zhu, *J. Phys. Chem. Lett.*, 2014, **5**, 3677–3687.
48 B. Jiang, J. Iocozzia, L. Zhao, H. Zhang, Y.-W. Harn, Y. Chen and Z. Lin, *Chem. Soc. Rev.*, 2019, **48**, 1194–1228.
49 E. Baer and L. Zhu, *Macromolecules*, 2017, **50**, 2239–2256.
50 Y. Wang, J. Chen, Y. Li, Y. Niu, Q. Wang and H. Wang, *J. Mater. Chem. A*, 2019, **7**, 2965–2980.
51 H. Palneedi, M. Peddigari, G.-T. Hwang, D.-Y. Jeong and J. Ryu, *Adv. Funct. Mater.*, 2018, **28**, 1803665.
52 K. B. N. Balasubramanian and T. Ramesh, *Polym. Adv. Technol.*, 2018, **29**, 1568–1585.
53 M. H. Al-Saleh, *Nanotechnology*, 2019, **30**, 062001.
54 U. O. Uyor, A. P. Popoola, O. Popoola and V. S. Aigbodion, *Adv. Polym. Technol.*, 2018, **37**, 2838–2858.
55 Y. Niu and H. Wang, *ACS Appl. Nano Mater.*, 2019, **2**, 627–642.
56 D. Q. Tan, *Adv. Funct. Mater.*, 2019, 1808567.
57 X. Huang and P. Jiang, *Adv. Mater.*, 2015, **27**, 546–554.
58 F. Caruso, *Adv. Mater.*, 2001, **13**, 11–22.
59 G. Cao, *Nanostructures & Nanomaterials-Synthesis, Properties & Applications*, Imperial College Press, 2004.
60 S. Ramakrishna, *An Introduction to Electrospinning and Nanofibers*, World Scientific Publishing Co. Pte. Ltd, 2005.
61 P. J. Burke, *Nanotubes and Nanowires*, World Scientific Publishing Co. Pte. Ltd., 2005.
62 X. Han, S. Chen, X. Lv, H. Luo, D. Zhang and C. R. Bowen, *Phys. Chem. Chem. Phys.*, 2018, **20**, 2826–2837.
63 M. Lewin, A. Mey-Marom and R. Frank, *Polym. Adv. Technol.*, 2005, 429–441.
64 W. Schaertl, *Nanoscale*, 2010, **2**, 829–843.
65 R. G. Chaudhuri and S. Paria, *Chem. Rev.*, 2012, **112**, 2373–2433.
66 M. B. Gawande, A. Goswami, T. Asefa, H. Guo, A. V. Biradar, D.-L. Peng, R. Zboril and R. S. Varma, *Chem. Soc. Rev.*, 2015, **44**, 7540–7590.
67 H. Heinz, C. Pramanik, O. Heinz, Y. Ding, R. K. Mishra, D. Marchon, R. J. Flatt, I. Estrela-Lopis, J. Llop, S. Moya and R. F. Ziolo, *Surf. Sci. Rep.*, 2017, **72**, 1–58.
68 W. Xu, G. Yang, L. Jin, J. Liu, Y. Zhang, Z. Zhang and Z. Jiang, *ACS Appl. Mater. Interfaces*, 2018, **10**, 11233–11241.
69 Z. Li, F. Liu, G. Yang, H. Li, L. Dong, C. Xiong and Q. Wang, *Compos. Sci. Technol.*, 2018, **164**, 214–221.
70 H. Feng, X. Fang, X. Liu, Q. Pei, Z.-K. Cui, S. Deng, J. Gu and Q. Zhuang, *Composites, Part A*, 2018, **109**, 578–584.
71 L. Wu, K. Wu, D. Liu, R. Huang, J. Huo, F. Chen and Q. Fu, *J. Mater. Chem. A*, 2018, **6**, 7573–7584.
72 H. Ye, T. Lu, C. Xu, M. Zhong and L. Xu, *Nanotechnology*, 2018, **29**, 095702.
73 Y. Song, Y. Shen, H. Liu, Y. Lin, M. Li and C.-W. Nan, *J. Mater. Chem.*, 2012, **22**, 8063–8068.
74 H. Luo, C. Chen, K. Zhou, X. Zhou, Z. Wu and D. Zhang, *RSC Adv.*, 2015, **5**, 68515–68522.
75 Z.-M. Dang, H.-Y. Wang and H.-P. Xu, *Appl. Phys. Lett.*, 2006, **89**, 112902.
76 P. Kim, N. M. Doss, J. P. Tillotson, P. J. Hotchkiss, M.-J. Pan, S. R. Marder, J. Li, J. P. Calame and J. W. Perry, *ACS Nano*, 2009, **3**, 2581–2592.
77 J. Li, J. Claude, L. E. Norena-Franco, S. Il Seok and Q. Wang, *Chem. Mater.*, 2008, **20**, 6304–6306.
78 C. Jiang, D. Zhang, K. Zhou, X. Zhou, H. Luo and I. Abrahams, *J. Mater. Chem. A*, 2016, **4**, 18050–18059.
79 D. Zhang, Z. Wu, X.-F. Zhou, A.-Q. Wei, C. Chen and H. Luo, *Sens. Actuators, A*, 2017, **260**, 228–235.
80 H. Lee, S. M. Dellatore, W. M. Miller and P. B. Messersmith, *Science*, 2007, **318**, 426–430.
81 Z.-M. Dang, T. Zhou, S.-H. Yao, J.-K. Yuan, J.-W. Zha, H.-T. Song, J.-Y. Li, Q. Chen, W.-T. Yang and J. Bai, *Adv. Mater.*, 2009, **21**, 2077–2082.
82 K. Yang, X. Huang, M. Zhu, L. Xie, T. Tanaka and P. Jiang, *ACS Appl. Mater. Interfaces*, 2014, **6**, 1812–1822.
83 L. Xie, X. Huang, Y. Huang, K. Yang and P. Jiang, *J. Phys. Chem. C*, 2013, **117**, 22525–22537.
84 K. Yang, X. Huang, L. Fang, J. He and P. Jiang, *Nanoscale*, 2014, **6**, 14740–14753.
85 P. Kim, S. C. Jones, P. J. Hotchkiss, J. N. Haddock, B. Kippelen, S. R. Marder and J. W. Perry, *Adv. Mater.*, 2007, **19**, 1001–1005.
86 K. Yang, X. Huang, Y. Huang, L. Xie and P. Jiang, *Chem. Mater.*, 2013, **25**, 2327–2338.

87 M. Rahimabady, M. S. Mirshekarloo, K. Yao and L. Lu, *Phys. Chem. Chem. Phys.*, 2013, **15**, 16242–16248.
88 D. He, Y. Wang, X. Chen and Y. Deng, *Composites, Part A*, 2017, **93**, 137–143.
89 J. Chen, X. Wang, X. Yu, L. Yao, Z. Duan, Y. Fan, Y. Jiang, Y. Zhou and Z. Pan, *J. Mater. Chem. C*, 2018, **6**, 271–279.
90 J. Chen, X. Wang, X. Yu, Y. Fan, Z. Duan, Y. Jiang, F. Yang and Y. Zhou, *Appl. Surf. Sci.*, 2018, **447**, 704–710.
91 K. Yu, Y. Niu, Y. Bai, Y. Zhou and H. Wang, *Appl. Phys. Lett.*, 2013, **102**, 102903.
92 S. Liu, S. Xue, B. Shen and J. Zhai, *Appl. Phys. Lett.*, 2015, **107**, 032907.
93 H. Tang, Z. Zhou, C. C. Bowland and H. A. Sodano, *Nano Energy*, 2015, **17**, 302–307.
94 S. Liu, J. Wang, B. Shen, J. Zhai, H. Hao and L. Zhao, *J. Alloys Compd.*, 2017, **696**, 136–142.
95 K. Bi, M. Bi, Y. Hao, W. Luo, Z. Cai, X. Wang and Y. Huang, *Nano Energy*, 2018, **51**, 513–523.
96 Y. Niu, F. Xiang, Y. Wang, J. Chen and H. Wang, *Phys. Chem. Chem. Phys.*, 2018, **20**, 6598–6605.
97 Z.-H. Dai, T. Li, Y. Gao, J. Xu, Y. Weng, J. He and B.-H. Guo, *Colloids Surf., A*, 2018, **548**, 179–190.
98 J. Fu, Y. Hou, M. Zheng, Q. Wei, M. Zhu and H. Yan, *ACS Appl. Mater. Interfaces*, 2015, **7**, 24480–24491.
99 P. Hu, S. Gao, Y. Zhang, L. Zhang and C. Wang, *Compos. Sci. Technol.*, 2018, **156**, 109–116.
100 K. Yu, Y. Niu, Y. Zhou, Y. Bai and H. Wang, *J. Am. Ceram. Soc.*, 2013, **96**, 2519–2524.
101 Z. Wang, T. Wang, C. Wang, Y. Xiao, P. Jing, Y. Cui and Y. Pu, *ACS Appl. Mater. Interfaces*, 2017, **9**, 29130–29139.
102 Z.-H. Dai, J.-R. Han, Y. Gao, J. Xu, J. He and B.-H. Guo, *Colloids Surf., A*, 2017, **529**, 560–570.
103 L. Li, R. Feng, Y. Zhang and L. Dong, *J. Mater. Chem. C*, 2017, **5**, 11403–11410.
104 H. Luo, D. Zhang, C. Jiang, X. Yuan, C. Chen and K. Zhou, *ACS Appl. Mater. Interfaces*, 2015, **7**, 8061–8069.
105 L. Xie, X. Huang, K. Yang, S. Li and P. Jiang, *J. Mater. Chem. A*, 2014, **2**, 5244–5251.
106 G. Zhang, Y. Li, S. Tang, R. D. Thompson and L. Zhu, *ACS Appl. Mater. Interfaces*, 2017, **9**, 10106–10119.
107 S. Chen, X. Lv, X. Han, H. Luo, C. R. Bowen and D. Zhang, *Polym. Chem.*, 2018, **9**, 548–557.
108 M. Li, X. Huang, C. Wu, H. Xu, P. Jiang and T. Tanaka, *J. Mater. Chem.*, 2012, **22**, 23477–23484.
109 Y. Huang, X. Huang, L. S. Schadler, J. He and P. Jiang, *ACS Appl. Mater. Interfaces*, 2016, **8**, 25496–25507.
110 L. Xie, X. Huang, C. Wu and P. Jiang, *J. Mater. Chem.*, 2011, **21**, 5897–5906.
111 L. Xie, X. Huang, Y. Huang, K. Yang and P. Jiang, *ACS Appl. Mater. Interfaces*, 2013, **5**, 1747–1756.
112 K. Yang, X. Huang, L. Xie, C. Wu, P. Jiang and T. Tanaka, *Macromol. Rapid Commun.*, 2012, **33**, 1921–1926.
113 S. Liu and J. Zhai, *J. Mater. Chem. A*, 2015, **3**, 1511–1517.
114 G. Wang, X. Huang and P. Jiang, *ACS Appl. Mater. Interfaces*, 2017, **9**, 7547–7555.
115 H. Tang and H. A. Sodano, *Nano Lett.*, 2013, **13**, 1373–1379.
116 H. Tang, Y. Lin and H. A. Sodano, *Adv. Energy Mater.*, 2013, **3**, 451–456.
117 L. Yao, Z. Pan, J. Zhai, G. Zhang, Z. Liu and Y. Liu, *Composites, Part A*, 2018, **109**, 48–54.
118 Q. Chi, T. Ma, Y. Zhang, Y. Cui, C. Zhang, J. Lin, X. Wang and Q. Lei, *J. Mater. Chem. A*, 2017, **5**, 16757–16766.
119 S. Liu, J. Zhai, J. Wang, S. Xue and W. Zhang, *ACS Appl. Mater. Interfaces*, 2014, **6**, 1533–1540.
120 S. Liu, S. Xue, W. Zhang, J. Zhai and G. Chen, *J. Mater. Chem. A*, 2014, **2**, 18040–18046.
121 A. E. Daugaard, K. Jankova, J. M. R. Marin, J. Bogelund and S. Hvilsted, *Eur. Polym. J.*, 2012, **48**, 743–750.
122 H. Luo, Z. Wu, C. Chen, C. Ma, K. Zhou and D. Zhang, *Composites, Part A*, 2016, **86**, 57–65.
123 Z. B. Pan, L. M. Yao, G. L. Ge, B. Shen and J. W. Zhai, *J. Mater. Chem. A*, 2018, **6**, 14614–14622.
124 D. Zhang, C. Ma, X. Zhou, S. Chen, H. Luo, C. R. Bowen and K. Zhou, *J. Phys. Chem. C*, 2017, **121**, 20075–20083.
125 H. Luo, C. Ma, X. Zhou, S. Chen and D. Zhang, *Macromolecules*, 2017, **50**, 5132–5137.
126 D. Wang, Y. Bao, J.-W. Zha, J. Zhao, Z.-M. Dang and G.-H. Hu, *ACS Appl. Mater. Interfaces*, 2012, **4**, 6273–6279.
127 H. Luo, Z. Wu, X. Zhou, Z. Yan, K. Zhou and D. Zhang, *Compos. Sci. Technol.*, 2018, **160**, 237–244.
128 X. Zhi, Y. Mao, S. Wen, Y. Li, L. Zhang, T. W. Chan and L. Liu, *Composites, Part A*, 2015, **76**, 194–202.
129 X. Fang, X. Liu, Z.-K. Cui, J. Qian, J. Pan, X. Li and Q. Zhuang, *J. Mater. Chem. A*, 2015, **3**, 10005–10012.
130 H. Feng, W. Ma, Z.-K. Cui, X. Liu, J. Gu, S. Lin and Q. Zhuang, *J. Mater. Chem. A*, 2017, **5**, 8705–8713.
131 Q. Huang, H. Luo, C. Chen, X. Zhou, K. Zhou and D. Zhang, *J. Alloys Compd.*, 2016, **696**, 1220–1227.
132 M. Yang, H. Zhao, C. Hu, P. Haghi-Ashtiani, D. He, Z.-M. Dang and J. Bai, *Phys. Chem. Chem. Phys.*, 2018, **20**, 2777–2786.
133 F. Liang, L. Zhang, W.-Z. Lu, Q.-X. Wan and G.-F. Fan, *Appl. Phys. Lett.*, 2016, **108**, 072902.
134 Z. Li, L. A. Fredin, P. Tewari, S. A. DiBenedetto, M. T. Lanagan, M. A. Ratner and T. J. Marks, *Chem. Mater.*, 2010, **22**, 5154–5164.
135 C. Zhang, Q. Chi, J. Dong, Y. Cui, X. Wang, L. Liu and Q. Lei, *Sci. Rep.*, 2016, **6**, 33508.
136 X. Huo, W. Li, J. Zhu, L. Li, Y. Li, L. Luo and Y. Zhu, *J. Phys. Chem. C*, 2015, **119**, 25786–25791.
137 Q. G. Chi, J. F. Dong, C. H. Zhang, C. P. Wong, X. Wang and Q. Q. Lei, *J. Mater. Chem. C*, 2016, **4**, 8179–8188.
138 Y. Zhang, Y. Wang, Y. Deng, M. Li and J. Bai, *ACS Appl. Mater. Interfaces*, 2012, **4**, 65–68.
139 R. Su, Z. Luo, D. Zhang, Y. Liu, Z. Wang, J. Li, J. Bian, Y. Li, X. Hu and J. Gao, *J. Phys. Chem. C*, 2016, 120.
140 X. Lin, P. Hu, Z. Jia and S. Gao, *J. Mater. Chem. A*, 2016, **4**, 2314–2320.
141 X. Zhang, Y. Shen, B. Xu, Q. Zhang, L. Gu, J. Jiang, J. Ma, Y. Lin and C. W. Nan, *Adv. Mater.*, 2016, **28**, 2055.
142 G. Wang, Y. Huang, Y. Wang, P. Jiang and X. Huang, *Phys. Chem. Chem. Phys.*, 2017, **19**, 21058–21068.

143 Z. Pan, L. Yao, J. Zhai, D. Fu, B. Shen and H. Wang, *ACS Appl. Mater. Interfaces*, 2017, **9**, 4024–4033.
144 D. He, Y. Wang, S. Song, S. Liu and Y. Deng, *ACS Appl. Mater. Interfaces*, 2017, **9**, 44839–44846.
145 D. He, Y. Wang, S. Song, S. Liu, Y. Luo and Y. Deng, *Compos. Sci. Technol.*, 2017, **151**, 25–33.
146 Q. Chi, T. Ma, Y. Zhang, Q. Chen, C. Zhang, Y. Cui, T. Zhang, J. Lin, X. Wang and Q. Lei, *ACS Sustainable Chem. Eng.*, 2018, **6**, 403–412.
147 J. Wang, Y. Long, Y. Sun, X. Zhang, H. Yang and B. Lin, *Appl. Surf. Sci.*, 2017, **426**, 437–445.
148 Y. Feng, W. L. Li, J. P. Wang, J. H. Yin and W. D. Fei, *J. Mater. Chem. A*, 2015, **3**, 20313–20321.
149 L. Huang, P. Zhu, G. Li, D. Lu, R. Sun and C. Wong, *J. Mater. Chem. A*, 2014, **2**, 18246–18255.
150 S. Luo, S. Yu, R. Sun and C.-P. Wong, *ACS Appl. Mater. Interfaces*, 2014, **6**, 176–182.
151 Z. Chen, H. Li, G. Xie and K. Yang, *RSC Adv.*, 2018, **8**, 1–9.
152 K. Yang, X. Huang, J. He and P. Jiang, *Adv. Mater. Interfaces*, 2015, **2**, 1500361.
153 M. Yang, C. Hu, H. Zhao, P. Haghi-Ashtiani, D. He, Y. Yang, J. Yuan and J. Bai, *Carbon*, 2018, **132**, 152–156.
154 Z. Pan, J. Zhai and B. Shen, *J. Mater. Chem. A*, 2017, **5**, 15217–15226.
155 L. Wang, X. Huang, Y. Zhu and P. Jiang, *Phys. Chem. Chem. Phys.*, 2018, **20**, 5001–5011.
156 D. Yu, N. X. Xu, L. Hu, Q. L. Zhang and H. Yang, *J. Mater. Chem. C*, 2015, **3**, 4016–4022.
157 W. S. Gutowski, *J. Adhes.*, 2003, **79**, 445–482.
158 Z. Pan, L. Yao, J. Zhai, B. Shen, S. Liu, H. Wang and J. Liu, *J. Mater. Chem. A*, 2016, **4**, 13259–13264.
159 Z. Pan, M. Wang, J. Chen, S. Bo, J. Liu and J. Zhai, *Nanoscale*, 2018, **10**, 16621–16629.
160 Prateek, R. Bhunia, S. Siddiqui, A. Garg and R. K. Gupta, *ACS Appl. Mater. Interfaces*, 2019, **11**, 14329–14339.
161 H. Luo, K. Zhou, C. Bowen, F. Zhang, A. Wei, Z. Wu, C. Chen and D. Zhang, *Adv. Mater. Interfaces*, 2016, **3**, 1600157.
162 P. Hu, Y. Shen, Y. Guan, X. Zhang, Y. Lin, Q. Zhang and C.-W. Nan, *Adv. Funct. Mater.*, 2014, **24**, 3172–3178.
163 P. Hu, J. Wang, Y. Shen, Y. Guan, Y. Lin and C.-W. Nan, *J. Mater. Chem. A*, 2013, **1**, 12321–12326.
164 Y. Feng, M.-L. Li, W.-L. Li, T.-D. Zhang, Y. Zhao and W.-D. Fei, *Appl. Phys. Lett.*, 2018, **112**, 022901.
165 Y. Zhang, W. Li, S. Xu, Z. Wang, Y. Zhao, J. Li and W. Fei, *J. Mater. Chem. A*, 2018, **6**, 24550–24559.
166 H. Luo, D. Zhang, L. Wang, C. Chen, J. Zhou and K. Zhou, *RSC Adv.*, 2015, **5**, 52809–52816.
167 Y. Wang, J. Cui, Q. Yuan, Y. Niu, Y. Bai and H. Wang, *Adv. Mater.*, 2015, **27**, 6658–6663.
168 L. L. Sun, B. Li, Y. Zhao, G. Mitchell and W. H. Zhong, *Nanotechnology*, 2010, **21**, 305702.
169 Y. N. Hao, X. H. Wang, S. O'Brien, J. Lombardi and L. T. Li, *J. Mater. Chem. C*, 2015, **3**, 9740–9747.
170 Y. Zhang, Q. Chi, L. Liu, C. Zhang, C. Chen, X. Wang and Q. Lei, *APL Mater.*, 2017, **5**, 076109.
171 J. Chen, Y. Wang, X. Xu, Q. Yuan, Y. Niu, Q. Wang and H. Wang, *J. Mater. Chem. A*, 2018, **6**, 24367–24377.
172 Z. Pan, B. Liu, J. Zhai, L. Yao, K. Yang and B. Shen, *Nano Energy*, 2017, **40**, 587–595.
173 Y. Wang, L. Wang, Q. Yuan, Y. Niu, J. Chen, Q. Wang and H. Wang, *J. Mater. Chem. A*, 2017, **5**, 10849–10855.
174 Q. Li, F. Liu, T. Yang, M. R. Gadinski, G. Zhang, L.-Q. Chen and Q. Wang, *Proc. Natl. Acad. Sci. U. S. A.*, 2016, **113**, 9995–10000.
175 J. Lao, H. Xie, Z. Shi, G. Li, B. Li, G.-H. Hu, Q. Yang and C. Xiong, *ACS Sustainable Chem. Eng.*, 2018, **6**, 7151–7158.
176 F. Liu, Q. Li, J. Cui, Z. Li, G. Yang, Y. Liu, L. Dong, C. Xiong, H. Wang and Q. Wang, *Adv. Funct. Mater.*, 2017, **27**, 1606292.
177 S. Song, Y. Wang, Y. Luo, D. He, A. Abella and Y. Deng, *Mater. Des.*, 2018, **140**, 114–122.
178 J. O. Zoppe, N. C. Ataman, P. Mocny, J. Wang, J. Moraes and H.-A. Klok, *Chem. Rev.*, 2017, **117**, 1105–1318.
179 Y. Qiao, M. S. Islam, L. Wang, Y. Yan, J. Zhang, B. C. Benicewicz, H. J. Ploehn and C. Tang, *Chem. Mater.*, 2014, **26**, 5319–5326.
180 Y. Chen, Z. Wang, Y. He, Y. J. Yoon, J. Jung, G. Zhang and Z. Lin, *Proc. Natl. Acad. Sci. U. S. A.*, 2018, **115**, 1391–1400.
181 Y. Chen, D. Yang, Y. J. Yoon, X. Pang, Z. Wang, J. Jung, Y. He, Y. W. Harn, M. He, S. Zhang, G. Zhang and Z. Lin, *J. Am. Chem. Soc.*, 2017, **139**, 12956–12967.
182 Y. Chen, Y. J. Yoon, X. Pang, Y. He, J. Jung, C. Feng, G. Zhang and Z. Lin, *Small*, 2016, **12**, 6714–6723.
183 D. Yang, Y. Chen, H. Peng, G. Chen and Z. Lin, *Nanoscale*, 2018, **10**, 22750–22757.
184 Y. Chen, T. Gan, C. Ma, L. Wang and G. Zhang, *J. Phys. Chem. B*, 2016, **120**, 4715–4722.
185 C. Feng, X. Pang, Y. He, Y. Chen, G. Zhang and Z. Lin, *Polym. Chem.*, 2015, **6**, 5190–5197.
186 B. Jiang, X. Pang, B. Li and Z. Lin, *J. Am. Chem. Soc.*, 2015, **137**, 11760–11767.
187 X. Liu, J. Iocozzia, Y. Wang, X. Cui, Y. Chen, S. Zhao, Z. Li and Z. Lin, *Energy Environ. Sci.*, 2017, **10**, 402–434.
188 X. Li, J. Iocozzia, Y. Chen, S. Zhao, X. Cui, W. Wang, H. Yu, S. Lin and Z. Lin, *Angew. Chem., Int. Ed.*, 2018, **57**, 2046–2070.
189 X. Pang, Y. He, B. Jiang, J. Iocozzia, L. Zhao, H. Guo, J. Liu, M. Akinc, N. Bowler, X. Tan and Z. Lin, *Nanoscale*, 2013, **5**, 8695–8702.
190 H. Z. Guo, Y. Mudryk, M. I. Ahmad, X. C. Pang, L. Zhao, M. Akinc, V. K. Pecharsky, N. Bowler, Z. Q. Lin and X. Tan, *J. Mater. Chem.*, 2012, **22**, 23944–23951.
191 J. Wang, X. Pang, M. Akinc and Z. Lin, *J. Mater. Chem.*, 2010, **20**, 5945–5949.
192 Y. Niu, Y. Bai, K. Yu, Y. Wang, F. Xiang and H. Wang, *ACS Appl. Mater. Interfaces*, 2015, **7**, 24168–24176.
193 X. F. Chen, Z. Shen, X. H. Wan, X. H. Fan, E. Q. Chen, Y. Ma and Q. F. Zhou, *Chem. Soc. Rev.*, 2010, **39**, 3072–3101.
194 X. Yang, Z. Xiang, S. Chen, H. Luo, D. Zhang and H. Zhang, *New J. Chem.*, 2017, **41**, 7553–7561.
195 X. Liang, X. Chen, C. Y. Li, Z. Shen, X. Fan and Q. Zhou, *Polymer*, 2010, **51**, 3693–3705.

196 Z. Y. Kuang, Y. J. Fan, L. Tao, M. L. Li, N. Zhao, P. Wang, E. Q. Chen, F. Fan and H. L. Xie, *ACS Appl. Mater. Interfaces*, 2018, **10**, 27269–27277.
197 P. Li, S. Chen, H. Luo, D. Zhang and H. Zhang, *J. Polym. Sci., Polym. Chem.*, 2017, **55**, 754–766.
198 S. Chen, H. Luo, H. L. Xie and H. L. Zhang, *Polymer*, 2013, **54**, 1794–1802.
199 D. Zhang, Y. X. Liu, A. Xinhua Wan and Q. F. Zhou, *Macromolecules*, 1999, **32**, 5183–5185.
200 L. Y. Shi, Y. Zhou, X. H. Fan and Z. Shen, *Macromolecules*, 2013, **46**, 5308–5316.
201 K. Qian, X. Lv, S. Chen, H. Luo and D. Zhang, *Dalton Trans.*, 2018, **47**, 12759–12768.
202 H. Luo, S. Chen, L. Liu, X. Zhou, C. Ma, W. Liu and D. Zhang, *ACS Sustainable Chem. Eng.*, 2019, **7**, 3145–3153.
203 L. A. Fredin, Z. Li, M. A. Ratner, M. T. Lanagan and T. J. Marks, *Adv. Mater.*, 2012, **24**, 5946–5953.
204 D. Kang, G. Wang, Y. Huang, P. Jiang and X. Huang, *ACS Appl. Mater. Interfaces*, 2018, **10**, 4077–4085.
205 X. Zhou, D. Zhong, H. Luo, J. Pan and D. Zhang, *Appl. Surf. Sci.*, 2018, **427**, 1183–1192.
206 X. Zhang, Y. Shen, Q. Zhang, L. Gu, Y. Hu, J. Du, Y. Lin and C. W. Nan, *Adv. Mater.*, 2015, **27**, 819–824.
207 H. Qu, S. Wei and Z. Guo, *J. Mater. Chem. A*, 2013, **1**, 11513–11528.
208 J. Xue, J. Xie, W. Liu and Y. Xia, *Acc. Chem. Res.*, 2017, **50**, 1976–1987.
209 J. Yoon, H.-S. Yang, B.-S. Lee and W.-R. Yu, *Adv. Mater.*, 2018, **30**, 1704765.
210 J. Xue, T. Wu, Y. Dai and Y. Xia, *Chem. Rev.*, 2019, **119**, 5298–5415.
211 P. Hu, Z. Jia, Z. Shen, P. Wang and X. Liu, *Appl. Surf. Sci.*, 2018, **441**, 824–831.
212 D. Ciprari, K. Jacob and R. Tannenbaum, *Macromolecules*, 2006, **39**, 6565–6573.
213 S. Peng, X. Yang, Y. Yang, S. Wang, Y. Zhou, J. Hu, Q. Li and J. He, *Adv. Mater.*, 2019, 1807722.
214 A. J. Bard and L. R. Faulkner, *Electrochemical Methods-Fundamentals and Applications*, John Wiley & Sons, Inc, 2nd edn, 2001.
215 M. Elimelech, *et al.*, *Particle Deposition and Aggregation-Measurement, Modelling and Simulation*, Butterworth-Heinemann, 1995.
216 P. Atkins and J. D. Paula, *Atkins' Physical Chemistry*, Oxford University Press, 8th edn, 2006.
217 H. Ohshima, *Electrical Phenomena at Interfaces and Biointerfaces-Fundamentals and Applications in Nano-, Bio-, and Environmental Sciences*, John Wiley & Sons, Inc., 2012.
218 Z.-H. Shen, J.-J. Wang, J.-Y. Jiang, Y.-H. Lin, C.-W. Nan, L.-Q. Chen and Y. Shen, *Adv. Energy Mater.*, 2018, **8**, 1800509.
219 X. Zhang, W. Chen, J. Wang, Y. Shen, L. Gu, Y. Lin and C.-W. Nan, *Nanoscale*, 2014, **6**, 6701–6709.
220 T. J. Lewis, *IEEE Trans. Dielectr. Electr. Insul.*, 2004, **11**, 739–753.
221 T. Tanaka, M. Kozako, N. Fuse and Y. Ohki, *IEEE Trans. Dielectr. Electr. Insul.*, 2005, **12**, 669–681.
222 T. Tanaka, *IEEE Trans. Dielectr. Electr. Insul.*, 2005, **12**, 914–928.
223 S. Li, G. Yin, G. Chen, J. Li, S. Bai, L. Zhong, Y. Zhang and Q. Lei, *IEEE Trans. Dielectr. Electr. Insul.*, 2010, **17**, 1523–1535.
224 M. Ezzat, N. A. Sabiha and M. Izzularab, *Appl. Nanosci.*, 2014, **4**, 331–338.
225 X. He, K. Yao and B. K. Gan, *J. Appl. Phys.*, 2005, **97**, 084101.
226 J. P. Calame, *J. Appl. Phys.*, 2006, **99**, 084101.
227 F. A. Pearsall, J. Lombardi and S. O'Brien, *ACS Appl. Mater. Interfaces*, 2017, **9**, 40324–40332.
228 A. M. Pourrahimi, R. T. Olsson and M. S. Hedenqvist, *Adv. Mater.*, 2018, **30**, 1703624.
229 S. Li, D. Min, W. Wang and G. Chen, *IEEE Trans. Dielectr. Electr. Insul.*, 2016, **23**, 3476–3485.
230 D. Min, W. Wang and S. Li, *IEEE Trans. Dielectr. Electr. Insul.*, 2015, **22**, 1483–1491.
231 A. T. Hoang, Y. V. Serdyuk and S. M. Gubanski, *Polymers*, 2016, 8, UNSP 103.
232 T. Takada, Y. Hayase, Y. Tanaka and T. Okamoto, *IEEE Trans. Dielectr. Electr. Insul.*, 2008, **15**, 152–160.
233 K. C. Kao, *Dielectric Phenomena in Solids-With Emphasis on Physical Concepts of Electronic Processes*, Elsevier, Inc., 2004.
234 C. Kittel, *Introduction to Solid State Physics*, John Wiley & Sons, 8th edn, 2005.
235 S. O. Kasap, *Principles of Electronic Materials and Devices*, McGraw-Hill, 3rd edn, 2006.
236 A. J. Dekker, *Electrical Engineering Materials*, Prentice-Hall, Inc, 1959.
237 Z.-M. Dang, Polymer Nanocomposites with High Permittivity, *Nanocrystalline Materials Their Synthesis-Structure-Property Relationships and Applications*, Elsevier, 2nd edn, 2014, ch. 9.
238 J. Shen and Y. Q. Ma, *Phys. Rev. B: Condens. Matter Mater. Phys.*, 2000, **61**, 14279–14282.
239 L. Gao, J. He, J. Hu and Y. Li, *J. Phys. Chem. C*, 2014, **118**, 831–838.
240 J. Shen and Y. Q. Ma, *J. Appl. Phys.*, 2001, **89**, 5031–5035.
241 D. Yang, S. Huang, M. Ruan, Y. Wu, S. Li, H. Wang, J. Zhang, H. Ma, W. Guo and L. Zhang, *J. Mater. Chem. C*, 2017, **5**, 7759–7767.
242 X. Xiao, N. Xu, Y. Jiang, Q. Zhang, E. Yu and H. Yang, *RSC Adv.*, 2016, **6**, 69580–69585.
243 L. Ren, X. Meng, J.-W. Zha and Z.-M. Dang, *RSC Adv.*, 2015, **5**, 65167–65174.
244 S. Nayak, B. Sahoo, T. K. Chaki and D. Khastgir, *RSC Adv.*, 2013, **3**, 2620–2631.
245 Y. Yao, N. Ning, L. Zhang, T. Nishi and M. Tian, *RSC Adv.*, 2015, **5**, 23719–23726.
246 X. Chen, J.-K. Tseng, I. Treufeld, M. Mackey, D. Schuele, R. Li, M. Fukuto, E. Baer and L. Zhu, *J. Mater. Chem. C*, 2017, **5**, 10417–10426.
247 B. Xie, Q. Zhang, L. Zhang, Y. Zhu, X. Guo, P. Fan and H. Zhang, *Nano Energy*, 2018, **54**, 437–446.
248 A. Chen, Y. Zhi, R. Guo and A. S. Bhalla, *J. Appl. Phys.*, 2003, **93**, 3475–3480.

249 K. Zhou, S. A. Boggs, R. Ramprasad, M. Aindow, C. Erkey and S. P. Alpay, *Appl. Phys. Lett.*, 2008, **93**, 325.
250 Y. U. Wang, *Appl. Phys. Lett.*, 2010, **96**, 034115.
251 Y. U. Wang, D. Q. Tan and J. Krahn, *J. Appl. Phys.*, 2011, **110**, 044103.
252 Z.-H. Shen, J.-J. Wang, X. Zhang, Y. Lin, C.-W. Nan, L.-Q. Chen and Y. Shen, *Appl. Phys. Lett.*, 2017, **111**, 092901.
253 J. I. Roscow, C. R. Bowen and D. P. Almond, *ACS Energy Lett.*, 2017, **2**, 2264–2269.
254 H. Luo, J. Roscow, X. Zhou, S. Chen, X. Han, K. Zhou, D. Zhang and C. R. Bowen, *J. Mater. Chem. A*, 2017, **5**, 7091–7102.
255 R. K. Bose, J. Koetteritzsch, S. J. Garcia, M. D. Hager, U. S. Schubert and S. van der Zwaag, *J. Polym. Sci., Polym. Chem.*, 2014, **52**, 1669–1675.
256 D. P. Agoris, I. Vitellas, O. S. Gefle, S. M. Lebedev and Y. P. Pokholkov, *J. Phys. D: Appl. Phys.*, 2001, **34**, 3485–3491.
257 Z.-H. Shen, J.-J. Wang, Y. Lin, C.-W. Nan, L.-Q. Chen and Y. Shen, *Adv. Mater.*, 2018, **30**, 1704380.
258 X. Zhang, J. Jiang, Z. Shen, Z. Dan, M. Li, Y. Lin, C.-W. Nan, L. Chen and Y. Shen, *Adv. Mater.*, 2018, **30**, 1707269.
259 Y. Zeng, Z.-H. Shen, Y. Shen, Y. Lin and C.-W. Nan, *Appl. Phys. Lett.*, 2018, **112**, 103902.
260 H. X. Tang and H. A. Sodano, *Appl. Phys. Lett.*, 2013, **102**, 063901.
261 G. Wang, X. Huang and P. Jiang, *Sci. Rep.*, 2017, **7**, 43071.
262 Y. Wang, X. Huang, T. Li, Z. Wang, L. Li, X. Guo and P. Jiang, *J. Mater. Chem. A*, 2017, **5**, 20737–20746.
263 D. Zhang, X. Zhou, J. Roscow, K. Zhou, L. Wang, H. Luo and C. R. Bowen, *Sci. Rep.*, 2017, **7**, 45179.
264 H. Tang, Y. Lin, C. Andrews and H. A. Sodano, *Nanotechnology*, 2010, **22**, 015702.
265 Y. Yang, Z. Wang, Y. Ding, Z. Lu, H. Sun, Y. Li, J. Wei, R. Xiong, J. Shi, Z. Liu and Q. Lei, *APL Mater.*, 2013, **1**, 050701.
266 B. Xie, Y. Zhu, M. A. Marwat, S. Zhang, L. Zhang and H. Zhang, *J. Mater. Chem. A*, 2018, **6**, 20356–20364.
267 Q. Li, G. Zhang, F. Liu, K. Han, M. R. Gadinski, C. Xiong and Q. Wang, *Energy Environ. Sci.*, 2015, **8**, 922–931.
268 R. Wen, J. Guo, C. Zhao and Y. Liu, *Adv. Mater. Interfaces*, 2018, **5**, 1701088.
269 L. Wang, F. Gao, J. Xu, K. Zhang, J. Kong, M. Reece and H. Yan, *Compos. Sci. Technol.*, 2018, **158**, 112–120.
270 V. Tomer, E. Manias and C. A. Randall, *J. Appl. Phys.*, 2011, **11**, 154103.
271 H. Tang, Y. Lin and H. A. Sodano, *Adv. Energy Mater.*, 2012, **2**, 469–476.
272 B. Xie, H. Zhang, Q. Zhang, J. Zang, C. Yang, Q. Wang, M. Li and S. Jiang, *J. Mater. Chem. A*, 2017, **5**, 6070–6078.
273 Z. Wang, J. K. Nelson, H. Hillborg, S. Zhao and L. S. Schadler, *Compos. Sci. Technol.*, 2013, **76**, 29–36.
274 D. Zhang, W. Liu, L. Tang, K. Zhou and H. Luo, *Appl. Phys. Lett.*, 2017, **110**, 133902.
275 D. Zhang, W. Liu, R. Guo, K. Zhou and H. Luo, *Adv. Sci.*, 2017, **5**, 1700512.
276 X. Zhang, Y. Shen, Z. Shen, J. Jiang, L. Chen and C.-W. Nan, *ACS Appl. Mater. Interfaces*, 2016, **8**, 27236–27242.
277 Prateek, D. Singh, N. Singh, A. Garg and R. K. Gupta, *Compos. Sci. Technol.*, 2019, **174**, 158–168.
278 R. Su, Z. Luo, D. Zhang, Y. Liu, Z. Wang, J. Li, J. Bian, Y. Li, X. Hu, J. Gao and Y. Yang, *J. Phys. Chem. C*, 2016, **120**, 11769–11776.
279 J.-Y. Pei, J.-W. Zha, W.-Y. Zhou, S.-J. Wang, S.-L. Zhong, L.-J. Yin, M.-S. Zheng, H.-W. Cai and Z.-M. Dang, *Appl. Phys. Lett.*, 2019, **114**, 103702.
280 K. Yin, J. Zhang, Z. Li, J. Feng, C. Zhang, X. Chen, A. Olah, D. E. Schuele, L. Zhu and E. Baer, *J. Appl. Polym. Sci.*, 2019, **136**, 47535.
281 Y. Wang, L. Wang, Q. Yuan, J. Chen, Y. Niu, X. Xu, Y. Cheng, B. Yao, Q. Wang and H. Wang, *Nano Energy*, 2018, **44**, 364–370.
282 Y. Shen, Y. Hu, W. Chen, J. Wang, Y. Guan, J. Du, X. Zhang, J. Ma, M. Li and Y. Lin, *Nano Energy*, 2015, **18**, 176–186.
283 J. Jiang, X. Zhang, Z. Dan, J. Ma, Y. Lin, M. Li, C.-W. Nan and Y. Shen, *ACS Appl. Mater. Interfaces*, 2017, **9**, 29717–29731.